Diploma Thesis

Evaluation and implementation of myQA software for Quality Assurance of beam optics measurements at MedAustron

for obtaining the academic degree

Master of Science

as part of the study

UE 066 461 - Technical Physics

submitted by

Tobias Radakovits, BSc
Student ID: 11805872

conducted at the **Atominstitut**
department for physics of Vienna University of Technology
In collaboration with **MedAustron**

Supervision
Supervisor: **Univ. Prof. Dr. Markus Stock** (Medaustron),
       Univ. Prof. Dr. Christina Streli (TU Wien)
Co-Supervisor: **Ass. Prof. Dr. Karin Poljanc** (TU Wien)
Under local supervision: **PhD. Marta Bolsa-Ferruz, PhD. Loïc Grevillot**

_____   _____   _____
Ort, Datum   (Unterschrift Verfasser/in)   (Unterschrift Betreuer/in)

Abstract

The implementation of advanced Quality Assurance (QA) procedures is crucial in medical facilities like MedAustron. MedAustron is dedicated to the research and treatment of cancer, with a unique focus on delivering proton and carbon ion therapies. Given the need for precision in radiotherapy, comprehensive QA procedures, including the examination of beam optics, are essential.

At MedAustron, beam optics tests have been evaluated using the software Lynx2D (Fimel, France) for acquisition, LynxQA application for analysis and myQA software (IBA, Belgium) for evaluation and data storage. These tests include spot maps, 2D homogeneous fields and intra-spill beam variations.

Because there was no existing medical certified analysis tool at the time, LynxQA, an in-house developed software was created by Virgile Letellier. However, myQA developed a standalone application known as Fast Track (myQA FT) within myQA since, which delivers analogous analysis tools to those found in LynxQA.

Firstly, the acquisition and analysis of beam optics parameters such as spot position and size, central axis, field size, homogeneity and symmetry using LynxQA and myQA FT were evaluated. The results concluded that the difference between the software for protons and carbon ions is within 0.2mm for spot position and size and within 0.5mm for the central axis and field size. Whereas the difference of the symmetry and homogeneity is within 0.2% and 0.5%, respectively. This is well within the expected uncertainties.

Additionally, the workflow of the acquisition and analysis of these parameters was constructed. The workflow consists of three different QA measurements: spot maps, 2D homogeneous fields and intra-spill variations. These workflows were implemented in the myQA software with the use of myQA FastTrack and Sphinx Plugin. Furthermore, improvements in automatization and efficiency were made. With the new workflows only one software is used, which mitigates data errors, and the time needed to acquire and analyze the data.

Zusammenfassung

Titel: Bewertung und Implementierung der myQA-Software für die Qualitätssicherung von Strahlungsoptik-Messungen bei MedAustron

Die Implementierung fortschrittlicher Verfahren zur Qualitätssicherung (QA) ist in medizinischen Einrichtungen wie MedAustron von entscheidender Bedeutung. MedAustron widmet sich der Forschung und Behandlung von Krebs mit einem einzigartigen Fokus auf Protonen- und Kohlenstoffionentherapien. Angesichts der erforderlichen Präzision in der Strahlentherapie sind umfassende QA-Verfahren, einschließlich der Untersuchung der Strahloptik, unerlässlich.

Bei MedAustron wurden Tests der Strahloptik mit der Software Lynx2D (Fimel, Frankreich) zur Datenerfassung, der LynxQA-Anwendung zur Analyse und der myQA-Software (IBA, Belgien) zur Bewertung und Datenspeicherung durchgeführt. Diese Tests umfassen Spot-Abbildungen, zweidimensionale homogene Felder und intra-spill Variationen des Strahls.

Da zum Zeitpunkt der Einführung kein medizinisch zertifiziertes Analysetool verfügbar war, wurde LynxQA, eine interne Software, von Virgile Letellier entwickelt. Inzwischen hat myQA jedoch eine eigenständige Anwendung namens Fast Track (myQA FT) innerhalb von myQA entwickelt, die ähnliche Analysetools wie LynxQA bietet.

Zuerst wurden Strahloptikparametern wie Spotposition und -größe, Zentralachse, Feldgröße, Homogenität und Symmetrie unter Verwendung von LynxQA und myQA FT in Sinne von Erfassung und Analyse untersucht. Die Ergebnisse zeigten, dass die Unterschiede zwischen den Softwareprogrammen für Protonen und Kohlenstoff Ionen bei Spotposition und -größe innerhalb von 0,2 mm und bei der Zentralachse und Feldgröße innerhalb von 0,5 mm liegen. Die Unterschiede bei Symmetrie und Homogenität liegen innerhalb von 0,2 % bzw. 0,5 %. Diese Werte liegen gut innerhalb der erwarteten Unsicherheiten.

Des Weiteren wurde eine Verbesserung des Workflows für die Erfassung und Analyse dieser Parameter entwickelt. Der Workflow besteht aus drei verschiedenen QA-Messungen: Spotkarten, zweidimensionale homogene Felder und intra-spill Variationen.

Diese Workflows wurden in der myQA-Software mithilfe von myQA FastTrack und dem Sphinx-Plugin implementiert. Darüber hinaus wurden Verbesserungen in der Automatisierung und Effizienz vorgenommen. Mit den neuen Workflows wird nur eine Software verwendet, was Datenfehler reduziert und die für die Datenerfassung und Datenanalyse benötigte Zeit verringert.

Acknowledgements

I would like to express my appreciation to everyone who assisted during the process of this thesis.

Firstly, I would like to thank Prof. Markus Stock and Prof. Christine Streli for providing me with the opportunity to write a thesis on this topic. I would also like to thank Prof. Karin Poljanc for her insights and guidance throughout my writing.

Next, I want to thank my colleagues at MedAustron for their warm welcome, time, and assistance when needed. It has been a pleasure to collaborate with you and I am looking forward to continuing to be part of your team in the future.

A special thanks is due to Loïc Grevillot and Marta Bolsa-Ferruz for mentoring me throughout the duration of this work. Your guidance and prompt responses to any issues were highly appreciated.

Last but not least, I would like to express my gratitude to my family and friends and especially my fiancé Noémie for their support in challenging situations.

Thank you.

Eidesstaatliche Erklärung

Ich erkläre an Eides statt, dass die vorliegende Arbeit nach den anerkannten Grundsätzen für wissenschaftliche Abhandlungen von mir selbstständig erstellt wurde. Alle verwendeten Hilfsmittel, insbesondere die zugrunde gelegte Literatur, sind in dieser Arbeit genannt und aufgelistet. Die aus den Quellen wörtlich entnommenen Stellen, sind als solche kenntlich gemacht. Das Thema dieser Arbeit wurde von mir bisher weder im In- noch Ausland einer Beurteilerin/einem Beurteiler zur Begutachtung in irgendeiner Form als Prüfungsarbeit vorgelegt. Diese Arbeit stimmt mit der von den Begutachterinnen/Begutachtern beurteilten Arbeit überein.

_____
Ort, Datum

_____
Signature

Contents

1.   Introduction

The incidence of cancer worldwide has been increasing rapidly, with the number of new cases rising from 14.1 million in 2015 to 18.1 million in 2020. During the same period, the number of cancer-related deaths also increased from 8.8 million to 9.9 million, highlighting the significant impact of this global health concern [1–3]. It is projected that almost 39.5% of individuals, both men and women, will be diagnosed with cancer at some point in their lives [2]. Therefore, there is an urgent need for comprehensive medical care, which has led to an accelerated pace of research aimed at refining cancer treatment methodologies.

1.1.   Radiotherapy

Traditionally, surgery, chemotherapy, and radiotherapy (RT) have been the primary conventional approaches for treating cancer. However, the need to mitigate tumor control probability and reduce side effects has led to the development of innovative treatments in recent decades [4]. In Austria developments in light ion beam therapy (LIBT) are available at the facility MedAustron in Wiener Neustadt (Austria). Here, the precise targeting of tumors is achieved through the application of protons and carbon ions. This precision is achieved by the Bragg Peak (BP), wherein the ion releases the majority of its energy at the end of its trajectory. This can be seen in Figure 1, where different depth to dose distributions in a water tank are shown. Where water is a good approximation for human tissue. By adjusting the beam energy, and consequently its penetration depth in the body, the Bragg Peak can be expanded to cover the tumor in two dimensions, a technique known as the Spread-Out Bragg Peak (SOBP)[1]. Simultaneously, the beam is adjusted in the transverse plane to ensure the entire three-dimensional tumor volume is covered. This precise targeting minimizes energy deposition in healthy tissues surrounding the tumor, as the radiation dose before and beyond the Bragg Peak is significantly lower compared to conventional radiotherapy. Additionally, heavy ions, such as carbon ions used at

---

[1] Explained in section 2.4 Beam Delivery Techniques

MedAustron, are effective in treating radiation-resistant tumors that are unresponsive to conventional therapies. [5]
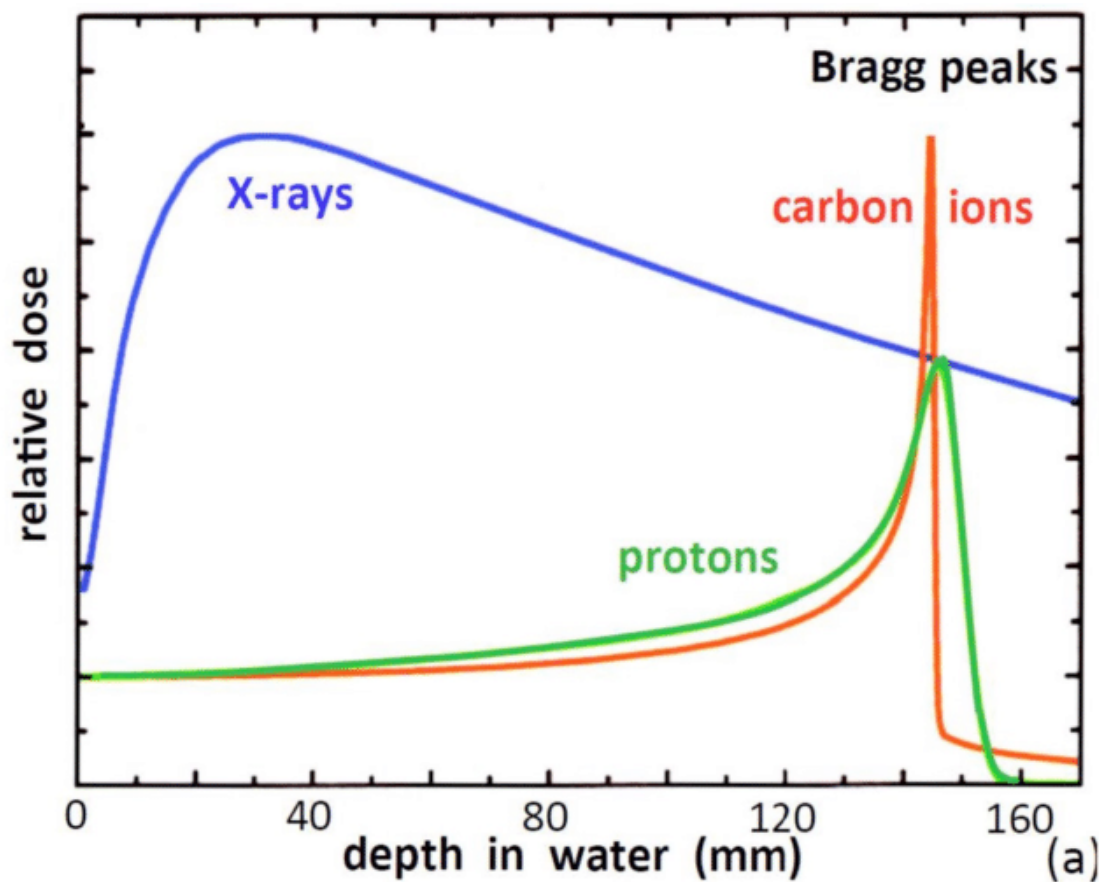
Figure 1: Dose-depth distribution profile comparing mono-energetic photon beams (blue), proton beams (green), and carbon ion beams (red). Particles enter from the left. [6]

Another widely used approach to tumor treatment is photon therapy, which relies on high-energy photons generated by accelerating electrons (up to MeV energies) in a linear accelerator (LINAC, see Figure 2). These electrons are directed onto an anode, producing X-rays through Bremsstrahlung with energies ranging from keV to MeV. [7] The resulting photon beam is then shaped and focused using a collimator to conform to the tumor's geometry. [8]

When photons traverse the patient, they deposit energy continuously along their path, as illustrated in Figure 1. This energy deposition is governed by probabilistic photon interactions with matter, including the photoelectric effect, Compton scattering, and pair production (see section 2.1.1 "Photons").[9] Unlike proton or carbon ion beams, where the interaction probability increases with depth and culminates in a distinct Bragg peak,

2

photons deposit energy continuously along their path without a stopping point. This results in a dose buildup near the surface, followed by an exponential decrease through the tissue. Consequently, photon therapy exposes healthy tissues to higher radiation doses both before and beyond the tumor compared to hadron therapy.
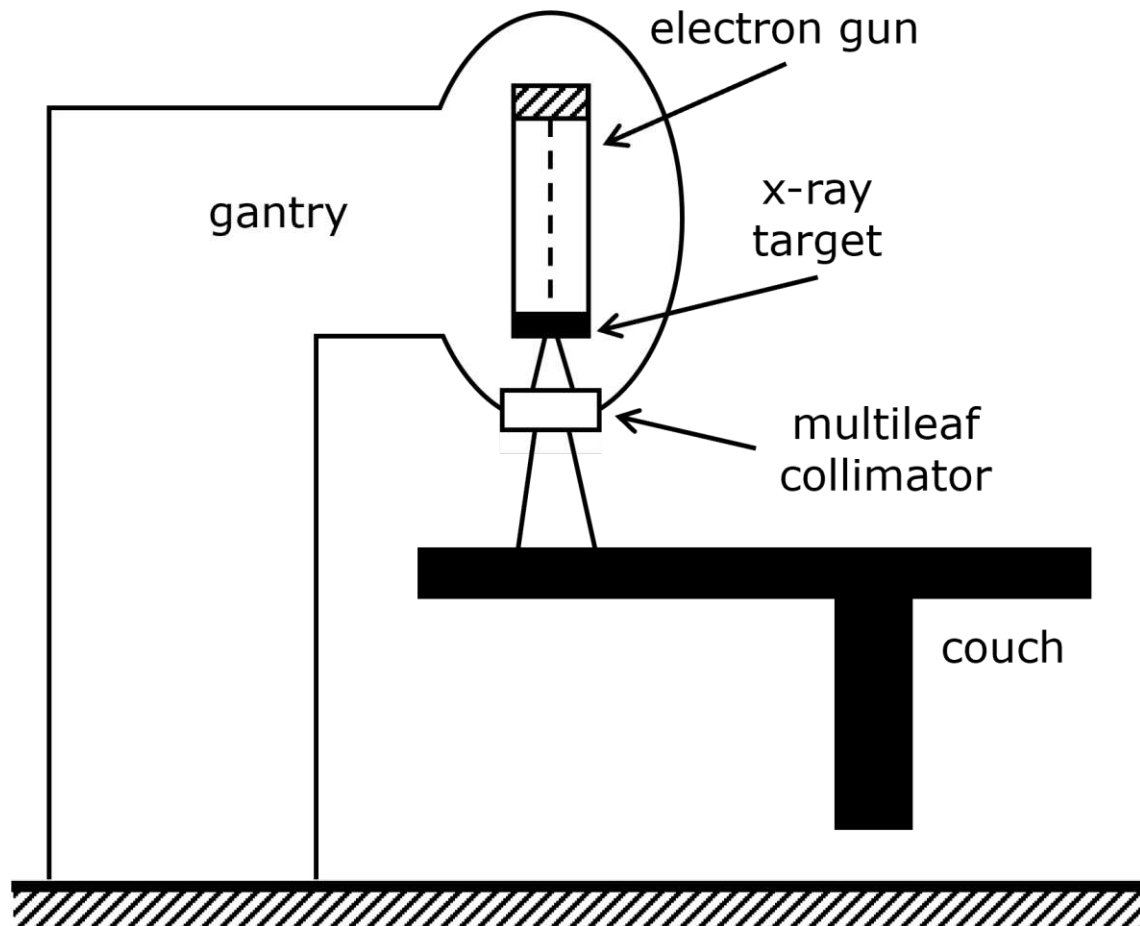
Figure 2: Schematic view of a medical LINAC used for photon therapy. (Modified from [8]

Despite this limitation, photon therapy is more accessible than particle therapy, as LINACs are smaller, comparatively expensive, and more widely available. Furthermore, not all tumors are located near critical organs, making photon therapy a viable and effective treatment option in many cases. [7,10]

To achieve the high precision required for treatments near vital organs in hadron therapy, robust quality assurance protocols are essential. This thesis examines current quality assurance methods at MedAustron, introducing workflows that incorporate medically certified software to replace in-house solutions. These improvements aim to enhance

testing efficiency, allowing more tests per patient and potentially increasing the number of patients treated. Additionally, the use of certified medical devices enhances safety by reducing the likelihood of errors.

Chapter 1.1 provides a brief overview of the history of proton and carbon ion therapy, while chapter 1.2 focuses on its implementation at MedAustron in Austria.

1.2. History of Radiotherapy

In 1946, Robert Wilson proposed using protons and heavier ions for radiotherapy, due to their ability to travel in a nearly straight path through tissue, depositing energy in a focused area known as the Bragg Peak [11]. Only eight years later, the first clinical trial for proton beam treatment on animals and later on humans was conducted in 1954 in the Berkeley Radiation Laboratory [12].

Following the initial positive clinical responses of 26 patients, Berkeley started a long-term clinical and laboratory investigation, involving helium and heavier ions such as carbon [13]. Subsequently, numerous studies were conducted for the first time in the proton RT facility in Europe at the University of Uppsala, Sweden [14,15].

Since the 1990s, numerous hospital-based proton therapy facilities worldwide have initiated clinical activities. Many clinics were established in USA, France, Canada, Germany, Russia, Japan, Italy, China, South Korea, Poland, the Czech Republic, Taiwan, and Austria. As of December 2022, approximately 362,300 patients worldwide have undergone treatment with particle therapy. About 312,000 patients treated with protons, about 46,800 with carbon ions and about 3,500 with helium, pions, and other particles [16].

1.3. MedAustron

In the following years many proton beam therapy facilities were constructed. But only six[2] unique facilities offer both proton and carbon ion irradiation therapy, called *dual particle facilities*. One of them is the MedAustron Ion Therapy Center, where particle therapy is currently conducted using protons or carbon ions. Protons are more commonly employed globally due to the widespread availability of equipment, whereas carbon ions require larger and more expensive technical equipment. Both particles possess the advantage that the radiation exposure in healthy tissue can be kept low. Carbon ions, however, additionally have a higher biological effectiveness, releasing more lethal events in tumor cells.[17,18]

In the following chapter the basic physics underlying particle beam therapy, focusing on particle interaction in matter is discussed. Furthermore, different kinds of detectors are introduced and technologies to accelerate the particles to the needed energies. Finally, beam delivery techniques are explained and the need for quality assurance is discussed, outlining current methods at different facilities.

---

[2]*As of December 2023:* MedAustron Wiener Neustadt (Austria), SPHIC Shanghai (China), HIT Heidelberg (Germany), MIT Marburg (Germany), CNAO Pavia (Italy), HIBMC Hyogo (Japan). *Under Construction:* Himed Cancer Hospital Xuzhou City Jiangsu Province (China), Mayo Carbon Ion Therapy Center Jacksonville Florida (USA)

2.   Physical Background

This chapter provides an overview of the fundamental principles and technologies underlying hadron therapy. It begins with the types of detectors utilized to measure particle interactions, emphasizing their role in monitoring dose distribution and ensuring treatment accuracy. Various accelerator types, including synchrotrons, cyclotrons, and linear accelerators, are then discussed, highlighting their mechanisms for energy adjustment and particle acceleration. The chapter also explores beam delivery techniques, such as passive scattering and pencil beam scanning (PBS), which enable precise targeting of tumors while minimizing harm to surrounding healthy tissue. Finally, the critical role of quality assurance in maintaining the reliability of beam delivery systems is examined, with a focus on MedAustron's QA practices for pencil beam optics and a discussion of challenges and proposed solutions in QA software integration. As well as a comparison to other facilities.

2.1.   Interaction of Particles in Matter

At MedAustron, the typical energy ranges used for treatment are 60–250 MeV for protons and 120–400 MeV for carbon ions (see section 3.1 "Energy Range at MedAustron"). This section examines the interaction of particles in matter, focusing on these energy ranges and including a brief overview of photons interactions for completeness.

2.1.1. Photons

Photon interactions with matter occur through three primary mechanisms, with the dominant process depending on photon energy (see Figure 3):

- **Photoelectric effect**: Dominant at low photon energies ($E_{Photon} < 1$ MeV), where the photon is fully absorbed by an atomic electron, which is subsequently ejected from the atom. [19]

- **Compton scattering**: Occurs across a broad energy range but is most dominant for $1 \leq E_{Photon} \leq 10$ MeV. In this process, a photon scatters off electrons, transferring energy and altering its wavelength. [19]

- **Pair production**: Dominant at high photon energies ($E_{Photon} > 10$ MeV), where the photon is converted into an electron-positron pair (the positron being the electron's antiparticle). [19]

In photon therapy, typical photon energies range between 2 and 18 MeV, with Compton scattering as the primary interaction mechanism. Even though the threshold energy for pair production is 1.022 MeV, it is not a major concern for clinical photon beams 10 MeV. [20,7] When irradiating the tissue, the primary photons are decreasing with depth and secondary electrons are set in motion, which delivers the needed dose. Because of the short buildup time of the secondary electrons the skin can be spared more.[21]
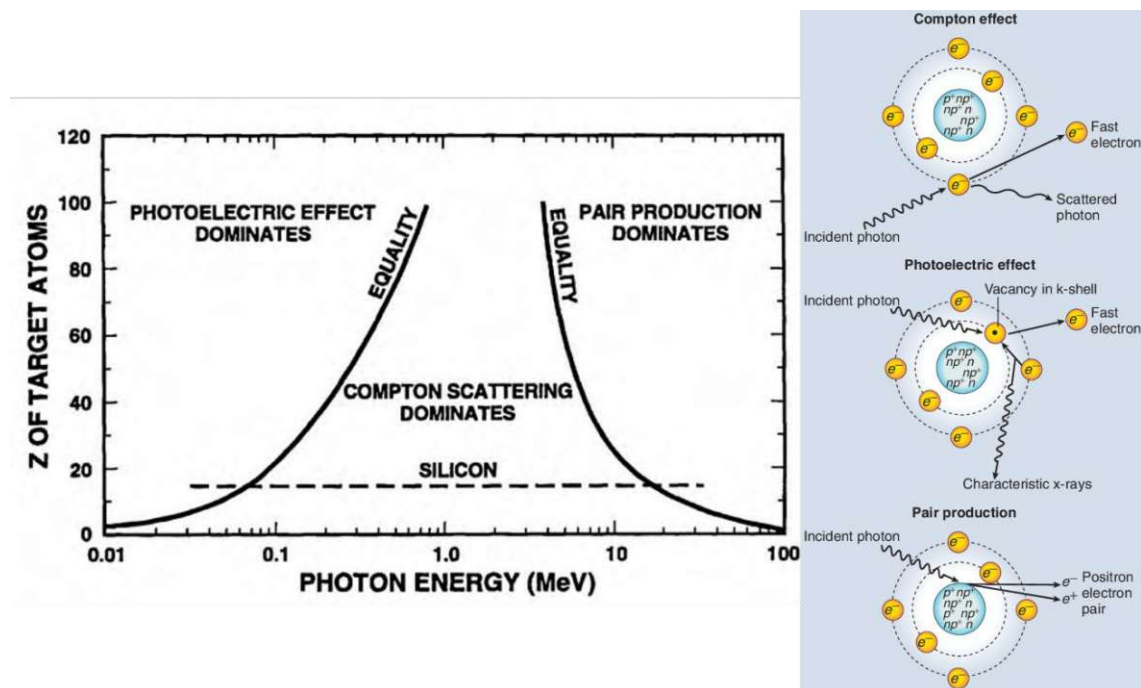

Figure 3: Left: Area of predominance of the three main forms of photon interaction with matter. [22] Right: Visualization of the three interaction forms. [7]

2.1.2. Charged Particles

Charged particles interact with matter primarily through collisions and radiation. In the context of hadron therapy, the radiation mechanism, primarily Bremsstrahlung, is negligible due to the high mass of the particles. Bremsstrahlung occurs when a charged particle is decelerated by the electromagnetic field of another charged particle, producing electromagnetic radiation. However, at the energy levels used in therapy, the energy loss from this process is minimal and does not significantly affect the treatment beam. [23-25]

Collisional Energy Loss

The most critical interaction in radiotherapy is collisions, particularly ionization through inelastic scattering with electrons. As charged particles traverse a medium, they interact electromagnetically with atomic electrons, transferring part of their energy. This results in two possible outcomes. The electrons are either excited by launching to a higher orbit (Excitation) or completely ejected out of the atom (Ionization).

In the case of protons and carbon ions the electron collisions result in a continuous slowing down effect referred to as *stopping*. Because the proton mass ($m_p \approx 1.672 \times 10^{-27} kg$ [26]) and the carbon ion mass ($m_c \approx 1.993 \ 10^{-26} kg$ [27]) are respectively 1832 and 21890 times heavier than the electron mass ($m_e \approx 9.109 \ 10^{-31} kg$ [28]), the energy loss per interaction is relatively small. Consequently, their lateral scattering is minimal, and the particles retain a highly focused trajectory. [23]

As protons and carbon ions decelerate further, their rate of energy loss increases significantly. This phenomenon results in the characteristic Bragg Peak (see Figure 4), where energy deposition sharply peaks just before the particle stops. This precise deposition is a key point of hadron therapy, enabling high doses to the target with minimal damage to surrounding tissues. [23]
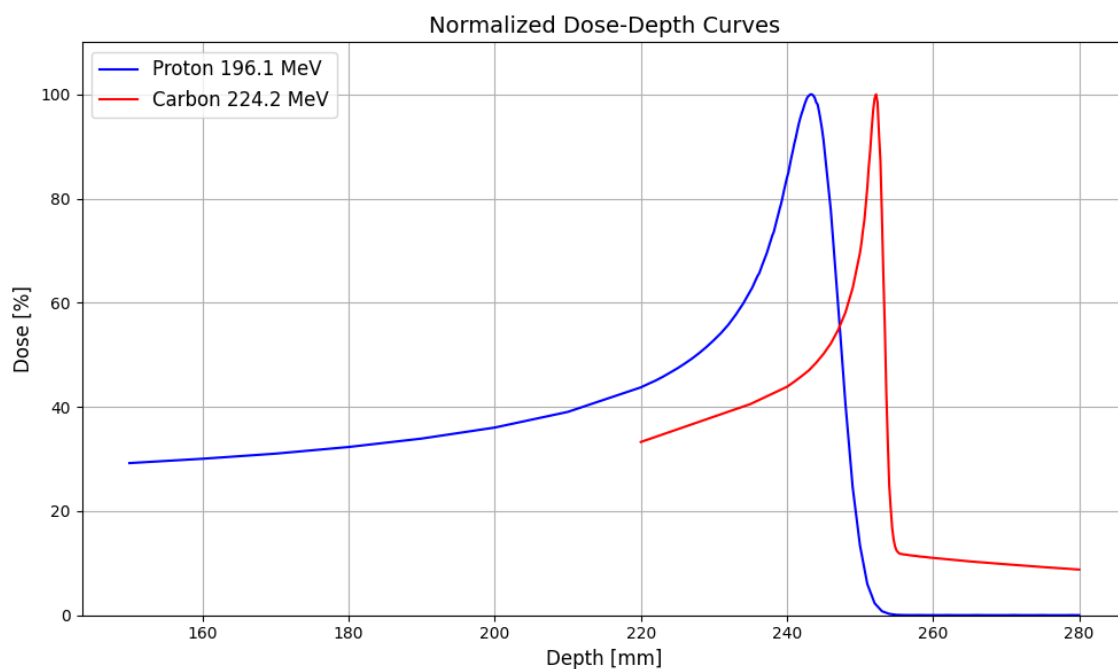
Figure 4: Normalized Dose-Depth curves for proton and carbon ion beams measured with a peakfinder at MedAustron.

Because the higher the mass of the ions the higher the scattering on the electrons is suppressed, which leads to sharper lateral penumbra for carbon ions and heavier ions. Furthermore, the dose falloff for heavier ions at the end of the range is even higher, due to the beforementioned reason. This can be used to place the beams closer to at risk organs laterally, while maintaining a high degree of organ sparing. [29,30] Figure 4 shows an apparent continuation of carbon ion deposition beyond the Bragg Peak. However, this is due to secondary particles generated through nuclear interactions, discussed in detail in section 2.1.4 "Range Sraggling".

Additional Interactions

Charged particles can also interact with matter through deflection by a nucleus or head-on collisions with a nucleus, leading to different effects. The *scattering* on the nucleus with the addition of the beforementioned scattering on the electrons (*stopping*) is well understood and summarized with multiple coulomb scattering (MCS). It is described by the electromagnetic interactions between the charged particle and the electric field of atomic electrons or, less commonly, the nucleus. In contrast, the head-on collision with a nucleus can lead to so called *nuclear reactions*, which involve complex phenomena described by a combination of empirically tested theories. Due to their relative

infrequency at therapeutic energy ranges[3], nuclear interactions are typically approximated. [[23]] These interaction mechanisms are illustrated in Figure 5.
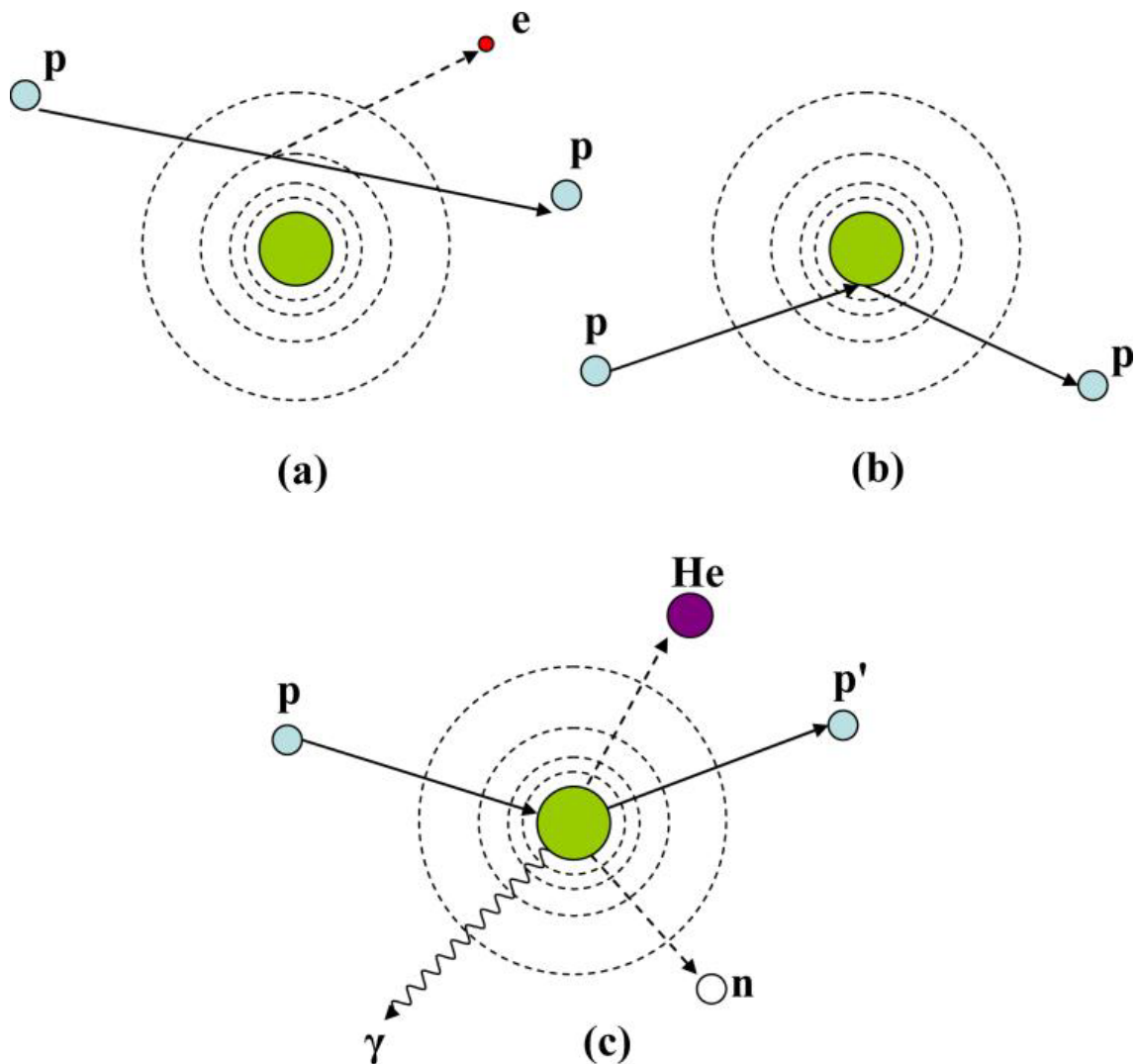
Figure 5: Schematic illustration of proton interaction mechanisms: (a) Coulombic interactions, (b) Coulomb scattering with nucleus, and (c) nuclear interactions producing secondary particles. [[23]]

The deflection of ions by individual nuclei is extremely small. Consequently, the observed angular spread of a beam passing through a medium result from the cumulative effect of numerous small deflections. Combined with scattering caused by electrons, the resulting spatial distribution is nearly Gaussian in the plane perpendicular to the beam axis. [[31]] This distribution is often analyzed by measuring the full width at half maximum (FWHM) of the Gaussian profile (see section 3.3 "Beam Optics Parameters").

---

[3] Except for carbon ions see section 2.1.4 "Range straggling".

2.1.3. Stopping Power

Figure 6 illustrates the stopping power of protons[4] in liquid water, calculated using Bethe's theory (see below). For convenience, the stopping power is normalized by the medium's density ($\rho = 0.998 \ g \ cm^{-3}$), with the mean excitation energy I = 78 eV. The logarithmic scale highlights the dominance of electronic stopping power over nuclear stopping power within the therapeutic energy range of 60–400 MeV. These nuclear effects are negligible, as shown in Figure 6, and can be safely ignored in radiotherapy calculations. [32]
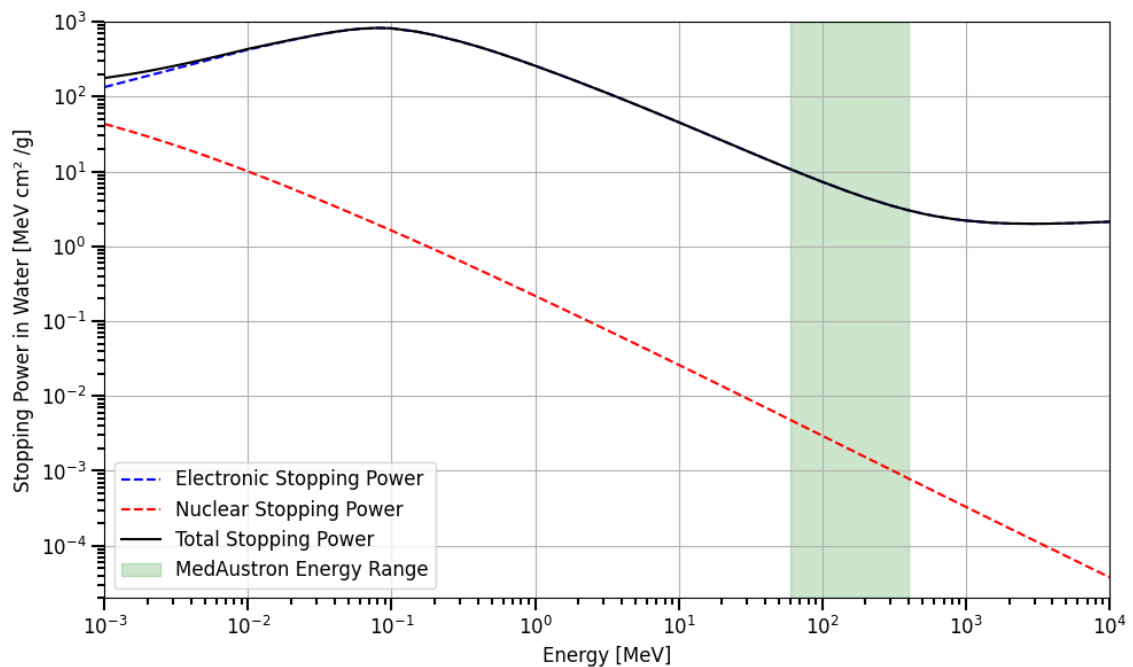
Figure 6: Total, electronic, and nuclear stopping power of protons in water showing the low effect of nuclear interaction at the energy range of meV to GeV. Emphasizing electronic stopping's dominance in the therapeutic range at MedAustron (60-400MeV). (Adapted from NIST) [32]

The stopping power is described by the Bethe bloch equation. The energy loss per unit length inside a medium with atomic number Z and number density n is given by:

---

[4] The same graph was done for carbon ions, which act similar (see Annex, Figure 36)

11

$$\frac{dE}{dx} \approx -4\pi\hbar^2 c^2 \alpha^2 \frac{nZ}{m_e v^2} \left\{ \ln\left[\frac{2\beta^2\gamma^2 c^2 m_e}{I_e}\right] - \beta^2 \right\},$$

where I_e is the effective ionization potential of the material averaged over all atomic electrons, $v = \beta c$ the velocity of the charged particle, and m_e the mass of the electron. [9]

As seen in Figure 6, the ionization energy loss depends on the velocity of the particle rather than its mass. The weak dependency on Z becomes evident when comparing stopping power curves for protons and carbon ions (Annex, Figure 36). Importantly, the energy loss increases as β^2, meaning slower particles are more ionizing than faster ones. This property explains the Bragg Peak, where the energy deposition rises sharply as the particle slows down near the end of its range.

The graph also shows a minimum ionization energy at a specific velocity, followed by a relativistic rise due to radiative losses. This observation underscores why Bremsstrahlung is negligible for radiotherapy within this energy range. [9]

2.1.4. Range Sraggling

In proton therapy, particles of identical incident energy stop at nearly the same depth, depositing no dose beyond the stopping point. However, due to statistical variations in the number of individual interactions, the proton range exhibits statistical errors, a phenomenon called *range straggling*. This effect becomes more pronounced if the incident beam has an energy spread and contributes to the full width half max (FWHM) of the Gaussian profile. The full stopping behavior is explained by the increasing momentum transfer in proton-electron collisions as the proton slows down. [31]

For carbon ions, their greater mass introduces additional effects. When sufficiently slowed, they can undergo *nuclear interactions* with a nucleus, breaking it apart and generating fragments that deposit energy at a later depth. These interactions lead to higher radiobiological effectiveness (RBE) compared to protons and result in a fragmentation tail in the dose-depth curve beyond the Bragg Peak. [33,30]

2.2. Types of Detectors

The primary objective of particle detectors is to measure properties such as energy, momentum or velocity, and lifetime of incident particles. For this thesis, we focus on detectors that rely on interactions between radiation and matter, resulting in measurable changes. These include charge detection (ionization chambers), light output (scintillators), or visible chemical changes (radiochromic films). [34]

2.2.1. Radiochromic Film

Radiochromic film consists of an active layer laminated between two polyester layers. The active layer consists of either dye, which changes color when exposed to ionizing radiation, or polycrystalline, substituted-diacetylene, which changes color due to progressive 1.4-trans additions as polyconjugations along the ladder-like polymer chains, which is proportional to the radiation dose (as can be seen in Figure 7). [34,35]

Advantages of radiochromic film include high spatial resolution, cut-ability, cost-effectiveness, and near energy-independent response. However, it is light-sensitive and non-reusable. Upon irradiation, the film's active component polymerizes, forming a colored polymer that polarizes transmitted light. This is digitized using dedicated scanners and analyzed with software such as PTW Mephysto (PTW Freiburg, Germany) or custom-developed tools. [36,37]

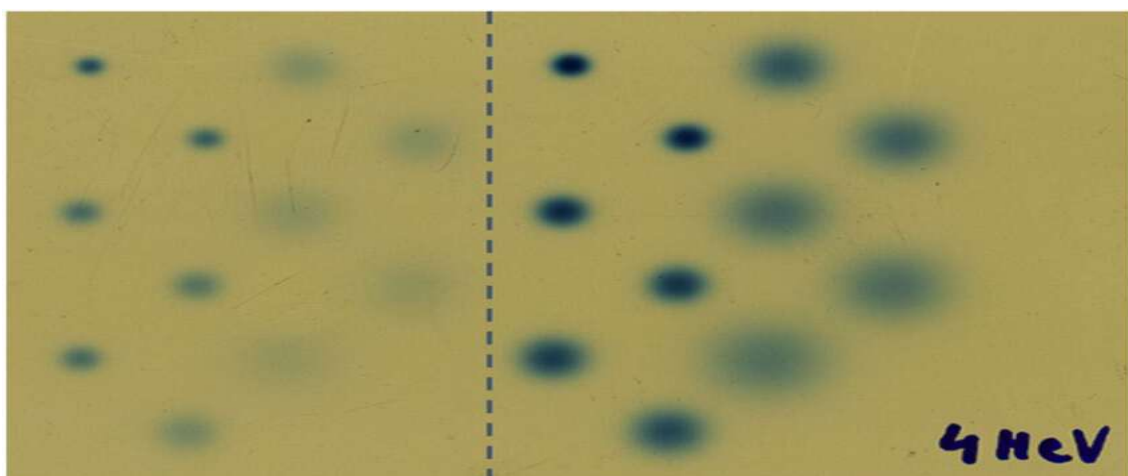**Use Cases:** Example applications include [38] and [39].

Figure 7: EBT3 film irradiated with 4 MeV protons at varying doses. [40]

2.2.2. Ionization Detectors

Ionization detectors measure the electric charge generated when an ion beam interacts with gas atoms within the detector. As ions pass through the gas, they cause ionization, and the resulting electrons and gas ions are collected by an electric field between the anode and cathode. The current produced is proportional to the radiation dose or intensity. [37]

To get spatial resolution, strips of ionization detectors are used. [41,42] When using doped silicon wafer instead of gas, the liberated electron-hole pairs can be used to measure the current created by the ion beam, which can be configured into strips or pixels. [9]

Ionization chambers offer several advantages, including insensitivity to fluctuations in applied voltage, making them reliable and cost-effective. Their response is directly proportional to the energy deposited by incident radiation, ensuring precise measurements, and their performance remains stable despite minor gas quality changes. However, they have limitations, such as low sensitivity in environments with minimal radiation and potential vulnerability to atmospheric conditions, which may slightly affect high-resolution systems. [37]

2.2.3. Scintillators

Scintillators rely on ionization effects, like ionization chambers. When an ion beam passes through a scintillator (plastic or liquid), it excites the molecules of the material. These molecules decay, emitting light. Fluorescent dyes are often added to absorb this light and re-emit it as detectable photons. Afterwards, photomultiplier devices are used to detect and measure the emitted photons. [19,37] In this thesis the commercially available scintillator Lynx (Schwarzenbruck, Germany) was used see section 3.2 "Equipment: Lynx".

Use Cases: Scintillators are used in [43] or [44] scenarios.

2.3. Accelerators

Before delivering the dose at a specific depth within the patient, the energy of the ions must be adjusted. There are two ways to achieve this, either ions are accelerated to a variable energy like in synchrotrons or linear accelerators or the ion energy is fixed and then slowed down in an adjustable amount of material like in cyclotrons. These types of accelerators are shortly introduced.

2.3.1. Linear Acelerator

A linear accelerator comprises a series of cylindrical electrodes called drift tubes (Figure 8). These tubes are connected to a radiofrequency (RF) system that generates an electric field in the gaps between them, accelerating particles as they pass through. Since the particle velocity increases with each gap, the length of the drift tubes must increase proportionally to ensure the flight time between gaps matches half the RF cycle period. [45]
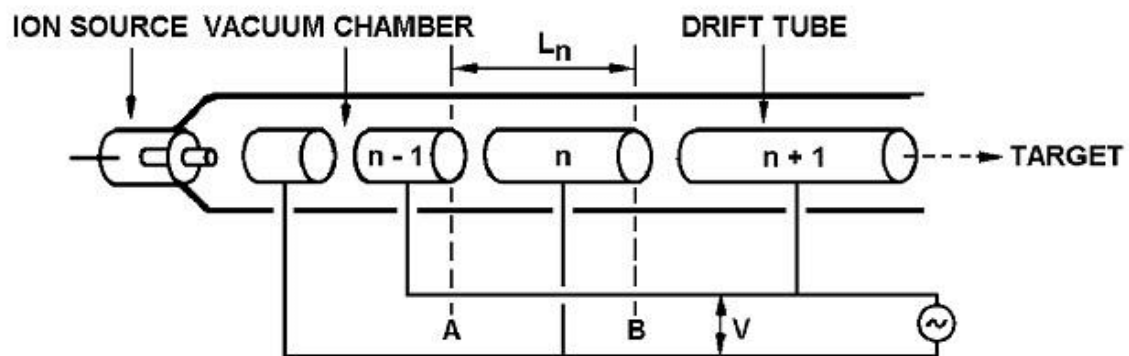
Figure 8: High voltage linear accelerator of Wiederöe-type. [adapted from [46]]

2.3.2. Cyclotron

In a cyclotron, particles follow a circular trajectory maintained by a homogeneous magnetic field (Figure 9). The structure consists of two semicircular electrodes (Dees) with an accelerating region in between. In the middle is an ion source, where the particles are extracted. The Dees are set under a high voltage by a radio frequency system, which creates an electric field between them. The particles are accelerated and kept on a circular

path by the magnetic field, then the voltage is reversed to accelerate in the other direction. When the particle reaches the maximum energy determined by the cyclotron dimensions, it is extracted and sent to a beam transport system. [45]

The voltage of the radio frequency system must be synchronous to the location of the ions at all radiuses. This is related to magnetic field B and the velocity of the particle by the Lorentz force. The Lorentz force is equal to the centripetal force:

$$\frac{mv^2}{r} = Bqv$$

Where the velocity can be written as $v = 2\pi r/T$, which results in the time required for one turn:

$$T = \frac{2\pi m}{qB}$$

This is independent of the radius and each cycle the velocity gets greater, which is why it is called Cyclotron. [45]
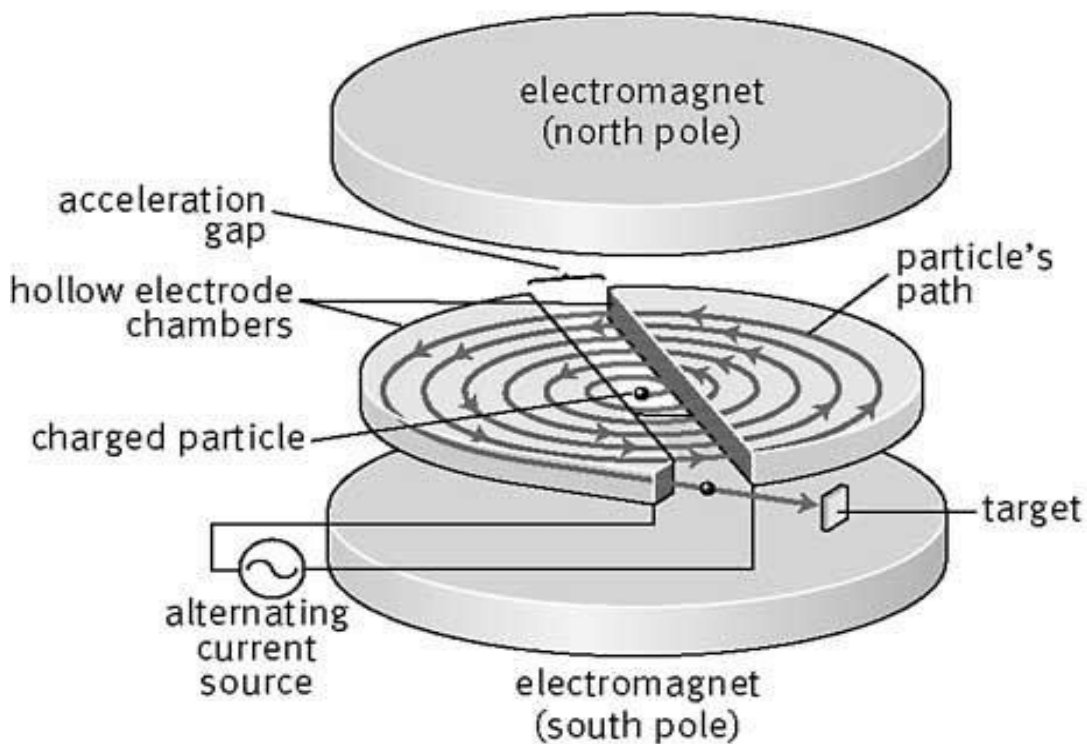

Figure 9: A schematic view of the Cyclotron. [46]

2.3.3. Synchrotron (MedAustron)

Synchrotrons are the dominant choice of accelerators used for heavy-ion therapy. The MedAustron synchrotron serves as an illustrative example.

The MedAustron particle therapy accelerator (MAPTA) (Figure 10) consist of three ion sources, creating either H_2^+ or C^{4+} ions. These are then pre-accelerated in Low-Energy Beam Transfer (LEBT) line, formed into a pulsed ion beam, further accelerated by a linear accelerator, and then injected into the main synchrotron ring. During injection, the ions pass through a fixed-target stripper foil, which removes one electron, resulting in H^+ or C^{6+} ions.

Inside the synchrotron, radiofrequency cavities accelerate the particles further, with the RF frequency dynamically adjusted to match the increasing particle speed. This synchronization, essential to maintain acceleration, gives the synchrotron its name. Dipole bending magnets are also adjusted to ensure the particles remain on their circular trajectory. The relationship between the particle momentum and the magnetic field is given by:

$$\frac{p}{Bq} = r = const.$$

Focusing and defocusing quadrupole magnets maintain the beam's focus. When the desired energy is achieved, the beam is extracted through the High-Energy Beam Transfer (HEBT) line and delivered to the irradiation rooms. There, the beam is monitored and modulated using a nozzle system. For carbon ions, the Bragg Peak must be broadened because, at low energies, its width is typically less than 1 mm, smaller than the spacing between adjacent tissue layers in treatment. [47]

The MedAustron facility includes three clinical treatment rooms and one research room (see Figure 10). Two of the clinical treatment rooms use both protons and carbon ions [48]. Specifically, one room features a horizontal beamline (HBL), while the other is equipped with both horizontal and vertical beamlines (VBL). Additionally, there is a third room with a gantry, exclusively used for proton therapy. For the gantry, at the time of

writing, there are three clinically commissioned angles G150, G90 and G0 (at 90 degrees ≙ HBL and 0 degrees ≙ VBL).
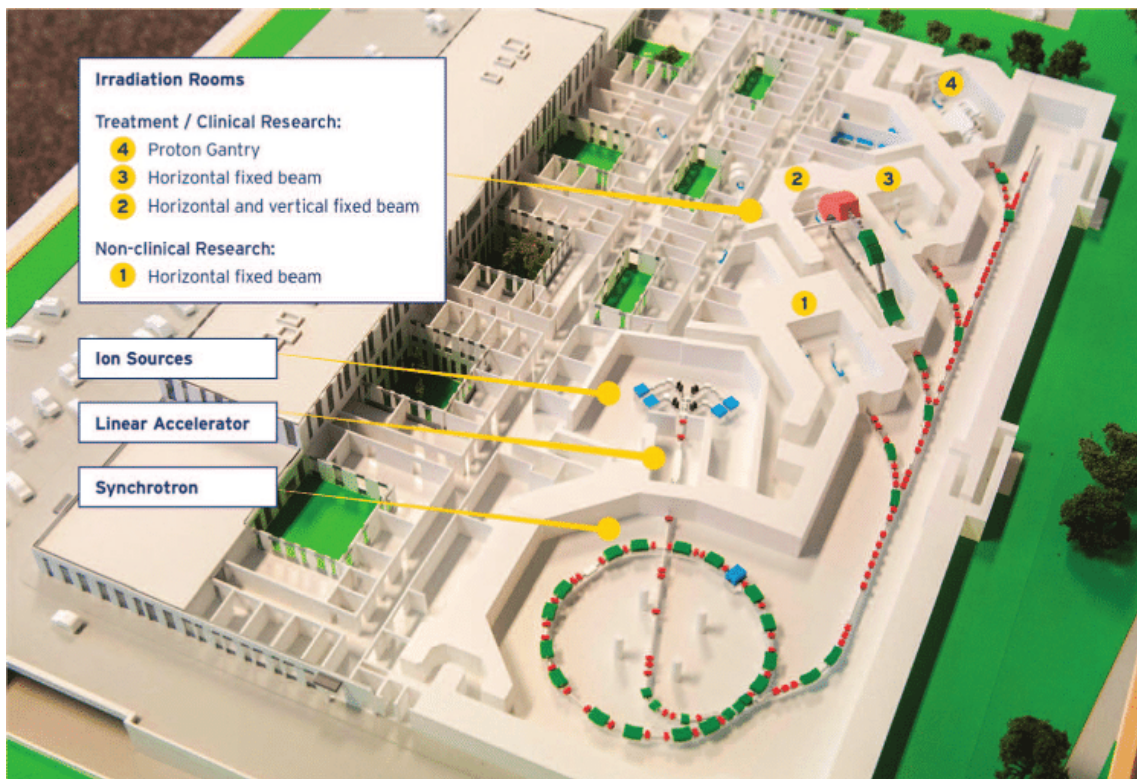

Figure 10: Layout of MedAustron, with the ion sources accelerator and the four irradiation rooms. [48]

2.4.   Beam Delivery Techniques

The size of a typical proton beam is considerably smaller than most tumors. Therefore, dedicated systems are required to spread the beam to cover tumor dimensions, which can reach up to 30–40 cm (e.g. sarcomas). Beam delivery systems play a critical role in ensuring that the dose is delivered precisely to the tumor while minimizing exposure to healthy tissues. This chapter outlines two primary beam delivery techniques: passive scattering and pencil beam scanning (PBS). [49]

2.4.1. Passive Scattering

Passive scattering is one of the most widely used methods for proton therapy. It involves broadening the proton beam laterally by passing it through high-Z materials, such as foils or thin plates, located within the treatment nozzle. This ensures a wide treatment field suitable for tumors of varying sizes. However, the scattering process reduces the beam's energy, requiring careful adjustments to maintain the necessary penetration depth. [49, 50]

Uniform dose distribution across the tumor depth is achieved through range modulation, where a rotating modulator wheel with varying thicknesses spreads individual Bragg Peaks into a composite Spread-Out Bragg Peak. This SOBP conforms to the tumor's volume. Additionally, patient-specific collimators are used to shape the beam laterally, ensuring accurate delivery tailored to the tumor geometry. [49, 50]

For larger treatment fields, the double scattering technique is employed. This method uses an initial scattering stage, range modulation, and a secondary scattering stage before the beam passes through patient-specific collimators. This multi-step process achieves a dose distribution conforming to the tumor's three-dimensional shape. (see Figure 11). [49, 50]
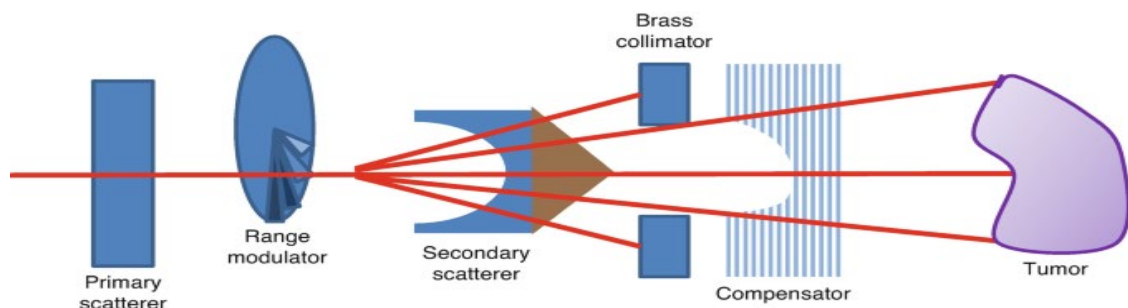

Figure 11: Schematic view of double scattering in passive scanning. [49]

2.4.2. Pencil Beam Scanning

Pencil beam scanning is a highly advanced and precise delivery technique that optimally targets tumors while minimizing the dose to healthy tissues. Unlike passive scattering, PBS uses a finely focused proton beam, termed a "pencil beam," which is scanned across the tumor slice by slice. Magnetic fields are employed to steer the beam in two dimensions perpendicular to its trajectory, achieving precise lateral tumor coverage.

To cover the tumor in three dimensions, the beam's energy is varied, adjusting its penetration depth. Sequential slices of the tumor are irradiated, creating a Spread-Out Bragg Peak and delivering a conformal dose to the entire tumor volume.

At MedAustron, a quasi-discrete scanning technique is employed, wherein the beam is applied without turning off during movement to the next spot of the same energy-layer. This ensures continuous delivery of radiation and a conformal dose distribution. Figure 12 illustrates the scanning process and highlights the precise application of proton beams within a target volume. [50].
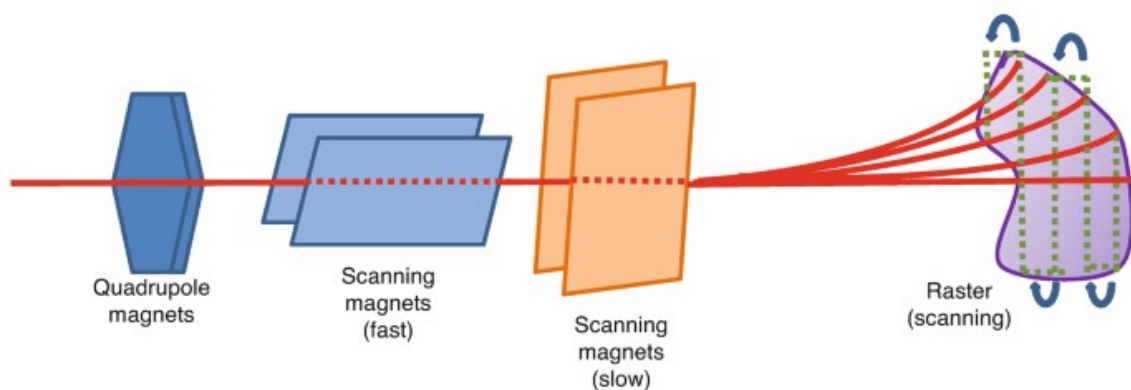

Figure 12: Schematic representation of a proton pencil beam. One tumor "slice" is scanned perpendicular to the beam path with the use of orthogonal scanning magnets. [49]

2.5. Quality Assurance

A hadron facility consists of many equipment components: accelerator, beam transport system, treatment delivery system, imaging system, medical software, etc. The configuration of these components varies based on the facilities objective (i.e. synchrotron, cyclotrons, scanning magnets, gantry, etc.) [50]. The diverse delivery techniques, including passive and dynamic beam delivery and their sub-techniques, alongside the utilization of different devices, resulted in a lack of uniform quality assurance guidelines for an extended period. This situation changed with the publication of the American Association of Physicists in Medicine (AAPM) Task Group 224 report in 2019. [18] While these are a set of guidelines, they are only recommendations, and different facilities use different setups. While a detailed exploration of these guidelines is beyond the scope of this work, this thesis will focus on the software aspects, specifically examining the QA of the beam optics in PBS, which is employed at MedAustron.

The AAPM report gives the following tolerances for beam parameter QA using pencil beam scanning:

Table 1: Recommended dosimetry tolerances

Dosimetry	Tolerances	Comments
Spot position	±2/±1 mm	absolute/relative
Spot size	±10%	
Spot delivery constancy	±10%	Spot position/size over time
2D field homogeneity	Within 10%	

2.5.1. Pencil Beam Optics QA at MedAustron

The QA for beam delivery at MedAustron is categorized into periodic and non-periodic tests. Periodic tests are further grouped into frequency (daily, weekly, monthly, bi-yearly,

yearly), while non-periodic tests are grouped into different events (after MAPTA[5] upgrade/breakdown, etc.).

The QA tests addressed in this thesis are done monthly and yearly. The experimental setup for all tests stays the same, using the Lynx (IBA-Dosimetry) (see section 3.2 "Equipment: Lynx") positioned on the couch at isocenter. Isocenter is defined as the reference point of the room around which the beam delivery and Patient Alignment System are calibrated. Then to accommodate the long cabling distances at MedAustron, a dedicated QA laptop is set up inside the irradiation room and connected to the Lynx device via LAN (see Figure 13). Simultaneously, in a separate control room, a remote connection to the QA laptop is established. The particle beams are irradiated into the Lynx which captures the transversal profile of each beam as DICOM files using the Lynx2D software. Afterwards, the DICOM files are analyzed with the in-house developed software LynxQA (by Virgile Letellier) and saved for long term trend analysis in myQA database. (see section 3.4.1 "Lynx2D and LynxQA Software").

The importance of QA lies in the high sensitivity of particle therapy to variations in beam quality. Factors such as spot size and position directly affect dose distribution, making QA vital for patient safety and treatment efficacy.

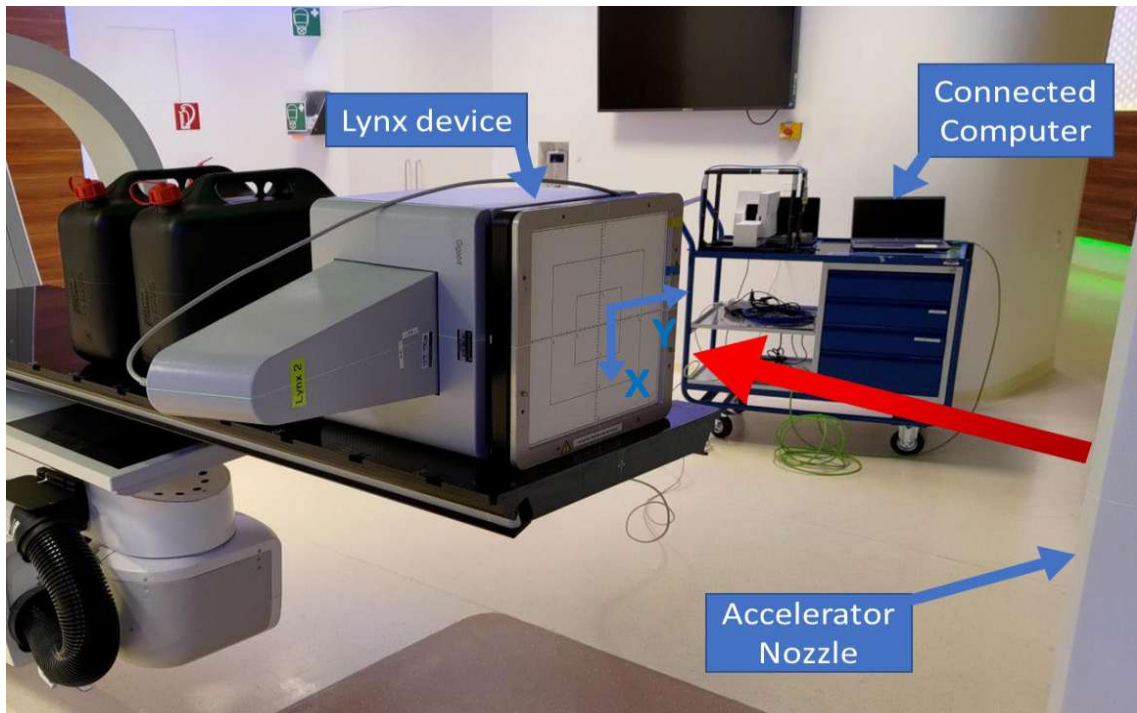[5] MedAustron Particle Therapy Accelerator

Figure 13: Setup: The Lynx is connected to the computer via an Ethernet cable and setup at the isocenter in the irradiation room. The coordinate system belonging to the Lynx is indicated.

Problems and Proposed Solution

The long-term maintenance of the in-house LynxQA software presents significant challenges, including resource demands for updates, troubleshooting, and ensuring compatibility with evolving systems. In contrast, the commercially available medical-grade software myQA, integrated with the myQA FastTrack (MyQA FT) plugin, provides an efficient, and robust solution. MyQA FT not only replaces Lynx2D for image acquisition but also serves as a comprehensive alternative to LynxQA for data analysis, offering a unified platform that eliminates the need for separate software applications.

This integration significantly streamlines the workflow, reducing operational complexity and minimizing the potential for errors during data transfer. MyQA FT enables simultaneous acquisition and analysis of beam data, saving valuable beam time. Moreover, because myQA FT operates on the same platform as the already established myQA database, saving and organizing data for long-term trend analysis becomes seamless and efficient. The direct compatibility of the plugin with the myQA ecosystem eliminates the manual steps currently required, further enhancing data integrity and reducing the workload for QA personnel.

2.5.2. Comparison to other Facilities

As previously mentioned, there are no official guidelines for quality assurance in hadron therapy, only recommendations, such as those from the AAPM Task Group 224 report, exist. At MedAustron, these recommendations have been used to design a comprehensive QA workflow with dedicated thresholds, which is regularly validated through independent dosimetry audits. However, comparing QA procedures across facilities remains challenging due to the heterogeneous use of beamline components, detectors, and thresholds. Despite these differences, the QA workflows at several facilities are outlined below.

The National Institute of Radiological Sciences (NIRS) in Japan employs a rotating gantry capable of delivering carbon ions at 430 MeV/u across various angles. Their daily QA system includes an ionization chamber for calibrating the primary dose monitor, output checks, and dose rate verification, as well as a scintillator system for range, isocenter, and gantry angle checks. [52] To assess beam optics parameters, such as spot size, beam position, and 2D field homogeneity, NIRS uses EBT3 radiochromic films. Across a 20 x 20 cm^2 scanned field, spot position accuracy was maintained within ±1 mm, and homogeneity within ±5% for both proton and carbon ions. [53]

At the CNAO therapy center in Pavia, Italy, pencil beam scanning QA initially relied on radiochromic films but later transitioned to the 2D MatriXX detector from IBA Dosimetry. This detector demonstrated positional resolutions of 0.23 mm for protons and 0.1 mm for carbon ions. [54]

In the United States, several facilities implementing PBS utilize either commercial or in-house QA devices, including the DQA-3, MLIC, and MatriXX-PT detectors. These setups vary widely in workflow and technical specifications. [55–59]

The diversity in detectors and QA procedures across facilities highlights the lack of a standardized approach. Most QA systems use scintillation detectors or radiochromic films to evaluate beam parameters, such as spot size, beam position, range, and 2D field

homogeneity. This variability underscores the importance of tailoring QA protocols to specific facility configurations and technologies.

3.   Materials and Methods

In this chapter, the methodologies for the three QA tests central to this thesis, spot map analysis, two-dimensional homogeneous field evaluation, and intra-spill variation analysis, are outlined in detail. The chapter also provides a comprehensive overview of the equipment and software employed, including their configurations and functionalities. Furthermore, the workflows currently in use at MedAustron are systematically described, highlighting the parameters and procedures that ensure the reliability and accuracy of beam optics quality assurance. Lastly, the chapter explains the comparative measurements performed with each software to evaluate and refine the QA workflows.

3.1.   Energy Range at MedAustron

In the clinical treatment rooms, proton beams are available at 255 discrete energies, ranging from 62.4 and 252.7 MeV (corresponding to a range of 30 – 380 mm in water). For carbon ions, energies range from 120.0 to 402.8 MeV/n (29.2 – 270 mm in water). [18,48]

For QA purposes, a subset of these energies is tested due to practical constraints.

The selected subsets include 5 "key" energies for quick daily representations and 20 (protons)/16 (carbon ions) "major" energies for more comprehensive monthly or yearly QA. These groupings ensure that a representative sample of the available energy is tested while maintaining efficiency. [17] Figure 14 summarizes the subdivision of these energies.

Table 2: Subdivided proton and carbon ion energies at MedAustron: 20 (proton) and 16 (carbon ion) major energies, including 5 key energies for quick representation. (MedAustron)

Energy Number	Energy Value PROTONS [MeV/n]	Category	Energy Number	Energy Value CARBONS [MeV/n]	Category
1	62.4	Major, Key	1	120.0	Major, Key
11	72.4	Major	12	139.4	Major
21	81.3	Major	22	155.9	Major
41	97.4	Major, Key	32	171.4	Major
61	111.6	Major	42	186.1	Major
81	124.7	Major	52	200.0	Major
101	136.8	Major	62	213.4	Major, Key
121	148.2	Major, Key	82	238.6	Major
141	159.0	Major	102	262.3	Major
160	169.3	Major	122	284.7	Major, Key
170	179.2	Major	142	306.2	Major
180	188.7	Major	162	326.8	Major
190	198.0	Major, Key	182	346.6	Major, Key
200	207.0	Major	202	365.8	Major
210	215.7	Major	222	384.5	Major
220	224.2	Major	242	402.8	Major, Key
230	232.6	Major			
240	240.8	Major			
250	248.8	Major			
255	252.7	Major, Key			

3.2. Equipment: Lynx

The Lynx utilizes a scintillator screen coupled with a high-resolution Ethernet CCD camera (Figure 15). The scintillator screen, composed of gadolinium-based plastic material, converts the energy lost by ionizing radiation into photons (see section 2.2.3 "Scintillators"). These photons are then reflected to the photodiodes of the CCD camera, positioned outside the irradiation field.

Once detected, the photons are converted into electrical signals and digitized at a 10-bit depth. The Lynx system supports a maximum field size of 30 × 30 cm^2 with a spatial resolution of 0.5 mm. [20]

For operation, the Lynx is placed on the treatment couch at the isocenter and aligned using in-room lasers. It enables direct data readout through Lynx2D (Fimel, France) or myQA FT software (IBA, Belgium) (see section 3.4 "Software"). This thesis focuses exclusively on tests utilizing Lynx2D for acquisition and LynxQA for analysis, specifically for portions of the monthly and yearly QA of beam optics at MedAustron.
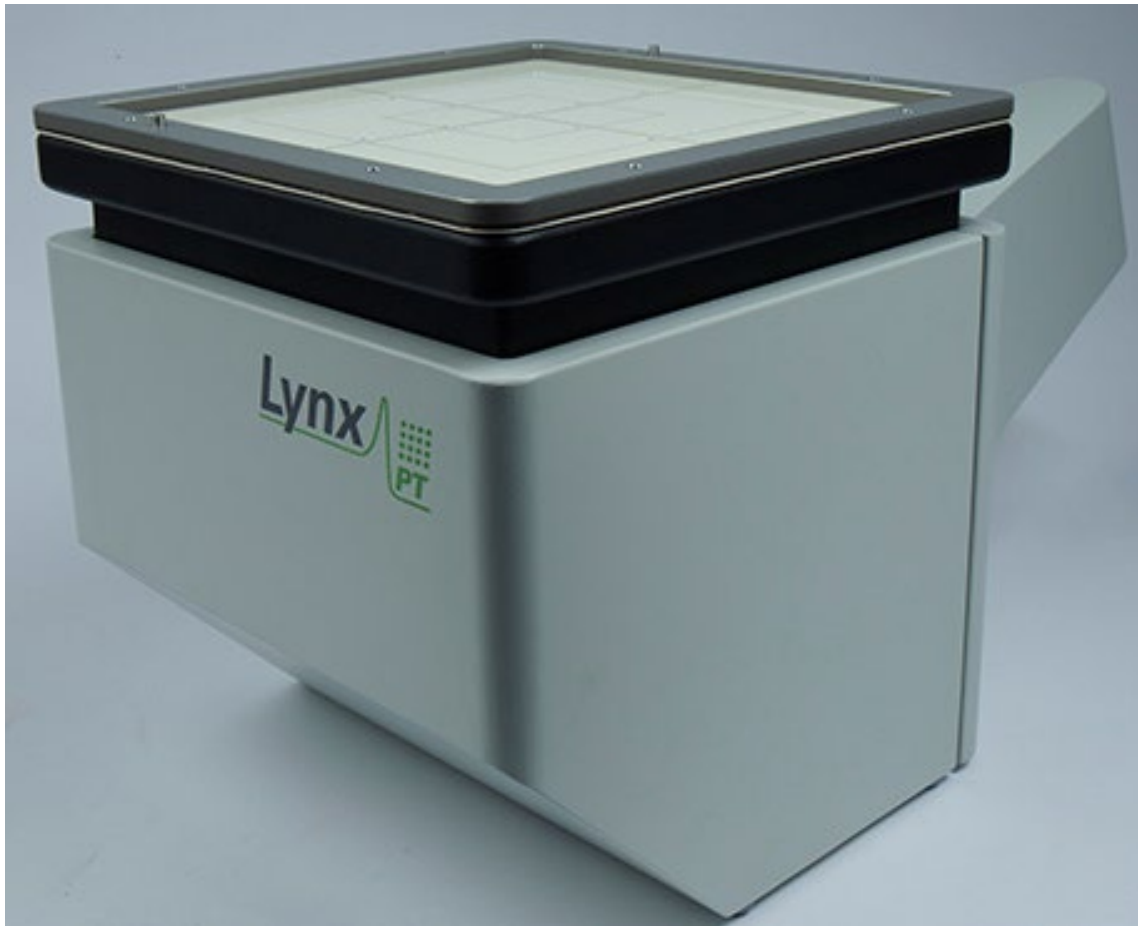

Figure 14: Lynx detector with scintillating screen and CCD camera. It connects software via LAN. [20]

3.3. Beam Optics Parameters

This section outlines the parameters for the three QA tests conducted as part of the monthly and yearly quality assurance: spot map analysis, 2D homogeneous field analysis, and intra-spill variation analysis.

3.3.1. Spot Map

The spot map used for quality assurance comprises nine pencil beam spots of protons or carbon ions arranged in a 3×3 grid over a 10×10 cm² area, as shown in Figure 16 left. This test focuses on assessing the deviations in the spot position and size (FWHM) at various coordinates. The Full Width at Half Maximum (FWHM), describes the width of the beam profile at half of its maximum dose value, assuming a Gaussian distribution.

The spot position refers to the center of the beam spot on a plane perpendicular to the beam axis. Its coordinates, defined as x (left-to-right) and y (down-to-up) in the LynxQA software, are evaluated for deviations. Additionally, the spot size, represented by the FWHM, is analyzed. This test ensures precise alignment and uniformity in spot delivery (Figure 16 right). [21,22]
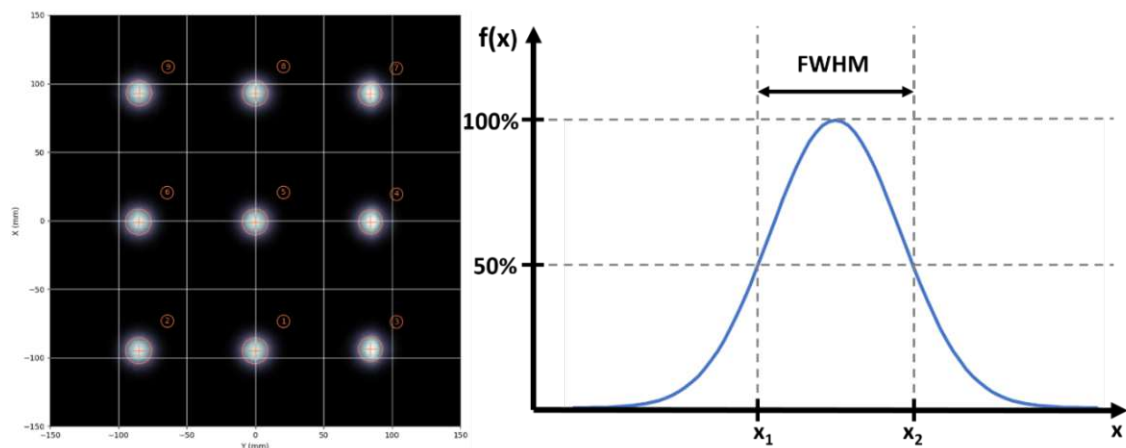
Figure 15: Spot map for a proton beam at 62.4 MeV in LynxQA. The spot size corresponds to the FWHM.

3.3.2. 2D Homogeneous Field

To create a 2D homogeneous field, particle beams are scanned adjacent to each other using a quasi-discrete scanning technique. A grid of beam spots is irradiated over the designated area, with spot spacing set to one-third of the FWHM. This arrangement ensures the delivery of a uniform dose at the isocenter, as illustrated in Figure 17.

29
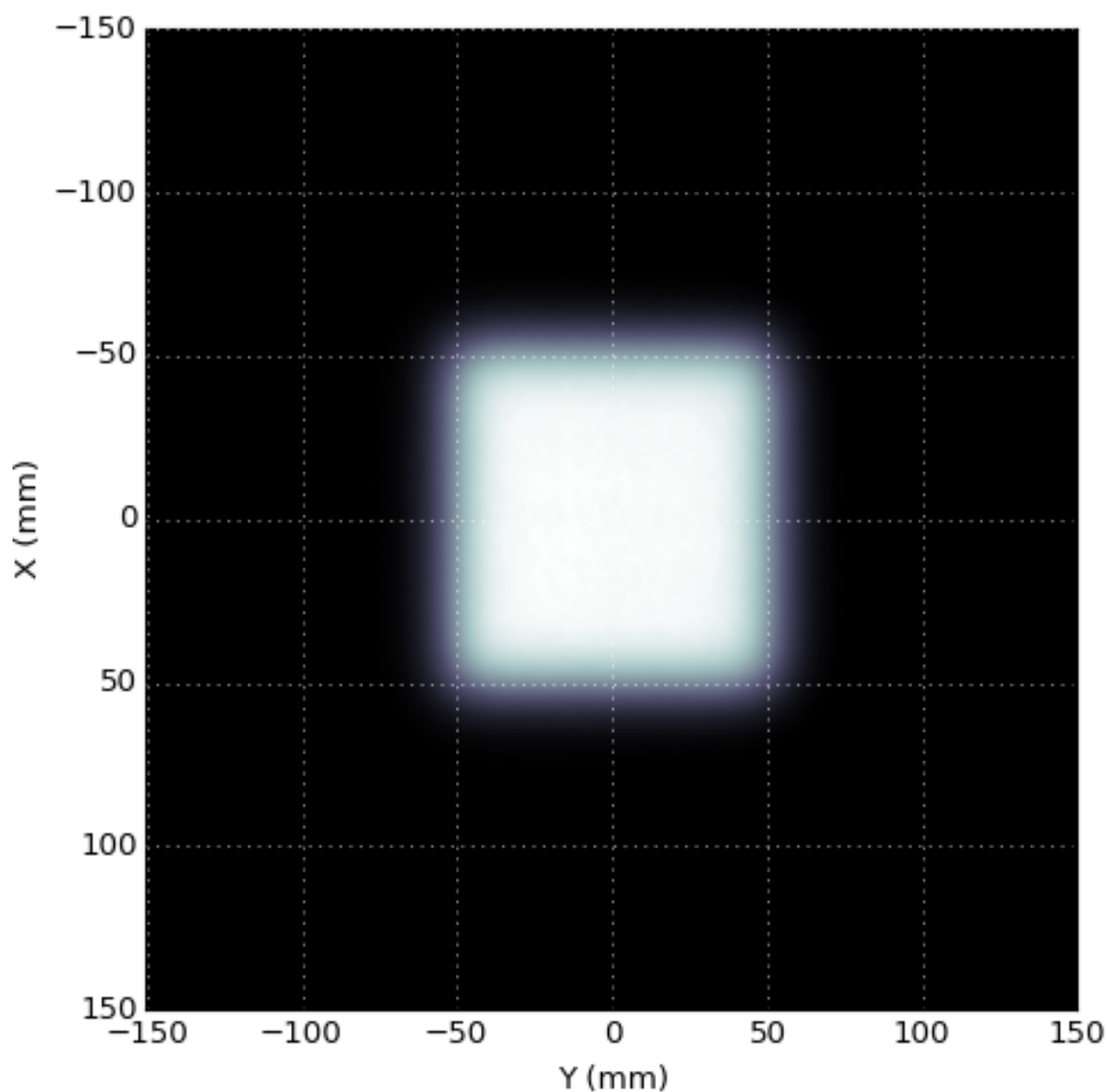
Figure 16: 2D homogenous map for a proton beam at 62.4 MeV in LynxQA.

Several parameters are analyzed within the 2D homogeneous field. The central axis (CAX) denotes the x and y coordinates of the field's center, providing a reference for field alignment. The field size at 50% (FS50) of the maximum dose measures the lateral distance between dose points at these respective levels, offering insight into the field's dimensions. Symmetry is assessed as the ratio of the dose difference between the two halves of the field relative to its total dose, calculated using the formula:

$$S = \left(\frac{D_1 - D_2}{D_1 + D_2} \right)$$

30

Here, D_1 and D_2 represent the integrated absorbed doses in each half of the field.

The treatment width (TW) is defined as the distance between the two lateral penumbras, measured at the 80% and 20% dose levels (LP80-20), relative to the 50% isodose level in the lateral beam profile. Additionally, 2D field homogeneity is evaluated within the treatment width. This parameter quantifies dose uniformity, calculated as:

$$H = \left(\frac{\text{Max} - Min}{\text{Max} + Min}\right)$$

where Max and Min are the highest and lowest doses within the analyzed area, respectively. Figure 18 depicts a transverse dose profile highlighting FS50, treatment width, and lateral penumbra (80–20%).
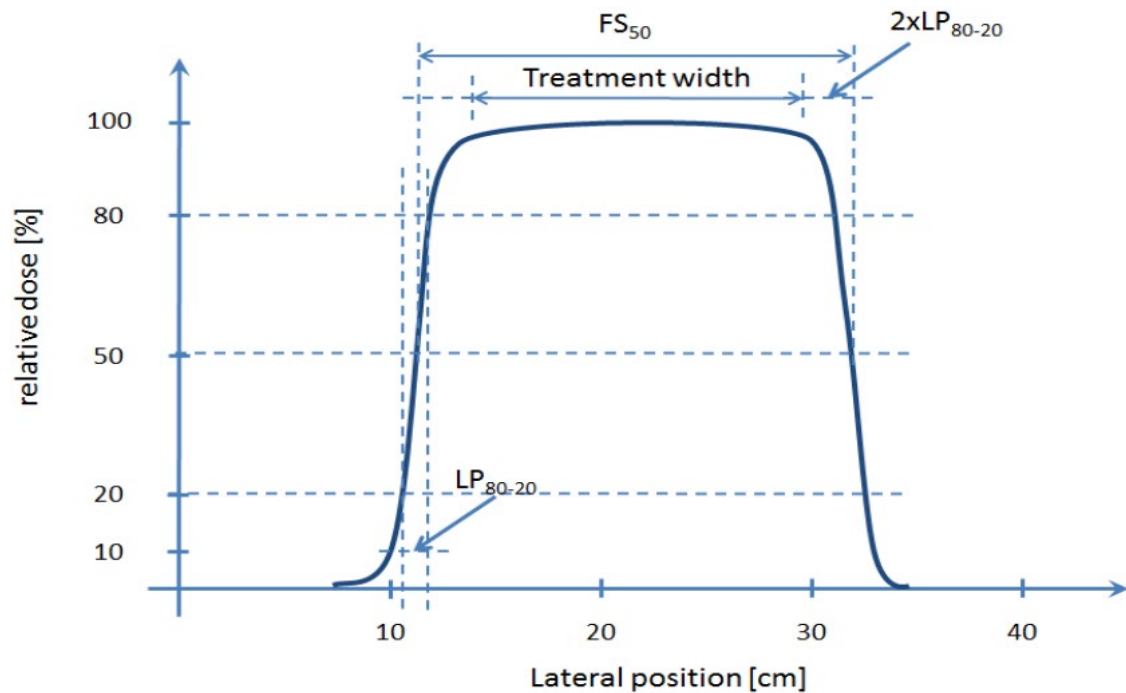

Figure 17: Transverse-dose profile indicating FS$_{50}$, treatment width and the lateral penumbra (80-20%). [63]

3.3.3. Intra-spill Variation

The intra-spill procedure is performed on a yearly basis. To do so, a beam is directed onto a single spot (Figure 19) and the variations in spot position and spot size are filmed over time, by taking 7.5 frames per second with the CCD camera of the Lynx. The parameters analyzed are X/Y spot position and X/Y FWHM changes over time during a spill. This analysis is performed for the 5 key energies both for protons and carbon ions.
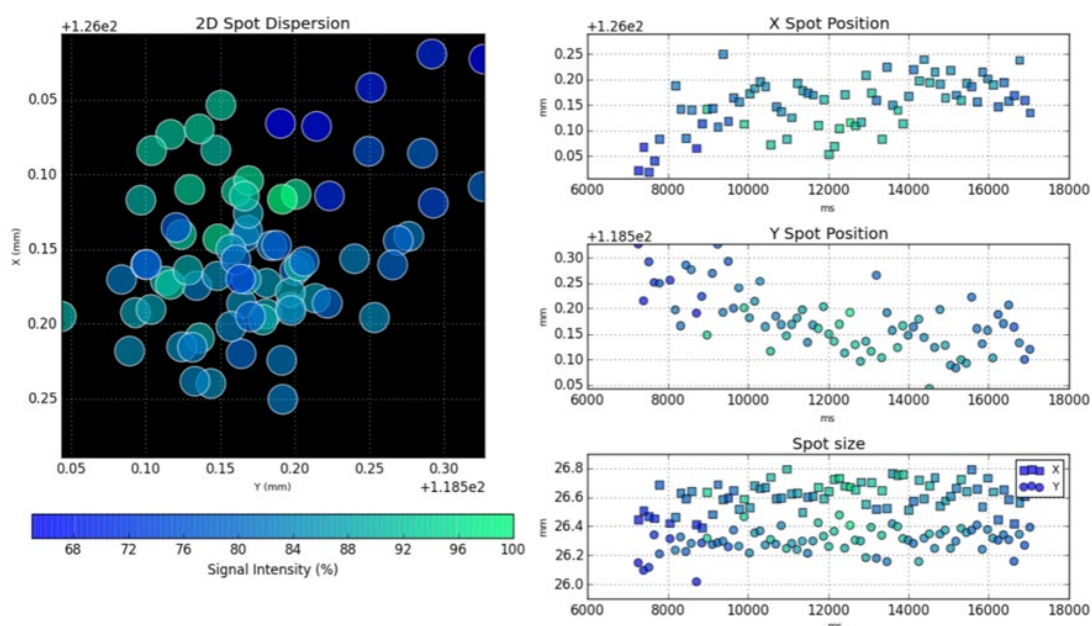

Figure 18: Intra-spill variation analysis. On the left is the 2D dispersion of the spot and the signal intensity. On the right is the variation in spot position and size for X and Y direction. (from MedAustron)

On the left of Figure 19 a 2D spot dispersion can be seen, where the spatial map of the beam's spot positions in two dimensions (X and Y) relative to the isocenter. Each spot is represented as a circle, and its color indicates the signal intensity, with darker blue representing lower intensity and green to cyan representing higher intensity. The signal intensity reflects the relative energy deposition or charge collected by the detector for each spot. Higher intensity indicates stronger beam focus or a more intense beam delivery, while lower values suggest dispersion or reduced beam energy. The "+1.26e2" and "+1.185e2" on the X and Y axes indicate that a constant value (126 mm or 118.5 mm) has been added to the raw X and Y coordinates, respectively. This is done manually in the setup to irradiate the beam at the corner of the detector to reduce wear on high-usage

areas. On the right side the spot position over time for X and Y position as a function of time is depicted. Further, below the spot size (FWHM) is plotted over time.

3.4. Software

While the full details of the algorithms used remain proprietary to IBA, a general description of their functionality is provided here for clarity. Spot sizes and positions are extracted from a two-dimensional Gaussian fit for each spot. [64]

3.4.1. Lynx2D and LynxQA Software

At MedAustron, the Lynx detector's measured data is processed using the Lynx2D software for digitalization and subsequently analyzed with MedAustron's internally developed software, LynxQA (version 3.3). Lynx2D facilitates the acquisition of time-integrated images, allowing exposures of up to 90 seconds, or videos recorded at 7.5 frames per second. [24] The analyzed data is exported into formats like Excel or TXT for further processing.

3.4.2. MyQA

MyQA developed by IBA Dosimetry GmbH (Schwarzenbruck, Germany), is a comprehensive software suite designed for machine and patient-specific quality control. At MedAustron, its primary role is as a database for long-term trend analysis, supported by the myQA Cockpit module. Additionally, myQA provides various other modules such as myQA FastTrack (myQA FT) or Sphinx Plugin (SP) (see below 3.4.2.4 "Sphinx Plugin") for fast measurement and data analysis, and myQA Machines, where the different devices are organized, and the quality can be assured.

3.4.2.1. Acquisition in myQA FastTrack

The medical certified analysis module myQA FT is part of myQA. The intended use is to perform and document QA activities of treatment devices, imaging devices and their accessories. The measurement tab can be seen in Annex Figure 45. It is used with the Lynx detector to perform measurements during installation, acceptance and commissioning phases of a particle therapy center. Images are acquired in the Measurement ribbon (Figure 20), where the Lynx and the calibration files are selected (Figure 20, 1).

Figure 19: Measurement ribbon for myQA FT.

The Frame Duration, which is the exposure time for one image, and the Iris Opening, the aperture opening in percentage, can be set (Figure 20, 2). Then a background measurement can be done, which will be saved for every measurement until the Lynx is disconnected. Three modes are available: Single Shot, Multiple Shot and Movie Mode (Figure 20, 3; Figure 21). Single Shot (or Multiple Shot) acquires one image, resulting in integration over the frame duration. If Multiple Shot is chosen, the specified number of frames over the frame duration are automatically recorded after each other. Movie Mode acquires a movie at 7.5[6]

Figure 20: Different measurement modes for myQA FT.

frames per second, resulting of the integration of 0.133[6] second frames during the number of frames specified.

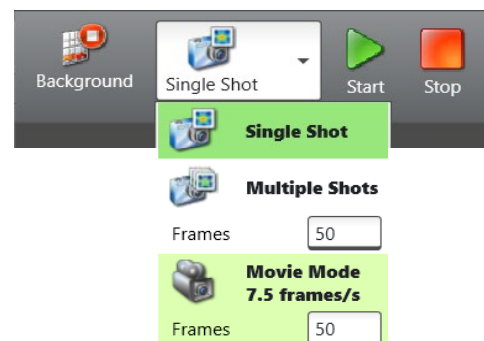### 3.4.2.2. Analysis in myQA FastTrack

After the acquisition the images are then shown in the reference panel in the *Home* ribbon (see Annex, Figure 46) for further processing or analysis. There is also the possibility of exporting and importing images. Two analysis tabs are available: Single and Multiple Image analysis. Multiple Image analysis is only available for spot maps. For Single Image analysis depending on the test, a specific analysis category can be chosen (see Figure 22).
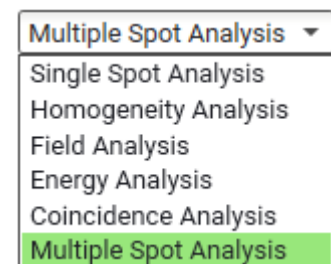

Figure 21: Different image analysis categories in myQA FT, in the Single Image tab.

In the workflows proposed by this thesis, the 2D field analysis and the intra-spill variation analysis are performed here. The following settings are used: **Field Analysis:** Field Size

---

[6] Fixed value

50%, Penumbra Definition 20%-80%, Interpolation none, and No. Penumbras removed 2.0. **Intra-spill variation:** In the Multiple Image tab, Multiple Spot Analysis: All the images containing data are selected and the default settings were used (see Annex Figure 45).

3.4.2.3. Coordinate System in myQA FastTrack

In Figure 23 the coordinate system of the Lynx and its representation in myQA FT can be seen.[7] The Lynx is placed with the bottom on the treatment couch with the tail in the left direction of the beam view.
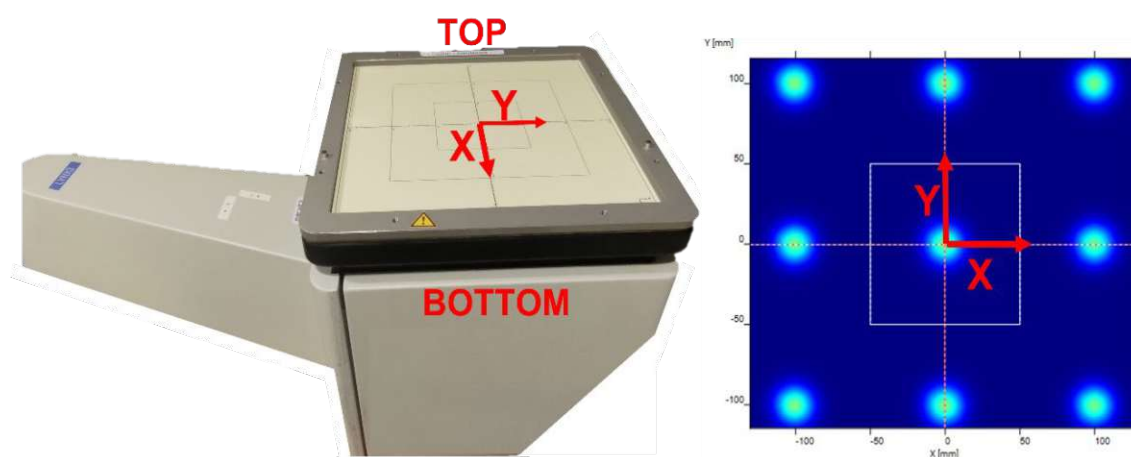
Figure 22: Coordinates illustrated on a Lynx (left) and a spot map in myQA FT (right). (from MedAustron)

3.4.2.4. Sphinx Plugin

Sphinx Plugin (SP) is another software in myQA for acquiring and analyzing beam parameters measured with the Lynx setup in combination with the Sphinx. The Sphinx device, a passive element made of RW3 material fixed in a carbon frame. RW3 is a phantom, which is water-equivalent for proton and carbon ions, to for example vary the measuring depth in increments of 1 mm slabs.

The plugin is used for periodic positioning and beam delivery QA. Furthermore, SP is used on daily QA for VBL without the Sphinx. But in this thesis, it will be used to acquire and analyze spot maps.

---

[7] In contrast, the coordinate system of LynxQA has a 90° clockwise rotation to the coordinate system of myQA FT. (see section 3.4.1 Spot Map)

The acquisition as well as the analysis can be done in the same tab. An individual test is created, where the region of interest is selected, which are the 9 spot positions mentioned in section 3.3.1 "Spot Map" (see Annex, Figure 47). Additionally, the thresholds for each beam parameter are defined. The parameters analyzed are given and cannot be chosen. The Lynx is always oriented in a way that its own image coordinates are aligned to the beam coordinate system at MedAustron. To keep the same setup pattern, a 90° rotation in the SP test was implemented[8].

Afterwards, the test is shown in the "Test Run" tab in myQA Machines. Here the images can be measured with the Lynx device. There is an option to manually save the analysis or by selecting "Finish" to save it in the myQA database. Furthermore, an image can be manually imported and analyzed again. (Figure 24)
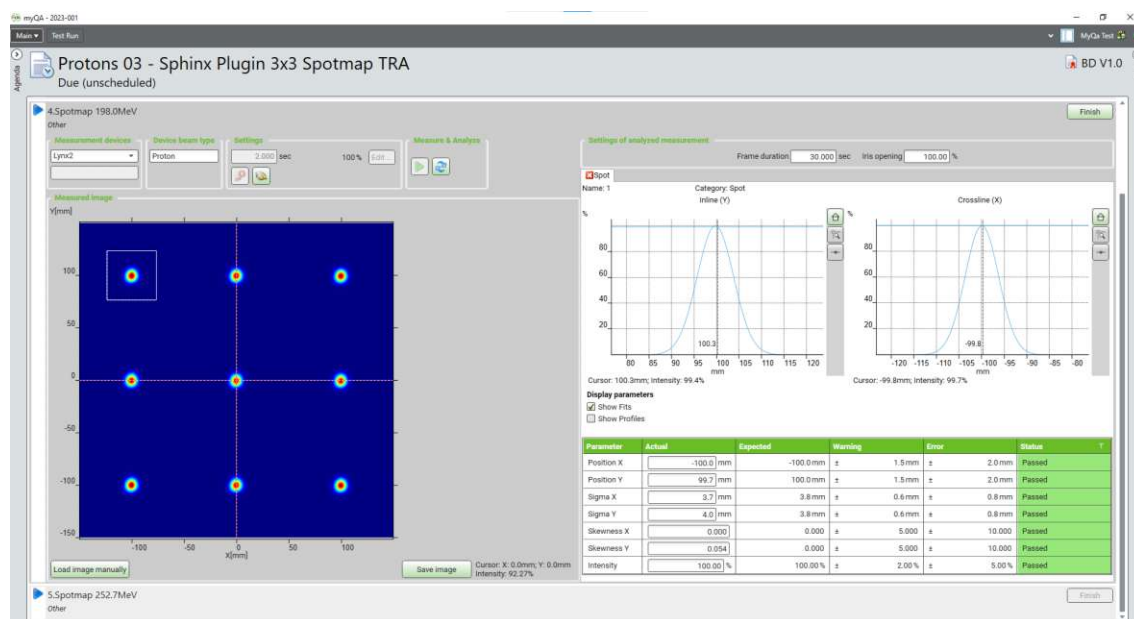

Figure 23: Example of a Sphinx Plugin test of a proton spot map with 198.0 MeV. Images can be recorded with the Lynx device on the top or manually imported on the bottom.

---

[8] This is automatically done in myQA FT.

3.5. Current QA Workflows "LynxQA"

This chapter outlines the existing beam optics quality assurance (QA) workflows at MedAustron. These workflows encompass the analysis of spot maps, two-dimensional homogeneous fields, and intra-spill variations. All measurements are acquired using the Lynx2D software and analyzed with the LynxQA software.

3.5.1. Spot Map Procedure

Spot map analysis is conducted monthly at the isocenter in air for five key energies. Additionally, annual evaluations are performed for 20 major proton energies and 16 major carbon ion energies.

Using the setup described in 3.2 Equipment: Lynx, the Lynx2D software is operated via remote desktop access. The process begins with a background measurement, followed by beam measurements across the designated energies. The resulting DICOM files are saved and subsequently analyzed using the LynxQA software. The analysis yields data on spot positions and full width at half maximum (FWHM), which are stored in an Excel file. This file is then imported into the myQA system, where the parameters are checked against predefined thresholds. If the results are within acceptable limits, the data is saved in the database for long-term trend analysis (see Annex, Figure 48).

3.5.2. 2D Homogenous Field Procedure

Homogeneous field analysis is conducted monthly for a 10×10 cm² field size. Annually, the evaluation extends to maximum field sizes, which vary depending on the beamline. The maximum field sizes are 20×20 cm² for the horizontal beamline (HBL), 17×18.8 cm² for the vertical beamline (VBL), and 12×20 cm² for the gantry-equipped room. For each assessment, the five key energies are measured for both particle types.

The field is recorded using the Lynx device with the same setup as mentioned above (see 3.2 Equipment: Lynx). Initially, the background is measured using the Lynx2D software. Subsequently, beam measurements are performed until the entire field is irradiated. The resulting DICOM files are analyzed with the LynxQA software, and the parameters are

exported in TXT format. These values are copied into an Excel template for verification. Once the parameters are deemed acceptable, the Excel file is imported into myQA, where the data undergoes a secondary validation before being saved in the database for trend analysis.

3.5.3. Intra-spill Variation Procedure

The intra-spill procedure is performed on a yearly basis and measured with the Lynx device at isocenter with the same setup as described above (3.2 Equipment: Lynx). To avoid damage to sensitive regions of the Lynx screen, the device is placed off-center. At least three complete beam spills directed onto a single spot are recorded using the Lynx2D software at a frame rate of 7.5 Hz.

The acquired intra-spill videos are analyzed using the LynxQA software. The analysis involves saving results into an Excel template for further evaluation. To ensure reliable data, frames recorded at the beginning and end of each spill, where outliers are more likely, are excluded from the analysis. The software determines which frames exceed a predefined intensity threshold, and only these frames are used. The analysis considers a range of percentages of frames (100%, 90%, 80%, 70%, and 50%), but for long-term trend analysis, only the 90% frame data is saved into the myQA database.

3.6. Measurements LynxQA vs MyQA FT

To ensure that myQA FT can reliably replace Lynx2D and LynxQA for both data acquisition and analysis, a series of comparative measurements were performed. These measurements were conducted for each of the five key energies and two particle types to evaluate beam parameters. The evaluations included spot maps, measured across five iterations, and two-dimensional homogeneous fields, measured over three iterations. Each measurement utilized the Lynx device, first in combination with the Lynx2D software for data acquisition and LynxQA software for analysis, and subsequently with myQA FT for both acquisition and analysis. For the intra-spill variation analysis, only the results derived from the spot maps were considered, as these inherently included the spot position and spot size comparisons.

The comparative analysis was carried out by directly comparing the parameters calculated by the two software systems. The Lynx-generated images, processed as DICOM files via either Lynx2D or myQA FT, were subsequently analyzed with LynxQA and myQA FT to compute beam parameters. The resulting values were exported in either Excel or TXT format and organized using a Python script, which grouped the parameters based on acquisition software, analysis software, energy, and beam parameters. These values were then compared both against each other and against the expected values for beam parameters, as specified in 10.1 Expected values at MedAustron.

3.7. Uncertainty Discussion

When comparing the analyses performed by LynxQA and myQA FT to the expected values and to each other, the measurement uncertainties associated with each system must be considered. LynxQA rounds parameter values to two decimal places (= ±0.01 mm), whereas myQA FT rounds the CAX (Central Axis) measurements to the nearest whole pixel, equivalent to ±0.25 mm.

Furthermore, the calibration and offset correction of the Lynx device, as determined during its calibration at MedAustron, introduces an uncertainty of ±0.1 mm. The accuracy of the in-room laser setup was also found to contribute an uncertainty of ±0.2 mm. Additionally, the resolution of the Lynx detector is 0.5 mm, which must be accounted for in the uncertainty calculations.

Depending on whether the comparison is made against the expected values or between the two software systems, the total uncertainty budget varies. This is detailed in Table 2 and Table 3.

Table 3: Absolute measurement uncertainty budget when comparing to the expected value.

Source of uncertainty	Absolute magnitude
LynxQA rounding uncertainty	±0.01 mm
Lynx calibration and offset uncertainty	±0.1 mm
Lynx positioning uncertainty	±0.2 mm
Lynx resolution uncertainty	±0.25 mm
Total measurement uncertainty budget	**±0.3 mm**

Table 4: Absolute measurement uncertainty budget when comparing software systems.

	Absolute measurement uncertainty budget
LynxQA rounding uncertainty	±0.01 mm
MyQA rounding uncertainty (CAX only)	±0.25 mm
Lynx resolution uncertainty (double, due to dual measurements)	2 x ±0.25 mm
Total measurement uncertainty	**±0.35 mm (CAX: ±0.43 mm)**

4.   Results

This section presents the comparison of parameter analysis between two workflows: the previous workflow, where data acquisition was performed using Lynx2D in combination with the Lynx device and analyzed later with LynxQA, and the proposed workflow, where myQA FT was used for both acquisition and analysis.

All data presented was obtained using the Lynx device in conjunction with image acquisition software. Data acquired with LynxQA was analyzed using Lynx2D, while data acquired with myQA FT was analyzed with myQA FT. The beam parameters analyzed by the two workflows were compared to each other and to the expected values.

In this section, the notation for each acquisition and analysis tool is as follows: when Lynx2D was used, it is denoted as "LynxQA (L)", and when myQA FT was used, it is denoted as "myQA (M)".

4.1.   Measurements

4.1.1. Spot Maps and Intra-spill Variation

4.1.1.1.Spot Position

In this section the difference in spot position to the expected value obtained with Lynx2D/LynxQA and myQA FT as well as their difference for protons is presented. Similar results were found for carbon ions and results are available in the annex for completeness. (Annex, 10.2 Plots with Carbon Ions)

Figure 25 (top) illustrates the difference to the expected value for each software, spot position, and energy, along with the warning and fail thresholds. The bottom panel shows the differences between the two software, where the average over all spots per energy is depicted as dotted lines. The blue line represents the uncertainty budget. (For carbon ions see Annex, Figure 37) The averages differences across all spots and energies between the software and the expected values are summarized in Table 4 for x and y direction.
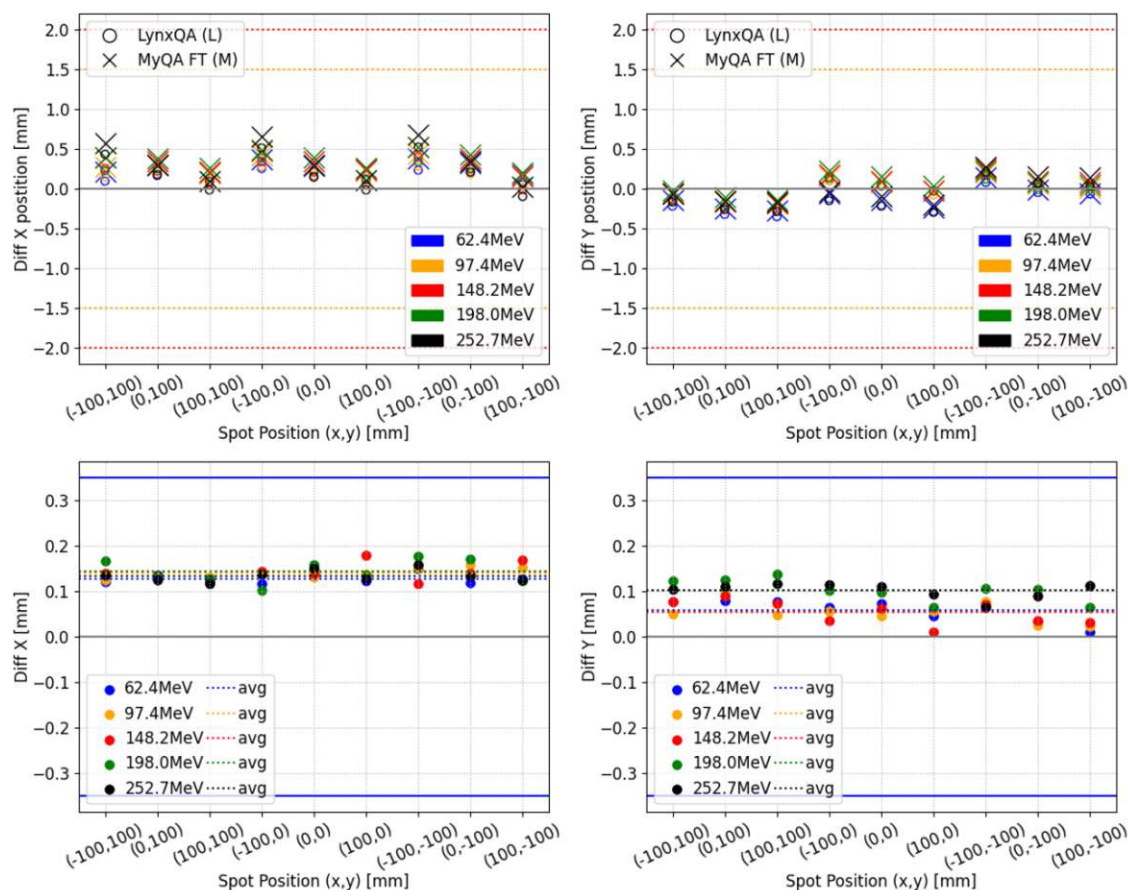
Figure 24: (Protons) Top: X/Y Spot position: Difference to expected value for myQA FT(M) and LynxQA(L) Bottom: X/Y absolute difference between myQA FT(M) and LynxQA(L), where the average over all spots per energy is plotted with dotted lines.

Table 5: Summary of differences in spot position between LynxQA and myQA FT, and relative to the expected values, averaged over all spots and energies.

SPOTMAPS		Spot Position		
		Difference to the expected value		Difference LynxQA (L) vs myQA FT (M)
		LynxQA (L)	myQA FT (M)	
Protons	X	0.19±0.13 mm	0.32±0.14 mm	0.14±0.02 mm
	Y	-0.08±0.16 mm	-0.01±0.15 mm	0.07±0.03 mm
Carbons	X	-0.10±0.17 mm	0.04±0.17 mm	0.14±0.02 mm
	Y	-0.01±0.17 mm	-0.02±0.18 mm	-0.01±0.03 mm

4.1.1.2. Full Width at Half Maximum

The same approach was applied to analyze the differences in the full width at half maximum (FWHM) values. Results for protons are presented in Figure 26 , with similar findings for carbon ions shown in the annex (Figure 38) and summarized in Table 5.
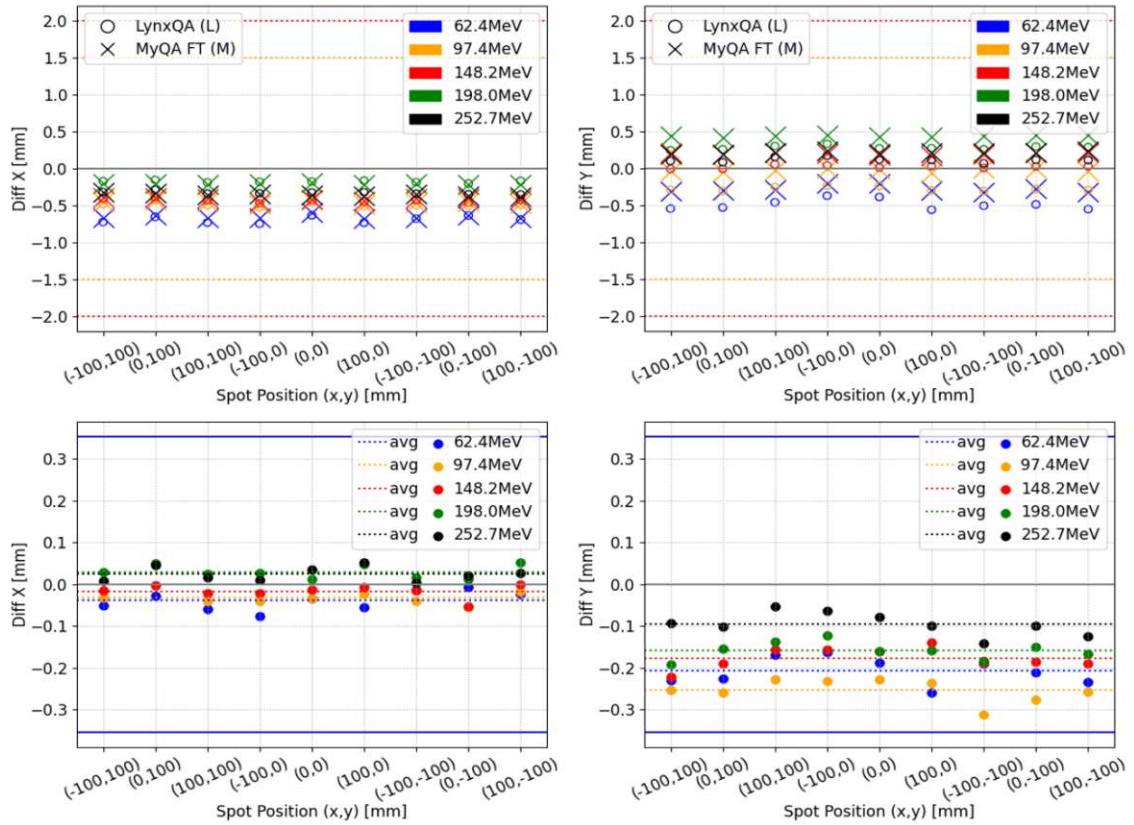

Figure 25: (Protons) Top: X/Y FWHM: Difference to expected value for LynxQA(L) and myQA FT(M). Bottom: X/Y Absolute difference between myQA FT(M) and LynxQA (L), where the average over all spots per energy is plotted with dotted lines.

Table 6: Summary of differences between LynxQA and myQA FT and to the expected values, averaged over all spots and all energies, for spot size (FWHM).

SPOTMAPS		FWHM		
		Difference to the expected value		**Difference LynxQA (L) vs myQA FT (M)**
		LynxQA (L)	**myQA FT (M)**	
Protons	X	-0.43±0.17 mm	-0.42±0.15 mm	-0.01±0.03 mm
	Y	-0.07±0.28 mm	0.11±0.24 mm	-0.18±0.06 mm
Carbons	X	-0.33±0.06 mm	-0.51±0.17 mm	0.18±0.09 mm
	Y	-0.44±0.17 mm	-0.57±0.21 mm	0.12±0.11 mm

4.1.2. 2D Homogenous Field

4.1.2.1.Central Axis

This subsection examines the differences in the central axis (CAX) between the expected values and the measurements using LynxQA and myQA FT. Results for protons are shown in Figure 27 (carbons: Annex, Figure 39) and summarized in Table 6.
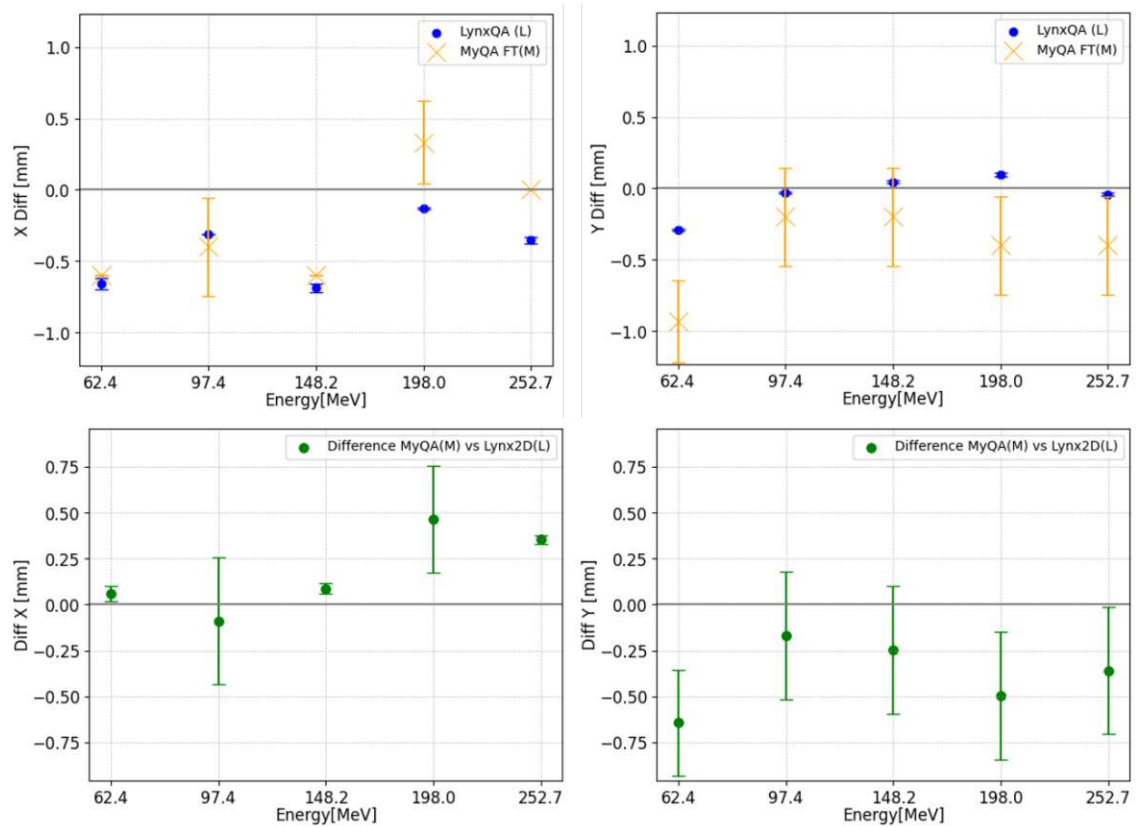

Figure 26 : (Protons) Top: X/Y CAX: Difference to the expected value for LynxQA(L) and myQA FT(M). Bottom: X/Y absolute difference between myQA FT(M) and LynxQA (L), where the average over all spots per energy is plotted with dotted lines.

The larger deviation from the expected value observed with myQA FT may be attributed to its algorithm rounding calculations to whole pixels, introducing an uncertainty of ±0.25 mm.

Table 7: Summary of differences in central axis (CAX) between LynxQA (L) and myQA FT (M), and relative to the expected values, averaged over all spots and energies.

2D Homogeneous Field		CAX		
		Difference to the expected value		Difference LynxQA (L) vs myQA FT (M)
		LynxQA (L)	myQA FT (M)	
Protons	X	-0.43±0.21 mm	-0.25±0.37 mm	0.18±0.20 mm
	Y	-0.04±0.13 mm	-0.43±0.27 mm	-0.38±0.17 mm
Carbons	X	-0.52±0.22 mm	-0.54±0.29 mm	-0.02±0.16 mm
	Y	-0.34±0.08 mm	-0.48±0.18 mm	-0.14±0.18 mm

4.1.2.2. Field Size at 50%

This subsection evaluates the differences in the field size at 50% (FS50), where the results for protons are shown in Figure 28 (carbons: Annex, Figure 40) and in Table 7.
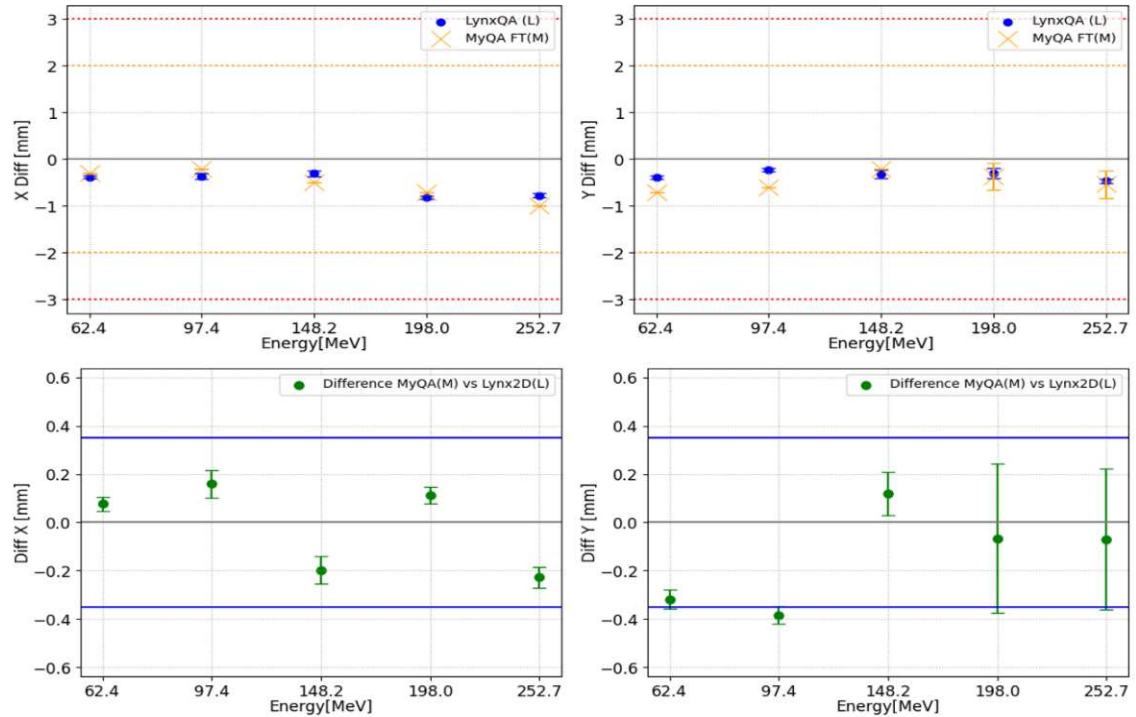

Figure 27 : (Protons) Top: X/Y FS50: Difference to the expected value for LynxQA(L) and myQA FT(M). Bottom: X/Y absolute difference between myQA FT(M) and LynxQA (L), where the average over all spots per energy is plotted with dotted lines.

Although the documentation for myQA FT does not explicitly state this, it is plausible that FS50 values are rounded to whole pixels, as observed with the CAX.

Table 8: Summary of differences between LynxQA and myQA FT and to the expected values, averaged over all spots and all energies, for FS50.

2D Homogeneous Field		FS50		
		Difference to the expected value		Difference LynxQA (L) vs myQA FT (M)
		LynxQA (L)	myQA FT (M)	
Protons	X	-0.52 ± 0.22 mm	-0.54 ± 0.29 mm	-0.02 ± 0.16 mm
	Y	-0.34 ± 0.08 mm	-0.48 ± 0.18 mm	-0.14 ± 0.18 mm
Carbons	X	0.24 ± 0.08 mm	0.0 ± 0.06 mm	-0.24 ± 0.05 mm
	Y	0.14 ± 0.10 mm	-0.12 ± 0.07 mm	-0.26 ± 0.10 mm

4.1.2.3. Penumbra

This subsection evaluates the differences in the left and right side of the penumbra, where the results for protons are shown in Figure 29 / Figure 30 (carbons: Annex, Figure 42 / Figure 41) and Table 9 / Table 8.
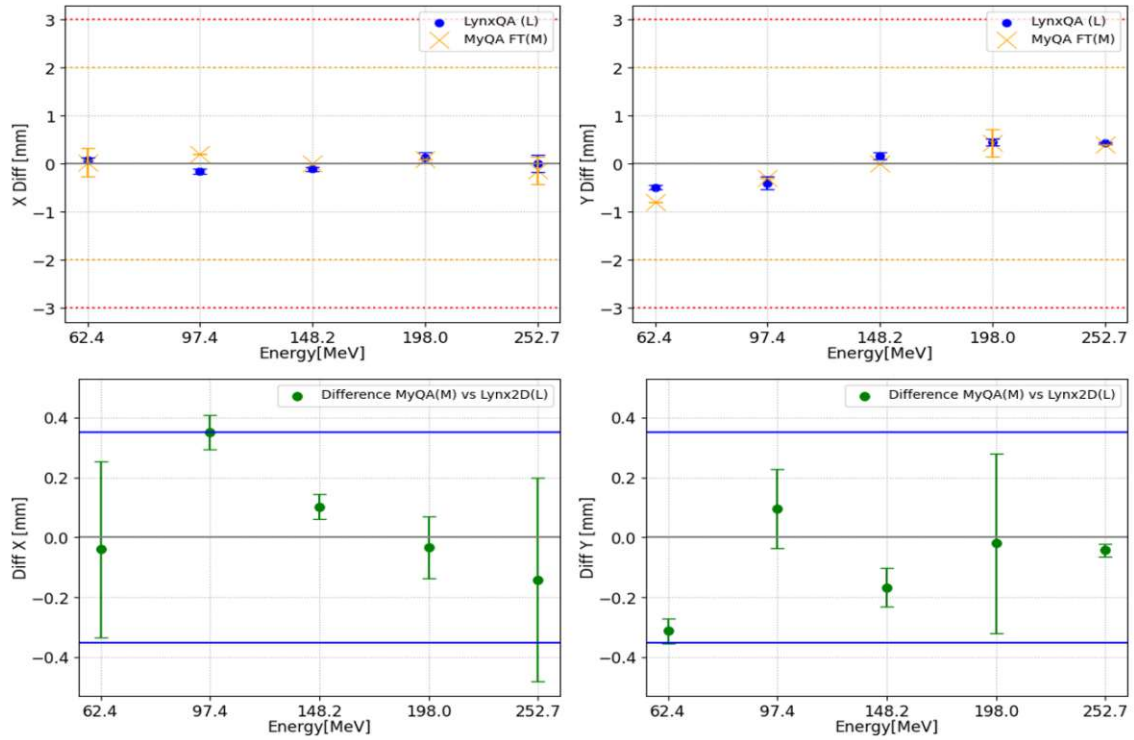

Figure 28 : (Protons) Top: X/Y Penumbra (left side): Difference to the expected value for LynxQA(L) and myQA FT(M). Bottom: X/Y Absolute difference between myQA FT(M) and LynxQA (L), where the average over all spots per energy is plotted with dotted lines.

Table 9: Summary of differences between LynxQA and myQA FT and to the expected values, averaged over all spots and all energies, for Penumbra (left side).

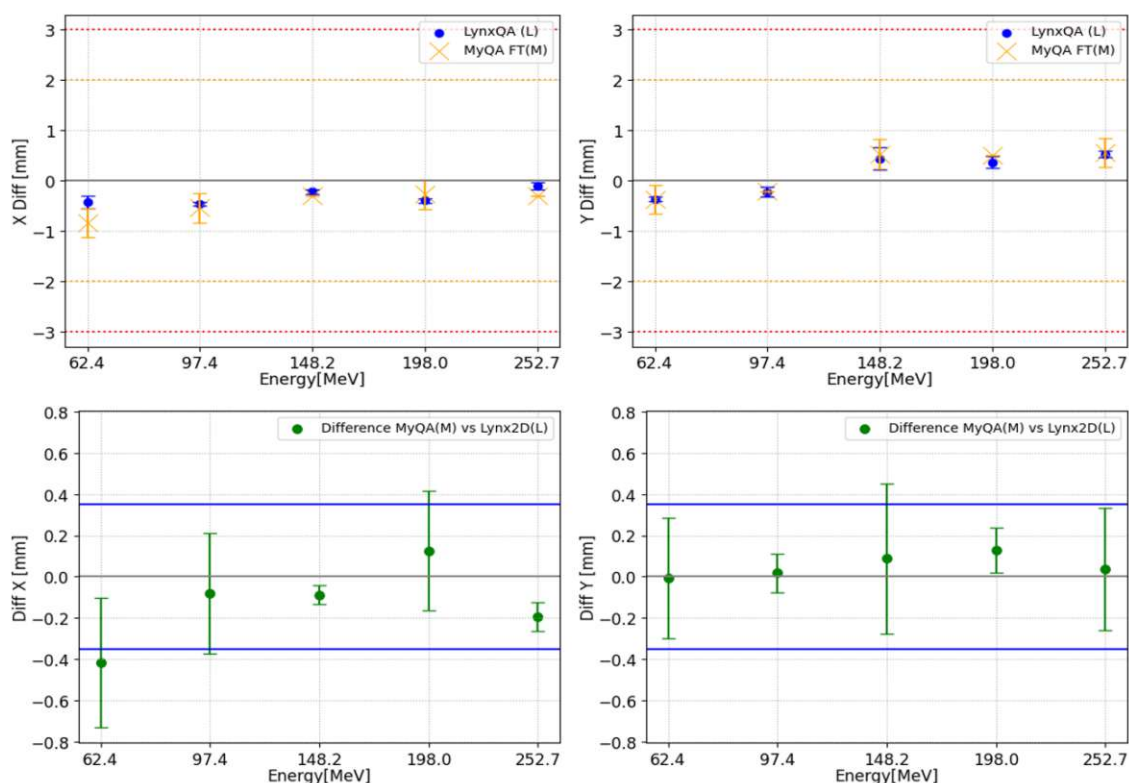| 2D Homogeneous Field		Penumbra (Left Side)		
		Difference to the expected value		Difference LynxQA (L) vs myQA FT (M)
		LynxQA (L)	myQA FT (M)	
Protons	X	-0.01 ± 0.11 mm	0.04 ± 0.11 mm	0.05 ± 0.17 mm
	Y	0.04 ± 0.40 mm	-0.05 ± 0.46 mm	-0.09 ± 0.14 mm
Carbons	X	-0.20 ± 0.15 mm	-0.36 ± 0.16 mm	-0.16 ± 0.22 mm
	Y	-0.10 ± 0.16 mm	-0.25 ± 0.09 mm	-0.15 ± 0.12 mm

Figure 29 : (Protons) Top: X/Y Penumbra (right side): Difference to the expected value for LynxQA(L) and myQA FT(M). Bottom: X/Y Absolute difference between myQA FT(M) and LynxQA (L), where the average over all spots per energy is plotted with dotted lines.

Table 10: Summary of differences between LynxQA and myQA FT and to the expected values, averaged over all spots and all energies, for Penumbra (right side).

2D Homogeneous Field		Penumbra (Right Side)		
		Difference to the expected value		Difference LynxQA (L) vs myQA FT (M)
		LynxQA (L)	myQA FT (M)	
Protons	**X**	-0.32 ± 0.13 mm	-0.45 ± 0.22 mm	-0.13 ± 0.18 mm
	Y	0.15 ± 0.37 mm	0.21 ± 0.4 mm	0.05 ± 0.05 mm
Carbons	**X**	-0.12 ± 0.08 mm	-0.26 ± 0.23 mm	-0.14 ± 0.20 mm
	Y	-0.18 ± 0.10 mm	-0.21 ± 0.2 mm	-0.02 ± 0.16 mm

4.1.2.4. Symmetry

This subsection evaluates the differences in the symmetry, where the results for protons are shown in Figure 31 (carbons: Annex, Figure 43) and Table 10.
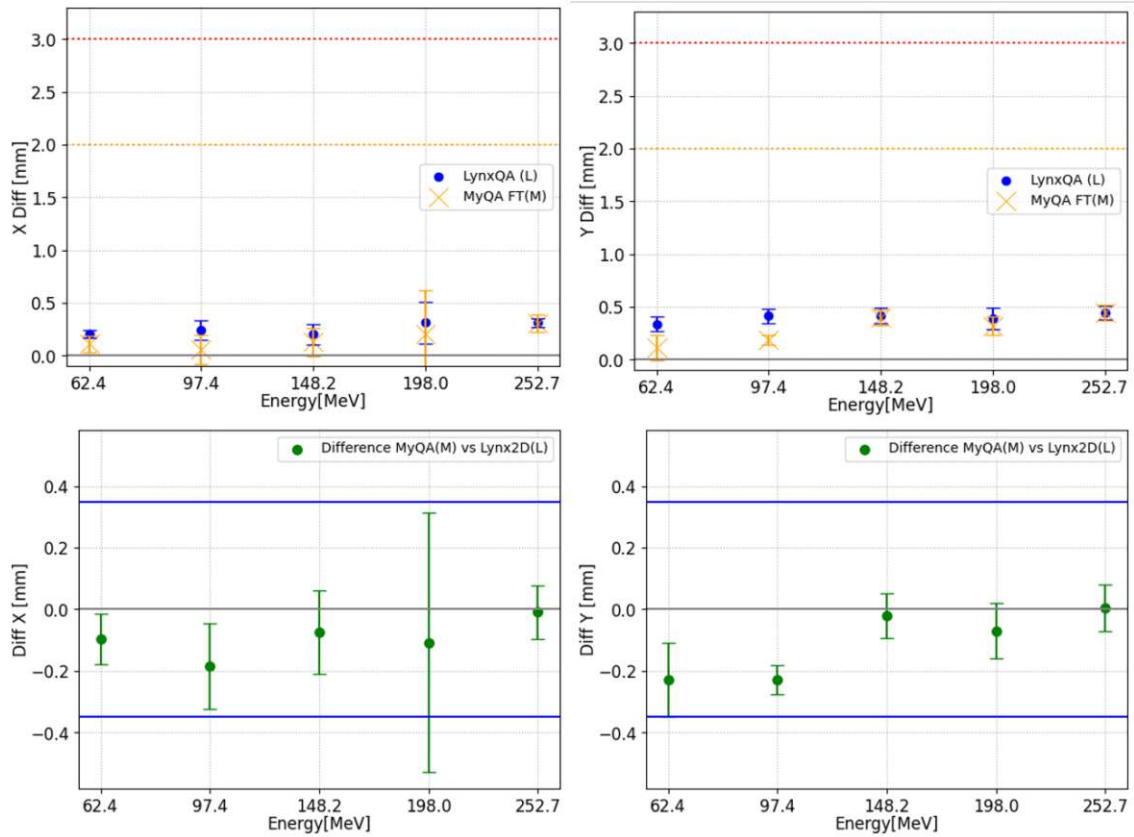

Figure 30 : (Protons) Top: X/Y Symmetry: Difference to the expected value for LynxQA(L) and myQA FT(M). Bottom: X/Y Absolute difference between myQA FT(M) and LynxQA (L), where the average over all spots per energy is plotted with dotted lines.

Table 11: Summary of differences between LynxQA and myQA FT and to the expected values, averaged over all spots and all energies, for Symmetry.

2D Homogeneous Field		Symmetry		
		Difference to the expected value		Difference LynxQA (L) vs myQA FT (M)
		LynxQA (L)	myQA FT (M)	
Protons	X	0.26 ± 0.05 %	0.16 ± 0.09 %	-0.09 ± 0.06 %
	Y	0.40 ± 0.04 %	0.29 ± 0.13 %	-0.11 ± 0.10 %
Carbons	X	0.16 ± 0.09 %	0.11 ± 0.1 %	-0.04 ± 0.11 %
	Y	0.18 ± 0.09 %	0.23 ± 0.11 %	0.05 ± 0.16 %

4.1.2.5.Homogeneity

This subsection evaluates the differences in the homogeneity over the treatment width, where the results for protons are shown in Figure 32 (carbons: Annex, Figure 44) and Table 11.
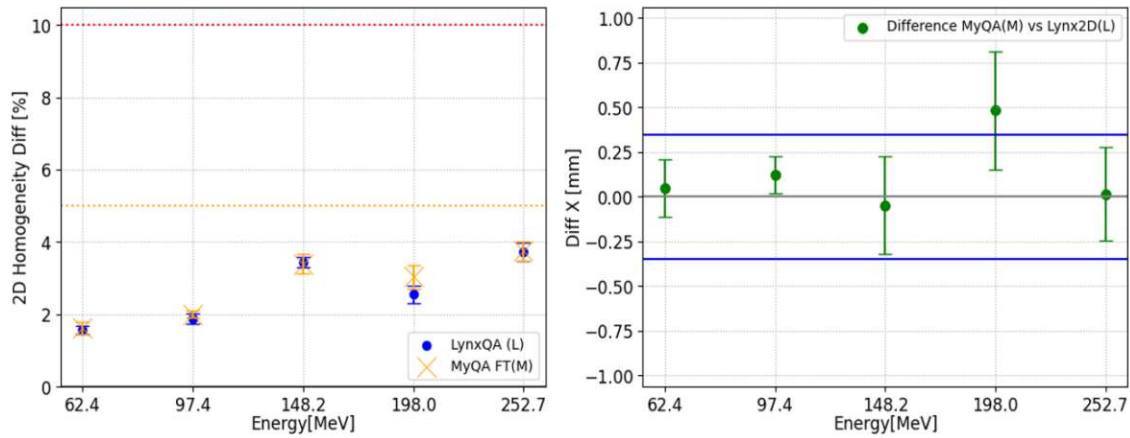

Figure 31 : (Protons) Top: 2D Homogeneity: Difference to the expected value for LynxQA(L) and myQA FT(M). Bottom: X/Y Absolute difference between myQA FT(M) and LynxQA (L), where the average over all spots per energy is plotted with dotted lines.

Table 12: Summary of differences between LynxQA and myQA FT and to the expected values, averaged over all spots and all energies, for Symmetry.

2D Homogeneous Field	Symmetry		
	Difference to the expected value		Difference LynxQA (L) vs myQA FT (M)
	LynxQA (L)	myQA FT (M)	
Protons	2.64 ± 0.84 %	2.76 ± 0.82 %	0.12 ± 0.19 %
Carbons	4.50 ± 1.11 %	4.80 ± 1.12 %	0.30 ± 0.20 %

4.2. Proposed Workflows

In this chapter, the proposed workflows incorporating myQA and its plugins are introduced for each test, spot maps, 2D homogenous field and intra-spill variation.

4.2.1. Spot Maps

To streamline the process and eliminate the need for two separate pieces of software for acquisition and analysis, myQA and its Sphinx Plugin can be utilized.

In the proposed workflow, acquisition as well as the analysis of spot maps are carried out using Sphinx Plugin. Prior to the measurement, a test is created in myQA for each energy and particle type (see section 3.4.2.4 "Sphinx Plugin"). Within these tests, the Sphinx Plugin is configured to identify the nine spots in the image and the thresholds for warnings or failures are predefined. The Lynx setup is identical as previously described (see section 3.2 "Equipment: Lynx").

Initially, the Lynx connection is established, and background acquisition is performed within the test designed for measuring the spot map of the highest energy. SP automatically analyzes the parameters, indicating whether they fall within acceptable limits.

Since one test is needed for each of the energies and each test requires an independent background measurement, a workaround is implemented. One test is used to measure the spot maps for all energies (Figure 33, 1). In between measurements the DICOM image acquired is saved by the user in a temporary folder (Figure 33, 2). Once all the energies are measured, the DICOM data is imported back into the dedicated test according to its energy (Figure 33, 3). Then the values are saved in the myQA database by selecting "Finish" (Figure 33, 4). The process is then repeated for carbon ions. It is important to note that when switching to the next test, data within SP is lost[9] while background information is retained.

---

[9] If the "Finish" button was selected and the user switches to the next test, the data is not lost, only the background.
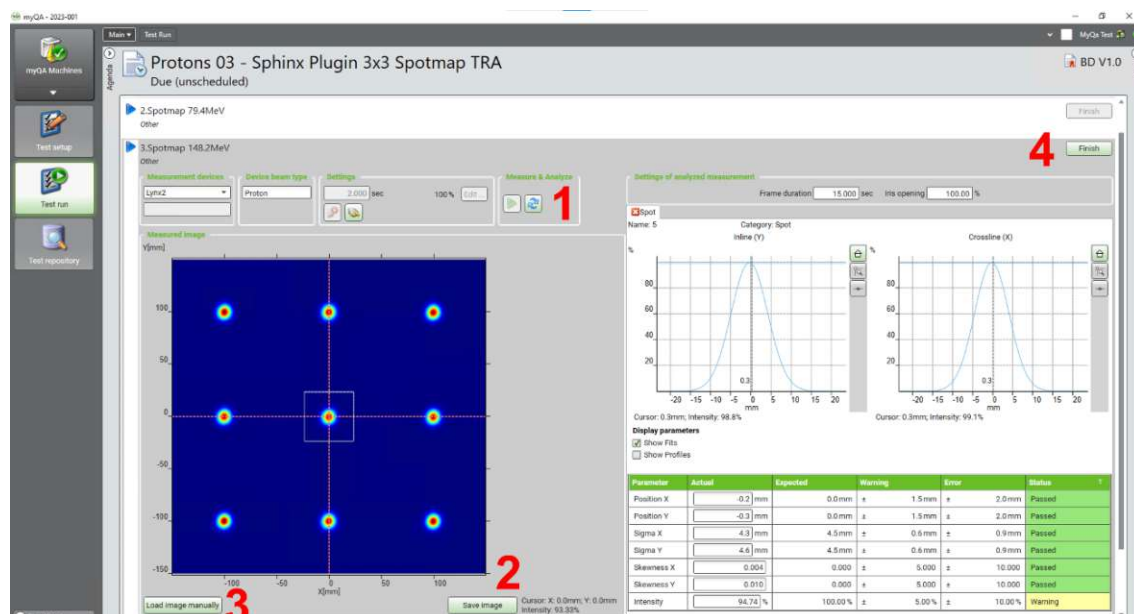
Figure 32: Sphinx Plugin acquisition and analysis window of a proton spot map with 148.2 MeV.

4.2.2. 2D Homogenous Field

Similar to the proposed workflow for the spot maps, the 2D field is measured and analyzed with the myQA software, but utilizing FT.

Using the previously described setup (see section 3.2 "Equipment: Lynx"), the field is measured with FT and automatically stored within the plugin for later analysis. In the analysis tab, the "Field Analysis" option is chosen (see Figure 34, 1), and specific settings are configured: Field Size at 50%, Penumbra Definition ranging from 20% to 80%, no interpolation, and number of penumbras removed: 2.0 (2x LP_{80-20}) (see Figure 34, 2; see section 3.3.2 "2D Homogeneous Field").
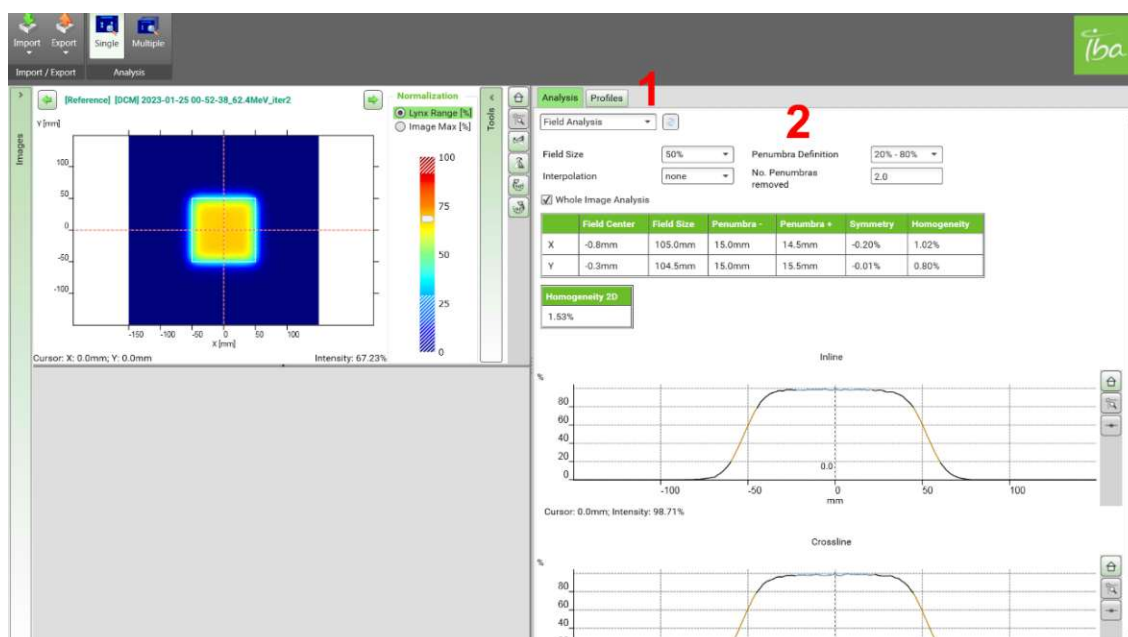
Figure 33: MyQA FT analysis tab. Measurement of a 2D homogenous field with proton beams of 62.5 MeV. On the right the field analysis is shown. No export button is available.

However, as IBA has not yet implemented an export feature for the field analysis in FT, a Python script had been written. This script captures a screenshot of the FT analysis window and extracts the values using Optical Character Recognition (OCR).

Firstly, the user selects the settings for the field analysis. Then in the script the area where the OCR should read out the values need to be selected. This is done by clicking on "Select new ROI" (Region of Interest) (see Figure 35, 1). Using the mouse, the user selects the area and after pressing enter the data is shown (see Figure 35, 2 and 3). A TXT file is created in the background, where the locations of the ROI's are saved. If the recognition is incorrect the screenshot can be modified into a black and white version, or the resolution can be adjusted. There is also a possibility to select a different segmentation mode in the OCR (see Figure 35, 4). For further inspection the extracted screenshot and extracted data can be checked at all times (see Figure 35, 5). Then when the data is correctly recognized the user selects "Start Extraction". The extracted data is shown and can be adjusted if the OCR is still faulty (see Figure 35, 6). If everything is correct the data is saved in a created Excel template. This is repeated for the other energies, where the energy selection in the script is automatically adjusted to the next lower energy. Furthermore, depending on proton or carbon and monthly and yearly settings in the script (see Figure 35, 7) the name and the energies are adjusted in the excel template.

Afterwards, the excel can be imported into myQA, where the data is checked against thresholds and saved for trend analysis.
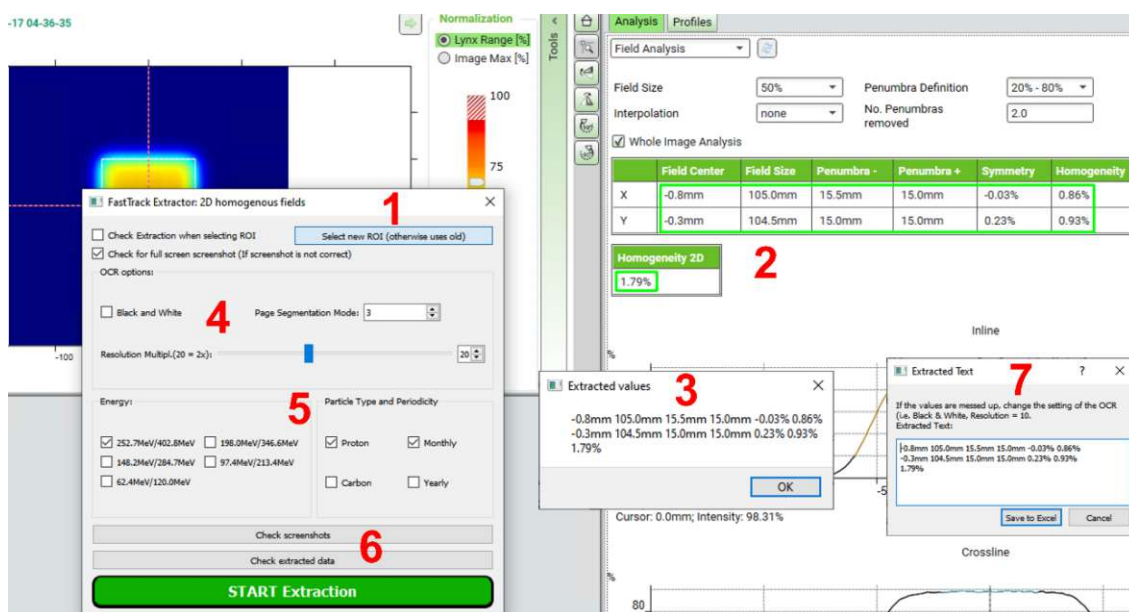

Figure 34: Description for the script to extract the field analysis data.

4.2.3. Intra-spill Variation

Similar to the 2D field workflow, this process uses myQA for both acquisition and analysis, using the FT plugin. The setup involves the Lynx device connected to the laptop, as described previously (see section "3.2 Equipment: Lynx").

When measuring the intra-spill, "Movie Mode" is selected, capturing 7.5 frames per second (see 3.4.2.1 Acquisition in myQA FastTrack). The frame duration is automatically set to 0.133 seconds. Only the number of frames can be chosen. About 150 frames[10] is sufficient enough to measure one whole spill. After the measurement the frames are automatically stored in a folder within FT as DICOM files. Then, the beam is stopped and resumed for the next spill. Afterwards, empty images, identified by a signal lower than 5% of the Lynx range on all pixels, are removed by using the "Delete Black Images" function on the folder. Then the images in each folder are analyzed using "Multiple Image" and "Multiple Spot" analysis, generating an Excel file containing X/Y spot

---

[10] If too many frames are used, there could be a memory issue and myQA crashes.

positions, X/Y FWHM, and other parameters. The data is copied into an Excel template. There the above-mentioned percentage-ranges (50%, 70%, 80%, 90%, 100%) are calculated, based on the "CNT" parameter, indicating the amplitude maximum of a 1D fit of the spot in one frame. The Excel template is imported into myQA for long-term analysis of the 90% frame threshold parameters.

5.   Discussion

In this chapter the measurements of the comparison between LynxQA and myQA workflow is discussed and the proposed workflow and their advantages for each test is compared to the previous version.

5.1.   Measurements

The data acquired with Lynx2D was analyzed with LynxQA and the data analyzed with myQA FT was acquired with myQA FT.

The **spot position** measurements indicate that both LynxQA and myQA FT exhibit a high degree of accuracy relative to the expected values, with differences well within the defined tolerance thresholds. For protons, the average difference to the expected value in the x-direction was 0.19 ± 0.13 mm for LynxQA and 0.32 ± 0.14 mm for myQA FT. Similarly, in the y-direction, these differences were -0.08 ± 0.16 mm and -0.01 ± 0.15 mm, respectively. These findings demonstrate that both software systems are capable of reliably determining spot positions, with myQA FT showing slightly larger deviations in the X direction. However, the overall differences between the two software systems, 0.14 ± 0.02 mm in x and 0.07 ± 0.03 mm in Y, remain well within the uncertainty budget.

The **FWHM** analysis shows comparable performance between LynxQA and myQA FT. For protons, the X direction differences were -0.43 ± 0.17 mm (LynxQA) and -0.42 ± 0.15 mm (myQA FT), while the Y direction results revealed slightly higher variability: -0.07 ± 0.28 mm (LynxQA) versus 0.11 ± 0.24 mm (myQA FT). The absolute differences between the workflows, -0.01 ± 0.03 mm (X) and -0.18 ± 0.06 mm (Y), highlight strong consistency, with minimal impact on clinical beam quality.

The **CAX** deviations provide critical insights into central beam alignment. Results reveal a larger deviation in myQA FT compared to LynxQA, particularly in the Y direction for protons. Specifically, LynxQA yielded -0.04 ± 0.13 mm (Y) and -0.43 ± 0.21 mm (X), while myQA FT reported -0.43 ± 0.27 mm (Y) and -0.25 ± 0.37 mm (X). These differences between workflows (0.18 ± 0.20 mm in X and -0.38 ± 0.17 mm in Y) align with the known

limitations of pixel rounding in myQA FT) as mentioned in section 4.1.2.1 "Central Axis" (4.1.2.2 "Field Size at 50%"), contributing to an added uncertainty of ±0.25 mm.

The evaluation of **FS50** differences highlights minor deviations between LynxQA and myQA FT. For protons, LynxQA exhibited deviations of −0.52±0.22 mm (X) and −0.34±0.08 mm (Y) relative to the expected values, while myQA FT showed −0.54±0.29 mm (X) and −0.48±0.18 mm (Y). The absolute differences between workflows were minimal, with −0.02±0.16 mm (X) and −0.14±0.18 mm (Y), indicating strong agreement. The plausible rounding of FS50 values to whole pixels in myQA FT may partially explain the observed differences, but these remain within clinical tolerance.

The **penumbra** analysis revealed consistent trends across the left and right sides, with minimal deviations between workflows. For the left side, LynxQA exhibited deviations of −0.01±0.11 mm (X) and 0.04±0.40 mm (Y) for protons, while myQA FT showed 0.04±0.11 mm (X) and −0.05±0.46 mm (Y). The absolute differences between workflows were similarly small (0.05±0.17 mm for X and −0.09±0.14 mm for Y). For the right side, the deviations were slightly higher, particularly for the X-direction (−0.32±0.13 mm for LynxQA and −0.45±0.22 mm for myQA FT) and Y direction (0.15±0.37 mm for LynxQA and 0.21±0.4 mm for myQA FT), with an absolute difference of −0.13±0.18 mm in X and 0.05±0.05 mm in Y. These results confirm robust consistency between the tools, with minor discrepancies.

The **symmetry** analysis results reveal slight deviations between LynxQA and myQA FT. For protons, LynxQA exhibited differences of 0.26±0.05 % (X) and 0.40±0.04 % (Y) relative to the expected values, while myQA FT showed 0.16±0.09 % (X) and 0.29±0.13 % (Y). The absolute differences between the tools were small, with −0.09±0.06 % (X) and −0.11±0.10 % (Y). These minor variations are within clinically acceptable limits and highlight the tools' consistency in symmetry assessment.

The homogeneity evaluation shows differences in treatment field uniformity between the workflows. For protons, LynxQA had homogeneity differences of 2.64±0.84 % while myQA FT showed slightly higher deviations of 2.76±0.82 %, resulting in an absolute difference of 0.12 %0.12%. Despite these differences, both tools demonstrate acceptable agreement.

Table 13: Summary of difference between LynxQA (L) and myQA FT (M).

SPOTMAPS		Spot Position		FWHM
Protons	**X**	0.14 ± 0.02 mm		-0.01±0.03 mm
	Y	-0.07 ± 0.03 mm		-0.18±0.06 mm
Carbons	**X**	0.14 ± 0.02 mm		0.18 ± 0.09 mm
	Y	-0.01 ± 0.03 mm		0.12 ± 0.11 mm
2D FIELDS		**CAX**	**FS50**	**Symmetry**
Protons	**X**	0.18±0.20 mm	-0.02±0.16 mm	-0.09±0.06 %
	Y	-0.38±0.17 mm	-0.14±0.18 mm	-0.11±0.10 %
Carbons	**X**	-0.02 ± 0.16 mm	-0.24±0.05 mm	-0.04±0.11 %
	Y	-0.14 ± 0.18 mm	-0.26±0.10 mm	0.05±0.16 %
		Penumbra -	**Penumbra +**	**2D Homogeneity**
Protons	**X**	0.05±0.17 mm	-0.13±0.18 mm	0.12±0.19 %
	Y	-0.09±0.14 mm	0.05±0.05 mm	
Carbons	**X**	-0.16±0.22 mm	-0.14±0.20 mm	0.30±0.20 %
	Y	-0.15±0.12 mm	-0.02±0.16 mm	

Carbon ion results mirror these findings, with similarly negligible differences between workflows. Furthermore, as can be seen in the plots for protons as well as for carbon ions, the data is well within the recommended QA tolerances and mostly within the measurement uncertainty. These results were generated with a high degree of precision and can be considered reliable for further analysis and discussion. The data is summarized in Table 12, where the absolute differences between the two software are denoted for protons as well as for carbon ions.

Overall, the results indicate that there is a minimal difference in the calculations of the parameters, and myQA FT proves to be a reliable alternative to replace LynxQA for measuring optics parameters at MedAustron.

5.2. Workflows

5.2.1. Spot Maps

The implementation of the new spot map QA workflow at MedAustron reflects significant improvements over the previous method and addresses challenges faced in similar facilities. This transition, from the fragmented workflows using separate tools such as Lynx2D for acquisition and LynxQA for analysis, to the streamlined use of myQA FT, offers several advantages. Primarily, this integration eliminates the need for intermediate steps, such as temporary data storage in Excel templates. This reduction in workflow complexity not only decreases the potential for human error but also shortens the overall time required for spot map acquisition. The improved efficiency of this process is particularly evident in the reduction of time for background measurements. The updated workflow offers a significant improvement in terms of time efficiency and ease of use. For instance, combining acquisition and analysis in a single software eliminates the need for manual data transfer and conveniently saves the data in the already used myQA database.

Additionally, the integration of the Sphinx Plugin into the QA process allows for the parallel analysis of Lynx and Sphinx Compact data (which uses the same setup and plugin), further reducing setup time. While these improvements primarily focus on workflow optimization, they also contribute to maintaining high-quality standards by reducing the risk of errors associated with manual interventions.

Despite these advancements, one limitation of the updated workflow is the uniform naming convention for tests (e.g. "1.Spotmap 62.4 MeV"), which requires users to remain vigilant to avoid mixing up energy values during data storage. While this drawback may lead to occasional inconveniences, its impact is minimal compared to the broader benefits of the streamlined workflow.

While comparisons to other facilities remain challenging due to the variability of workflows and protocols in hadron therapy (as noted in section 2.5.2 "Comparison to other facilities"), this approach offers a comprehensive and efficient methodology. The integration of automated processes and database connectivity makes this workflow a

scalable model for other facilities aiming to optimize QA practices without compromising on quality.

5.2.2. 2D Homogenous Field

The newly implemented QA workflow for 2D homogeneous field measurements introduces significant advancements in efficiency, accuracy, and usability. A key improvement is the integration of acquisition and analysis within a single software platform, myQA FT, which again eliminates the need for switching between multiple tools and reduces the manual handling of data. This streamlined process not only minimizes the potential for errors but also speeds up the QA workflow by removing the labor-intensive steps that characterized the previous methodology. For instance, the earlier workflow required manually saving data in a text file, importing it into an Excel template, and conducting analysis manually. In contrast, the updated workflow ensures data is processed and stored directly within the centralized myQA database.

A notable drawback of the current workflow is the lack of an export function in myQA FT for field analysis, requiring users to rely on a Python script for further data processing. While this script reduces manual effort compared to the older workflow, it still adds an extra step that could be avoided with future software updates. Notably, future updates from IBA could address this limitation by introducing an export button for field analysis, similar to the functionality already available for spot map analysis. This would further simplify the process by eliminating the need for the Python script altogether. These advantages are key to speeding up and improving the QA. The use of automated scripts and database integration reduces human error.

Despite the export limitation, the updated workflow demonstrates measurable improvements in automation and error reduction. By incorporating automated scripts for analysis and database integration, the process ensures consistency and reproducibility.

As with other workflows, the absence of standardized guidelines for 2D homogeneous field QA across hadron therapy facilities leaves room for variability in implementation. However, the improvements introduced by MedAustron offer a model that can be adapted

to other facilities, particularly if the export functionality is integrated in future updates. Overall, this workflow represents a robust and efficient approach to QA testing that aligns with the demands of modern particle therapy facilities.

5.2.3. Intra-spill Variation

As for the other workflows, the updated intra-spill variation QA workflow at MedAustron effectively leverages the myQA platform for both data acquisition and analysis, utilizing the FT plugin to streamline the process. This unified platform not only simplifies operations but also ensures consistency and reliability in quality assurance practices. By consolidating the workflow into a single system, the updated approach minimizes the potential for errors stemming from manual data transfer and improves the traceability of QA data through the myQA database.

A notable limitation of the workflow is the maximum frame count that can be selected during acquisition. The FT plugin encounters memory issues if more than approximately 150 frames are chosen, restricting the analysis to within this frame range. While this limitation may initially appear restrictive, it is generally not a concern, as 150 frames are typically sufficient to capture data for an entire spill. Furthermore, additional post-processing steps are required to evaluate frame-level data, which necessitates exporting the data into an Excel sheet before reimporting the processed results into the myQA database. These manual steps slightly offset the workflow's efficiency but are considered acceptable for maintaining system compatibility and consistency with other QA workflows.

Despite these challenges, the updated intra-spill variation workflow demonstrates clear benefits in terms of efficiency, standardization, and ease of use. The integration of the myQA system ensures that the workflow aligns with MedAustron's QA framework, while the reliance on automated data handling reduces human error. The adoption of this workflow also highlights opportunities for future improvements by IBA, such as expanding the FT plugin's frame-handling capacity or integrating advanced post-processing capabilities directly into the software.

In summary, while there are areas for refinement, the revised workflow represents a meaningful step forward in intra-spill variation QA. This approach sets a solid foundation for further development and serves as a reference point for other facilities looking to optimize similar processes.

6. Conclusion and Outlook

This thesis explored and compared key parameters in beam optics data acquisition and analysis, focusing on the transition from the Lynx2D/LynxQA system to the myQA FT platform. The investigation spanned a comprehensive dataset comprising spot maps and 2D homogeneous fields across various proton and carbon ion energies. The findings confirmed that myQA FT serves as a viable alternative to the currently employed LynxQA software at MedAustron, with results falling well within established tolerance ranges and exhibiting consistent trends for both particle types.

The study underscored the central role of beam optics QA within the broader context of Light Ion Beam Therapy. By addressing the limitations of in-house QA tools, this work demonstrated how commercially developed medical software, such as myQA FT, can streamline workflows while maintaining high-quality standards. The integration of acquisition and analysis into a single platform minimizes human error, enhances efficiency, and facilitates the seamless storage and management of QA data within the myQA database. Notably, this transition reduces reliance on intermediate steps, such as manual data transfer through Excel templates, further optimizing operations.

Despite its advantages, the myQA FT software still has limitations, such as the lack of an export function for 2D homogeneous field analysis. These gaps were addressed with workaround solutions, including the development of a Python script for data processing. The continued development of myQA FT, particularly through enhancements like integrated export functionality, has the potential to further simplify QA workflows and reduce the need for additional technical interventions.

The findings of this thesis also hold broader implications for the field of proton therapy QA. Historically, the market for commercial QA solutions has been limited, leading to many facilities to rely on custom, in-house tools. While these tools are tailored to specific institutional needs, they require ongoing maintenance and updates, which can strain resources. This study demonstrated the potential of the myQA environment, including the Sphinx and Lynx plugins, to offer a streamlined, commercially supported alternative. The adoption of such solutions has the potential to standardize QA practices, enhance

operational efficiency, and enable smoother transitions to commercial software in clinical settings.

Looking forward, future work should explore expanding the scope of myQA FT to address the needs of more advanced QA procedures, such as automated reporting and in-depth data analytics. Collaboration between clinical facilities and software developers, like IBA Dosimetry, is essential to refine these tools further, ensuring they meet the evolving demands of proton therapy QA. Additionally, more comparative studies between commercial and in-house QA tools across multiple institutions could help establish industry-wide benchmarks and best practices.

In conclusion, this thesis presents a significant step toward modernizing beam optics QA workflows at MedAustron. By demonstrating the practicality and efficiency of commercial software solutions, it lays a foundation for broader adoption and continuous improvement in QA methodologies, ultimately contributing to the advancement of precision and reliability in proton therapy.

7. References

1. GBD 2015 Disease and Injury Incidence and Prevalence Collaborators. Global, regional, and national incidence, prevalence, and years lived with disability for 310 diseases and injuries, 1990-2015: a systematic analysis for the Global Burden of Disease Study 2015. *Lancet*. 2016;388(10053):1545-1602. doi:10.1016/S0140-6736(16)31678-6

2. Sung H, Ferlay J, Siegel RL, et al. Global Cancer Statistics 2020: GLOBOCAN Estimates of Incidence and Mortality Worldwide for 36 Cancers in 185 Countries. *CA Cancer J Clin*. 2021;71(3):209-249. doi:10.3322/caac.21660

3. Cancer Today. Accessed April 19, 2024. https://gco.iarc.fr/today/online-analysis-table?v=2020&mode=cancer&mode_population=continents&population=900&populations=900&key=asr&sex=0&cancer=39&type=0&statistic=5&prevalence=0&population_group=0&ages_group%5B%5D=0&ages_group%5B%5D=17&group_cancer=1&include_nmsc=0&include_nmsc_other=1

4. Debela DT, Muzazu SG, Heraro KD, et al. New approaches and procedures for cancer treatment: Current perspectives. *SAGE Open Med*. 2021;9:20503121211034370. doi:10.1177/20503121211034366

5. Dilmanian FA, Eley JG, Rusek A, Krishnan S. Charged Particle Therapy with Mini-Segmented Beams. *Front Oncol*. 2015;5. doi:10.3389/fonc.2015.00269

6. Amladi U DMBJOJ. A Facility for Tumour Therapy and Biomedical Research in Sout-Eastern Europe. *Research Gate*. (2019).

7. Zeman EM, Schreiber EC, Tepper JE. Basics of Radiation Therapy. In: *Abeloff's Clinical Oncology*. Elsevier; 2014:393-422.e3. doi:10.1016/B978-1-4557-2865-7.00027-8

8. Barish RJ. Radiation Oncology Physics: A Handbook for Teachers and Students. *Health Phys*. 2006;90(5):501. doi:10.1097/01.HP.0000203316.33943.55

9. Thomson M. *Modern Particle Physics*. Cambridge University Press; 2013. doi:10.1017/CBO9781139525367

10. Aldenhoven L, Ramaekers B, Degens J, et al. Cost-effectiveness of proton radiotherapy versus photon radiotherapy for non-small cell lung cancer patients: Exploring the model-based approach. *Radiotherapy and Oncology*. 2023;183:109417. doi:10.1016/j.radonc.2022.11.006

11. Wilson RR. Radiological Use of Fast Protons. *Radiology*. 1946;47(5):487-491. doi:10.1148/47.5.487

12. LAWRENCE JH. Proton irradiation of the pituitary. *Cancer*. 1957;10(4):795-798. doi:10.1002/1097-0142(195707/08)10:4<795::aid-cncr2820100426>3.0.co;2-b

13. Castro JR, Quivey JM, Lyman JT, et al. Current status of clinical particle radiotherapy at Lawrence Berkeley Laboratory. *Cancer*. 1980;46(4):633-641. doi:10.1002/1097-0142(19800815)46:4<633::aid-cncr2820460402>3.0.co;2-o

14. Larsson B, Leksell L, Rexed B, Sourander P. Effect of High Energy Protons on the Spinal Cord. *Acta radiol*. 1959;Volume 51(1):52-64. doi:10.1177/028418515905100106

15. LARSSON B. Pre-therapeutic physical experiments with high energy protons. *Br J Radiol*. 1961;34:143-151. doi:10.1259/0007-1285-34-399-143

16. Particle Therapy Co-Operative Group. December 7, 2023. Accessed December 7, 2023. https://www.ptcog.site/index.php/patient-statistics-2

17. Tsujii H, Kamada T, Baba M, et al. Clinical advantages of carbon-ion radiotherapy. *New J Phys*. 2008;10(7):075009. doi:10.1088/1367-2630/10/7/075009

18. Stock M, Georg D, Ableitinger A, et al. The technological basis for adaptive ion beam therapy at MedAustron: Status and outlook. *Z Med Phys*. 2018;28(3):196-210. doi:10.1016/j.zemedi.2017.09.007

19. Thomson M. *Modern Particle Physics*. Cambridge University Press; 2013. doi:10.1017/CBO9781139525367

20. Russo S, Mirandola A, Molinelli S, et al. Characterization of a commercial scintillation detector for 2-D dosimetry in scanned proton and carbon ion beams. *Phys Med*. 2017;34:48-54. doi:10.1016/j.ejmp.2017.01.011

21. Paganetti H, ed. *Proton Therapy Physics*. CRC Press; 2018. doi:10.1201/b22053

22. Ballabriga R, Blaj G, Campbell M, et al. Characterization of the Medipix3 pixel readout chip. *Journal of Instrumentation*. 2011;6(01):C01052-C01052. doi:10.1088/1748-0221/6/01/C01052

23. Newhauser WD, Zhang R. The physics of proton therapy. *Phys Med Biol*. 2015;60(8):R155-R209. doi:10.1088/0031-9155/60/8/R155

24. Janni JF. Energy loss, range, path length, time-of-flight, straggling, multiple scattering, and nuclear interaction probability. *At Data Nucl Data Tables*. 1982;27(4-5):341-529. doi:10.1016/0092-640X(82)90005-5

25. Haug E, Nakel W. *The Elemental Process of Bremsstrahlung*. World Scientific Publishing Co Pte Ltd, 978-981-238-578-9 (ISBN); 2004.

26. https://pdg.lbl.gov/2022/reviews/contents_sports.html. Physical constants. (accessed on Dezember 2024)

27. Wieser ME, Coplen TB. Atomic weights of the elements 2009 (IUPAC Technical Report). *Pure and Applied Chemistry*. 2010;83(2):359-396. doi:10.1351/PAC-REP-10-09-14

28. Tiesinga E, Mohr PJ, Newell DB, Taylor BN. CODATA Recommended Values of the Fundamental Physical Constants: 2018. *J Phys Chem Ref Data*. 2021;50(3). doi:10.1063/5.0064853

29. Mohamad O, Sishc B, Saha J, et al. Carbon Ion Radiotherapy: A Review of Clinical Experiences and Preclinical Research, with an Emphasis on DNA Damage/Repair. *Cancers (Basel)*. 2017;9(6):66. doi:10.3390/cancers9060066

30. Verhey LJ, Petti PL. Principles of Radiation Physics. In: *Leibel and Phillips Textbook of Radiation Oncology*. Elsevier; 2010:95-119. doi:10.1016/B978-1-4160-5897-7.00007-X

31. Paganetti H, ed. *Proton Therapy Physics*. CRC Press; 2018. doi:10.1201/b22053

32. Berger MJ, Coursey JS, Zucker MA, Chang J. Stopping-Power & Range Tables for Electrons, Protons, and Helium Ions. *Physical Measurement Laboratory*. DOI: https://dx.doi.org/10.18434/T4NC7P, 2017.

33. Mohamad O, Sishc BJ, Saha J, et al. Carbon Ion Radiotherapy: A Review of Clinical Experiences and Preclinical Research, with an Emphasis on DNA Damage/Repair. *Cancers (Basel)*. 2017;9(6). doi:10.3390/cancers9060066

34. Butson MJ, Yu PKN, Cheung T, Metcalfe P. Radiochromic film for medical radiation dosimetry. *Materials Science and Engineering: R: Reports*. 2003;41(3-5):61-120. doi:10.1016/S0927-796X(03)00034-2

35. McLaughlin WL, Al-Sheikhly M, Lewis DF, Kovács A, Wojnárovits L. Radiochromic Solid-State Polymerization Reaction. In: ; 1996:152-166. doi:10.1021/bk-1996-0620.ch011

36. Reimer B, Baessler H. Photoconduction in a Polydiacetylene Crystal. *Physica Status Solidi (a)*. 1975;32(2):435-439. doi:10.1002/pssa.2210320211

37. *Physics and Engineering of Radiation Detection*. Elsevier; 2015. doi:10.1016/C2013-0-15270-1

38. Ciangaru G, Yang JN, Oliver PJ, et al. Verification procedure for isocentric alignment of proton beams. *J Appl Clin Med Phys*. 2007;8(4):65-75. doi:10.1120/jacmp.v8i4.2671

39. Mirandola A, Molinelli S, Vilches Freixas G, et al. Dosimetric commissioning and quality assurance of scanned ion beams at the Italian National Center for Oncological Hadrontherapy. *Med Phys*. 2015;42(9):5287-5300. doi:10.1118/1.4928397

40. Sanchez-Parcerisa D, Sanz-García I, Ibáñez P, et al. Radiochromic film dosimetry for protons up to 10 MeV with EBT2, EBT3 and unlaminated EBT3 films. *Phys Med Biol*. 2021;66(11):115006. doi:10.1088/1361-6560/abfc8d

41. Lin Y, Zhang H, Gu S, et al. Proton beam spot size and position measurements using a multi-strip ionization chamber. *Physica Medica*. 2024;123:103411. doi:10.1016/j.ejmp.2024.103411

42. Yang Y, Shi C, Chen C, et al. A 2D strip ionization chamber array with high spatiotemporal resolution for proton pencil beam scanning FLASH radiotherapy. *Med Phys*. 2022;49(8):5464-5475. doi:10.1002/mp.15706

43. Jeong S, Yoon M, Chung K, Ahn SH, Lee B, Seo J. Clinical application of a gantry-attachable plastic scintillating plate dosimetry system in pencil beam scanning proton therapy beam monitoring. *Physica Medica*. 2020;77:181-186. doi:10.1016/j.ejmp.2020.08.019

44. Almurayshid M, Helo Y, Kacperek A, Griffiths J, Hebden J, Gibson A. Quality assurance in proton beam therapy using a plastic scintillator and a commercially available digital camera. *J Appl Clin Med Phys*. 2017;18(5):210-219. doi:10.1002/acm2.12143

45. Paganetti H, ed. *Proton Therapy Physics*. CRC Press; 2018. doi:10.1201/b22053

46. El-Saftawy, A. A. M. and Zagazig University, Physics Department (Egypt) (2013) "Regulating The Performance Parameters Of Accelerated Particles".

47. Grevillot L, Stock M, Vatnitsky S. Evaluation of beam delivery and ripple filter design for non-isocentric proton and carbon ion therapy. *Phys Med Biol*. 2015;60(20):7985-8005. doi:10.1088/0031-9155/60/20/7985

48. Stock M, Georg P, Mayer R, Böhlen TT, Vatnitsky S. Development of Clinical Programs for Carbon Ion Beam Therapy at MedAustron. *Int J Part Ther*. 2016;2(3):474-477. doi:10.14338/IJPT-15-00022.1

49. Abousaida B, Hsieh C en, Venkatesulu BP, Krishnan S. Technological Advances in Radiotherapy. In: *Radiotherapy of Liver Cancer*. Springer Singapore; 2021:73-91. doi:10.1007/978-981-16-1815-4_6

50. *ICRU Report 78, Prescribing, Recording, and Reporting Proton-Beam Therapy*. Accessed April 19, 2024. https://www.icru.org/report/prescribing-recording-and-reporting-proton-beam-therapy-icru-report-78/

51. Arjomandy B, Taylor P, Ainsley C, et al. AAPM task group 224: Comprehensive proton therapy machine quality assurance. *Med Phys*. 2019;46(8):e678-e705. doi:10.1002/mp.13622

52. Saotome N, Furukawa T, Hara Y, et al. Design and performance of daily quality assurance system for carbon ion therapy at NIRS. *Nucl Instrum Methods Phys Res B*. 2017;406:356-360. doi:10.1016/j.nimb.2017.03.059

53. Mirandola A, Molinelli S, Vilches Freixas G, et al. Dosimetric commissioning and quality assurance of scanned ion beams at the Italian National Center for Oncological Hadrontherapy. *Med Phys*. 2015;42(9):5287-5300. doi:10.1118/1.4928397

54. Varasteh Anvar M, Attili A, Ciocca M, et al. Quality assurance of carbon ion and proton beams: A feasibility study for using the 2D MatriXX detector. *Physica Medica*. 2016;32(6):831-837. doi:10.1016/j.ejmp.2016.05.058

55. Ding X, Zheng Y, Zeidan O, et al. A novel daily QA system for proton therapy. *J Appl Clin Med Phys*. 2013;14(2):4058. doi:10.1120/jacmp.v14i2.4058

56. Lambert J, Bäumer C, Koska B, Ding X. Daily QA in proton therapy using a single commercially available detector. *J Appl Clin Med Phys*. 2014;15(6):5005. doi:10.1120/jacmp.v15i6.5005

57. Actis O, Meer D, König S, Weber DC, Mayor A. A comprehensive and efficient daily quality assurance for PBS proton therapy. *Phys Med Biol*. 2017;62(5):1661-1675. doi:10.1088/1361-6560/aa5131

58. Bizzocchi N, Fracchiolla F, Schwarz M, Algranati C. A fast and reliable method for daily quality assurance in spot scanning proton therapy with a compact and inexpensive phantom. *Med Dosim*. 42(3):238-246. doi:10.1016/j.meddos.2017.05.001

59. Younkin JE, Shen J, Bues M, et al. Technical Note: An efficient daily QA procedure for proton pencil beam scanning. *Med Phys*. 2018;45(3):1040-1049. doi:10.1002/mp.12787

60. Russo S, Mirandola A, Molinelli S, et al. Characterization of a commercial scintillation detector for 2-D dosimetry in scanned proton and carbon ion beams. *Phys Med*. 2017;34:48-54. doi:10.1016/j.ejmp.2017.01.011

61. INTERNATIONAL ATOMIC ENERGY AGENCY, Absorbed Dose Determination in External Beam Radiotherapy, Technical Reports Series No. 398, IAEA, Vienna (2000)

62. *ICRU Report 49, Stopping Power and Ranges for Protons and Alpha Particles*. https://doi.org/10.1118/1.597176

63. Elia A, Grevillot L, Stock M. *Medical Physics Terminologies for Parameters Associated with Dose Distributions*. Physica Medica Vol 71. https://doi.org/10.1016/j.ejmp.2020.02.006; 2014.

64. Grevillot L, Moreno JO, Fuchs H, et al. Implementation of Sphinx/Lynx as daily QA equipment for scanned proton and carbon ion beams. *J Appl Clin Med Phys*. 2023;24(4). doi:10.1002/acm2.13896

65. Russo S, Mirandola A, Molinelli S, et al. Characterization of a commercial scintillation detector for 2-D dosimetry in scanned proton and carbon ion beams. *Physica Medica*. 2017;34:48-54. doi:10.1016/j.ejmp.2017.01.011

8

8.   Use of Artificial Intelligence

For linguistic improvements, ChatGPT 4.0 was used between August 2024 and January 2025. While the research and original writing were conducted by the author, ChatGPT was used as a supportive tool to enhance the coherence and readability of this thesis.

9. Annex

9.1. Expected Values at MedAustron

Table 14: Chosen spot coordinates for the nine spots in a spot map

Spot-ID	X[mm]	Y[mm]	Spot-ID	X[mm]	Y[mm]
1	100	100	6	-100	0
2	0	100	7	0	-100
3	-100	100	8	100	-100
4	100	0	9	-100	-100
5	0	0			

Table 15: Expected values for FWHM for protons and carbon-ions.

Protons		Carbon-ions	
Energy [MeV/u]	X/Y FWHM [mm]	Energy [MeV/u]	X/Y FWHM [mm]
62.4	21.5	120.0	9.6
97.4	14.4	213.4	7.3
148.2	10.6	284.7	6.6
198.0	9.0	346.6	6.6
252.7	7.4	402.8	6.7

Table 16: Expected values for FS50 for protons and carbon-ions.

Protons		Carbon-ions	
Energy [MeV/u]	X/Y FS50[mm]	Energy [MeV/u]	X/Y FS50[mm]
62.4	105.3/105.2	120.0	102.0/102.2
97.4	103.7/103.6	213.4	102.0/102.2
148.2	102.0/101.7	284.7	102.1/102.1
198.0	102.7/102.2	346.6	102.0/102.0
252.7	101.5/101.2	402.8	101.9/102.1

Table 17: Expected values for left and right sided penumbra for protons and carbon-ions.

Protons			Carbon-ions		
Energy [MeV/u]	X/Y Penumbra- [mm]	X/Y Penumbra+ [mm]	Energy [MeV/u]	X/Y Penumbra- [mm]	X/Y Penumbra+ [mm]
62.4	15.3/15.8	15.5/15.7	120.0	7.1/7.0	7.2/7.0
97.4	10.3/10.8	10.7/10.7	213.4	5.4/5.2	5.3/5.3
148.2	7.5/8.0	7.8/7.8	284.7	4.5/4.5	4.6/4.7
198.0	6.4/6.4	6.6/6.5	346.6	4.6/4.7	4.6/4.6
252.7	5.3/5.6	5.3/5.6	402.8	4.7/4.7	4.6/4.6

Table 18: Warning and Fail limits at MedAustron for the parameters analyzed.

Parameter	Warning	Fail
Spot Position [mm]	>1.5	>2
FWHM [mm]	>1.5	>2
FS50 [mm]	>2	>3
Sy mmetry [%]	>2	>3
Homogeneity [%]	>5 (protons) >7 (carbons)	>10

9.2.   Plots with Carbon Ions
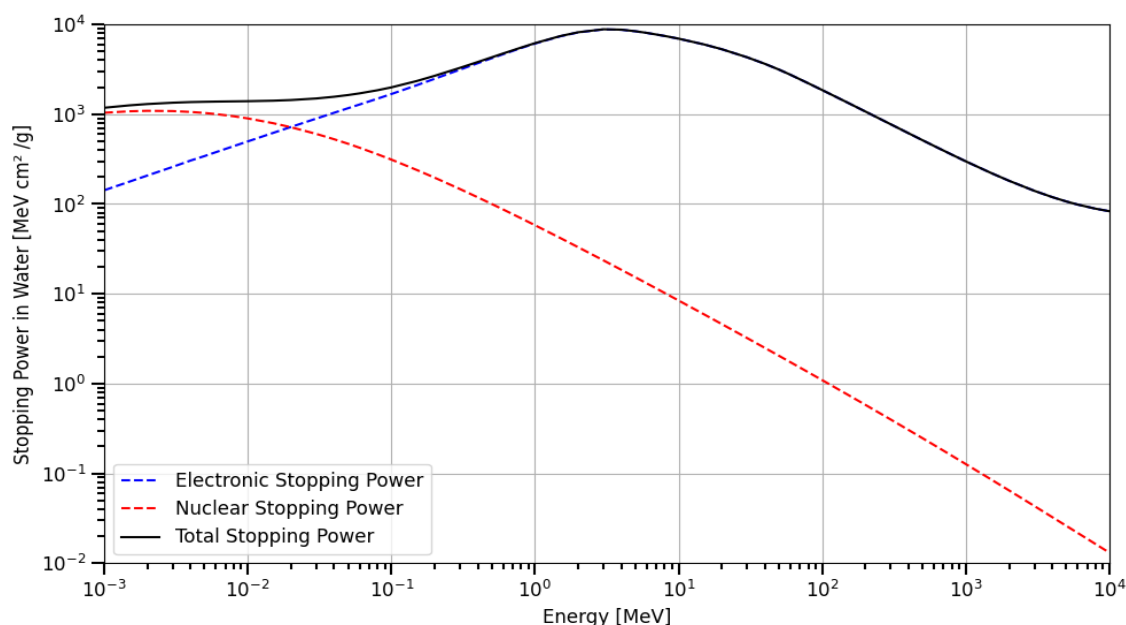
Figure 35: Total, electronic, and nuclear stopping power of carbon ions in water, showing the low effect of nuclear interaction at the energy range of meV to GeV. (. (From NIST) [32]
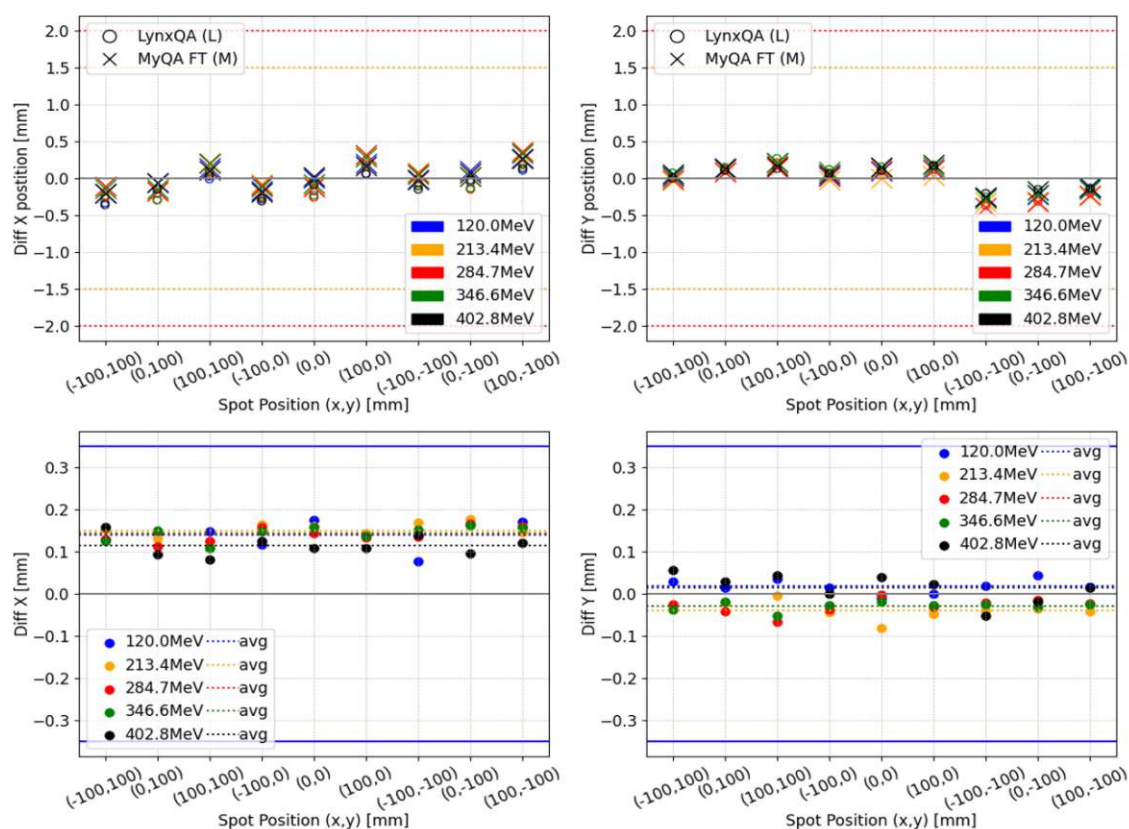
Figure 36: (Carbons) Top: X/Y Spot position: Difference to expected value for myQA FT(M) and LynxQA(L) Bottom: X/Y Absolute difference between myQA FT(M) and LynxQA(L), where the average over all spots per energy is plotted with dotted lines.
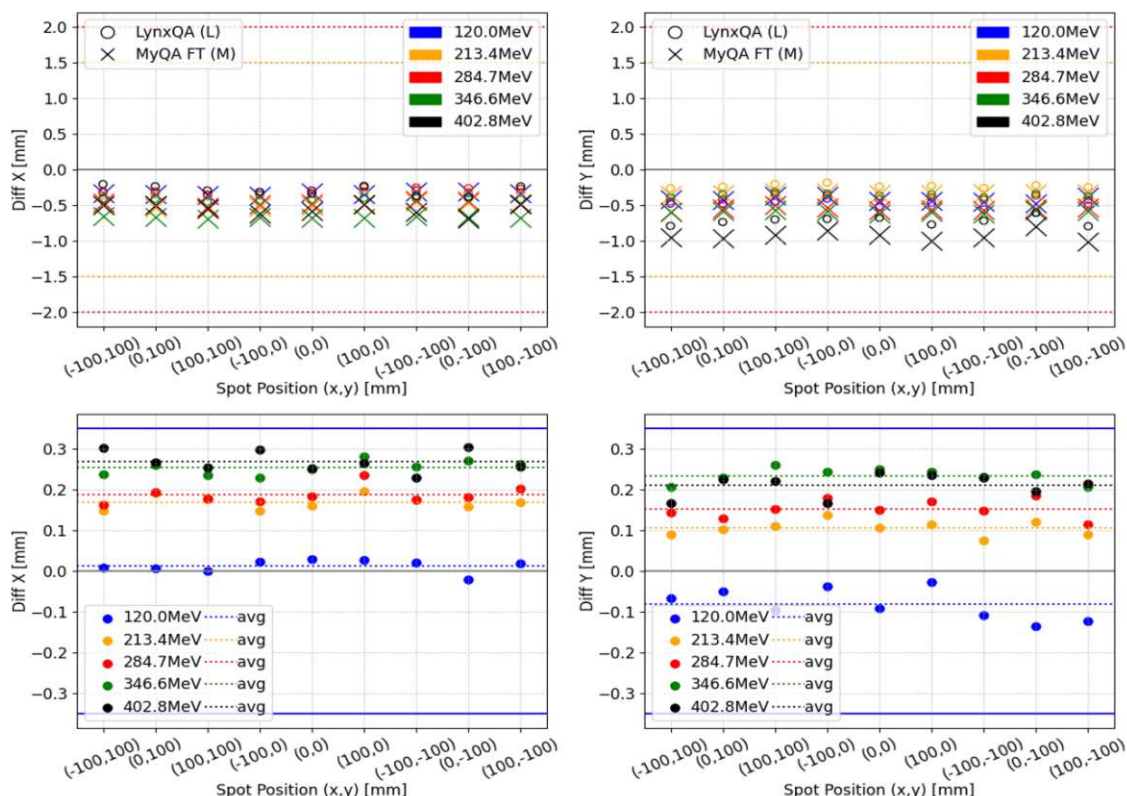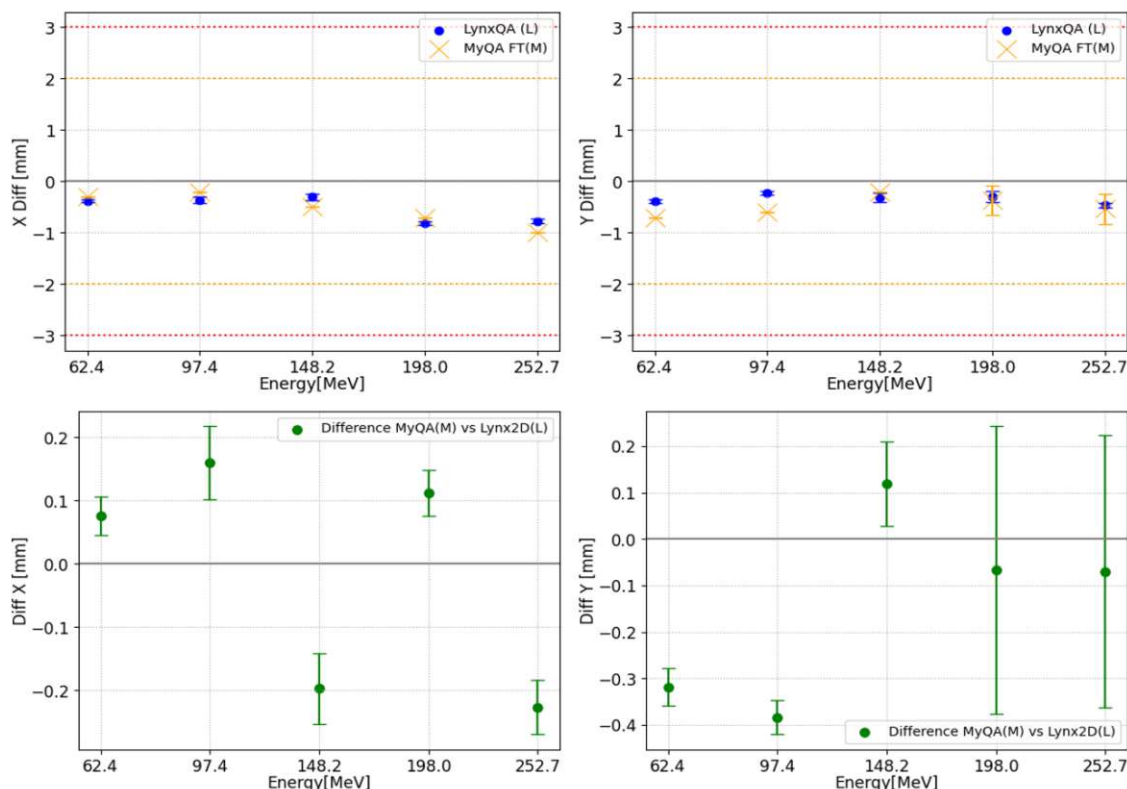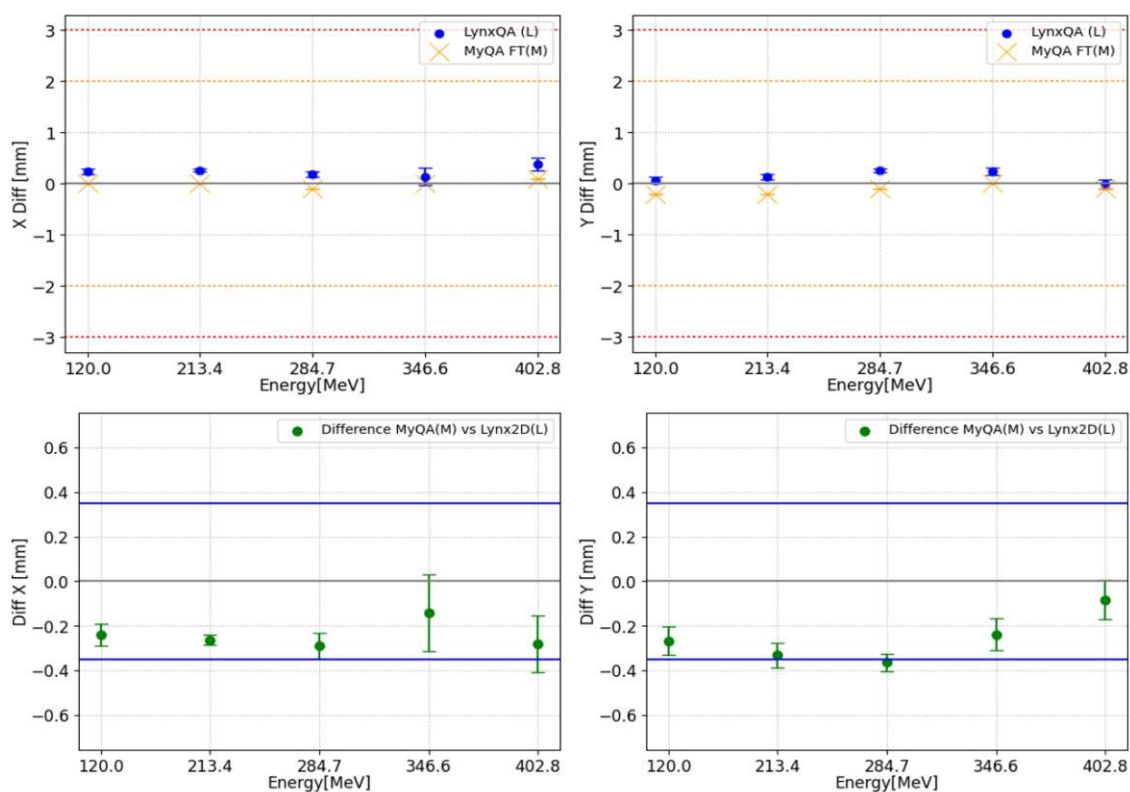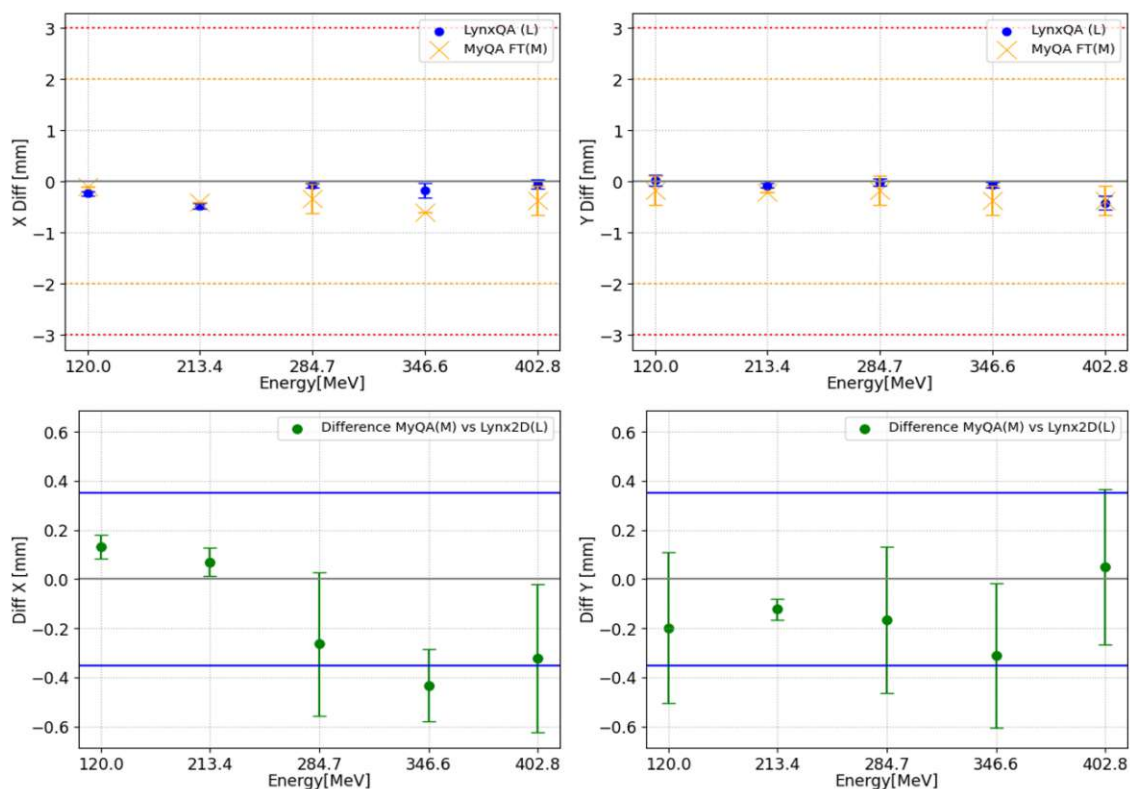
Figure 37 : (Carbons) Top: X/Y FWHM: Difference to expected value for LynxQA(L) and myQA FT(M). Bottom: X/Y Absolute difference between myQA FT(M) and LynxQA (L), where the average over all spots per energy is plotted with dotted lines.
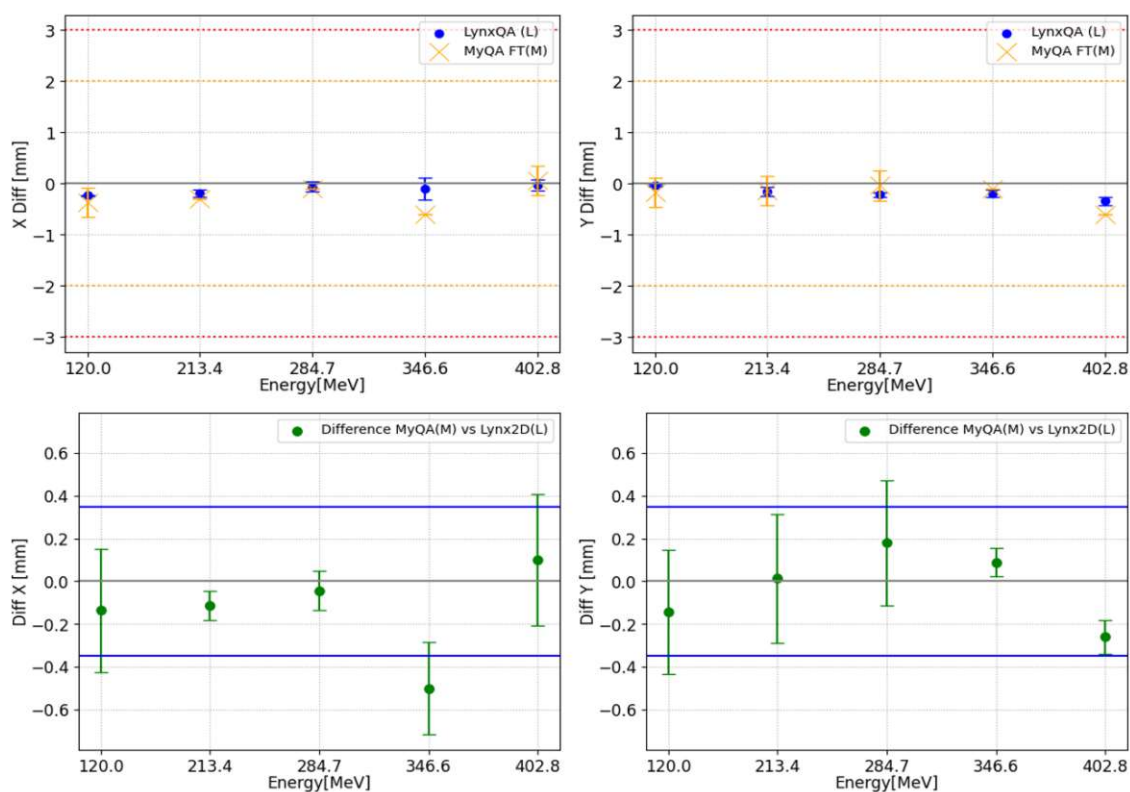

Figure 38 : (Carbons) Top: X/Y CAX: Difference to the expected value for LynxQA(L) and myQA FT(M). Bottom: X/Y Absolute difference between myQA FT(M) and LynxQA (L), where the average over all spots per energy is plotted with dotted lines.

Figure 39 : (Carbons) Top: X/Y FS50: Difference to the expected value for LynxQA(L) and myQA FT(M). Bottom: X/Y Absolute difference between myQA FT(M) and LynxQA (L), where the average over all spots per energy is plotted with dotted lines.
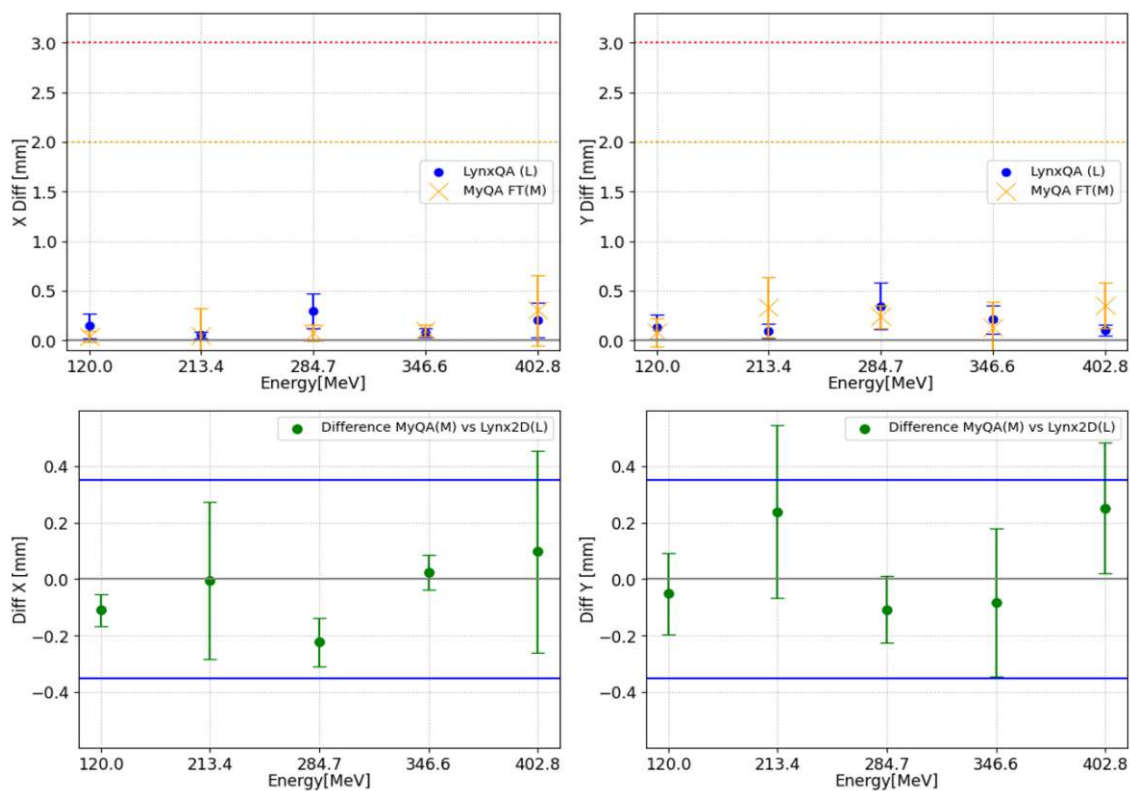

Figure 40 : (Carbons) Top: X/Y Penumbra (left side): Difference to the expected value for LynxQA(L) and myQA FT(M). Bottom: X/Y Absolute difference between myQA FT(M) and LynxQA (L), where the average over all spots per energy is plotted with dotted lines.
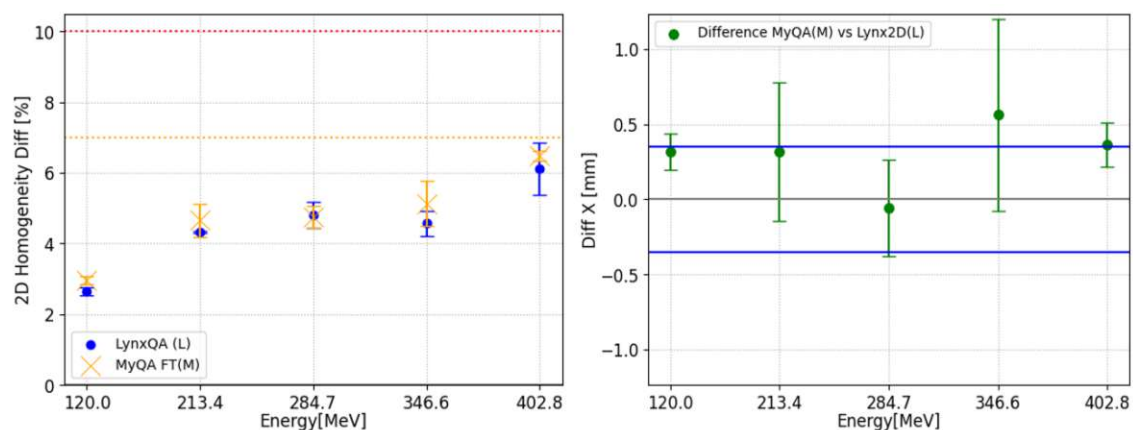
Figure 41 : (Carbons) Top: X/Y Penumbra (right side): Difference to the expected value for LynxQA(L) and myQA FT(M). Bottom: X/Y Absolute difference between myQA FT(M) and LynxQA (L), where the average over all spots per energy is plotted with dotted lines.

Figure 42 : (Carbons) Top: X/Y Symmetry: Difference to the expected value for LynxQA(L) and myQA FT(M). Bottom: X/Y Absolute difference between myQA FT(M) and LynxQA (L), where the average over all spots per energy is plotted with dotted lines.

Figure 43 : (Carbons) Top: 2D Homogeneity: Difference to the expected value for LynxQA(L) and myQA FT(M). Bottom: X/Y Absolute difference between myQA FT(M) and LynxQA (L), where the average over all spots per energy is plotted with dotted lines.
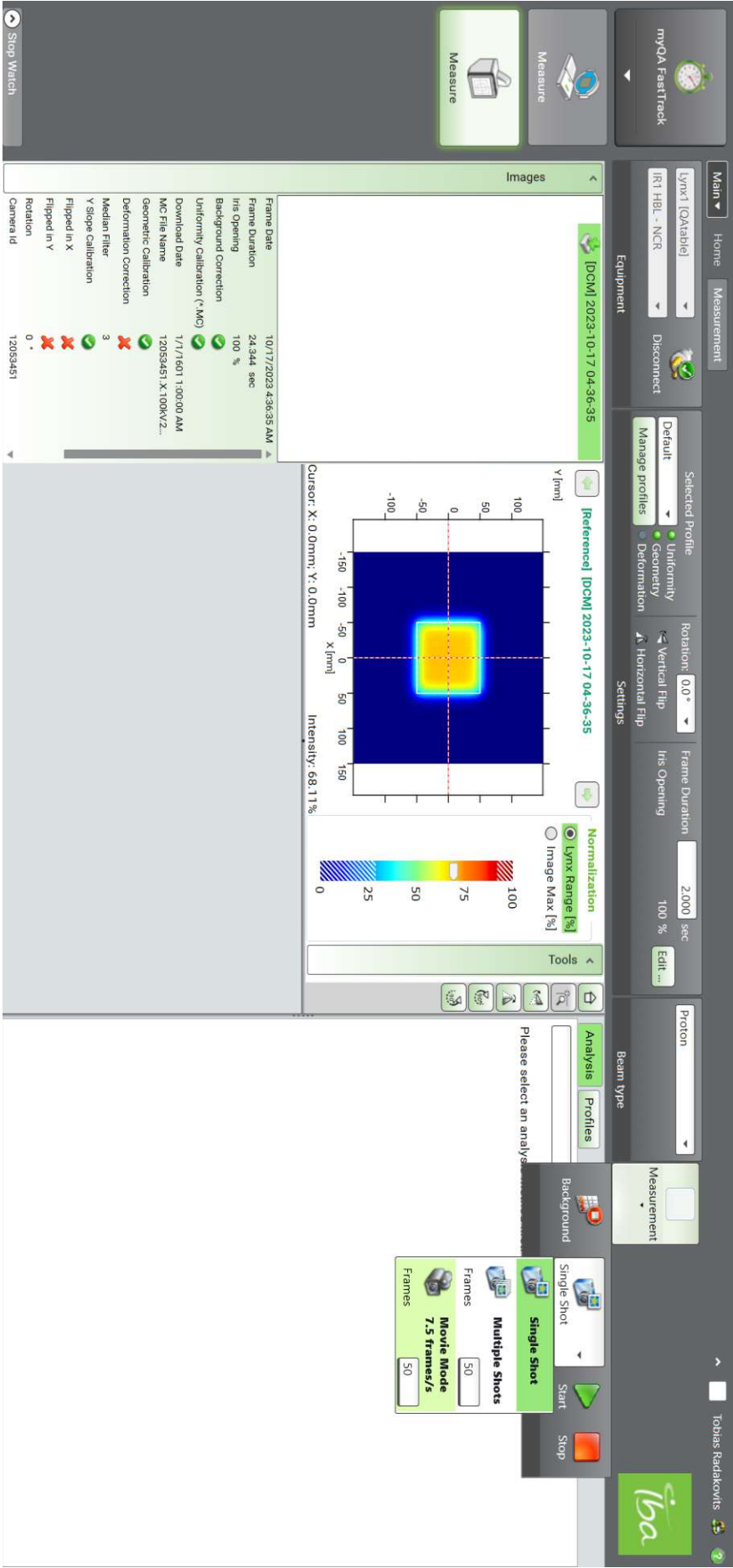
Figure 44: Measurement tab of myQA FT. Images are shown on the left and can be renamed. A proton field with 62.4 MeV is shown as well as the different measurement modes.
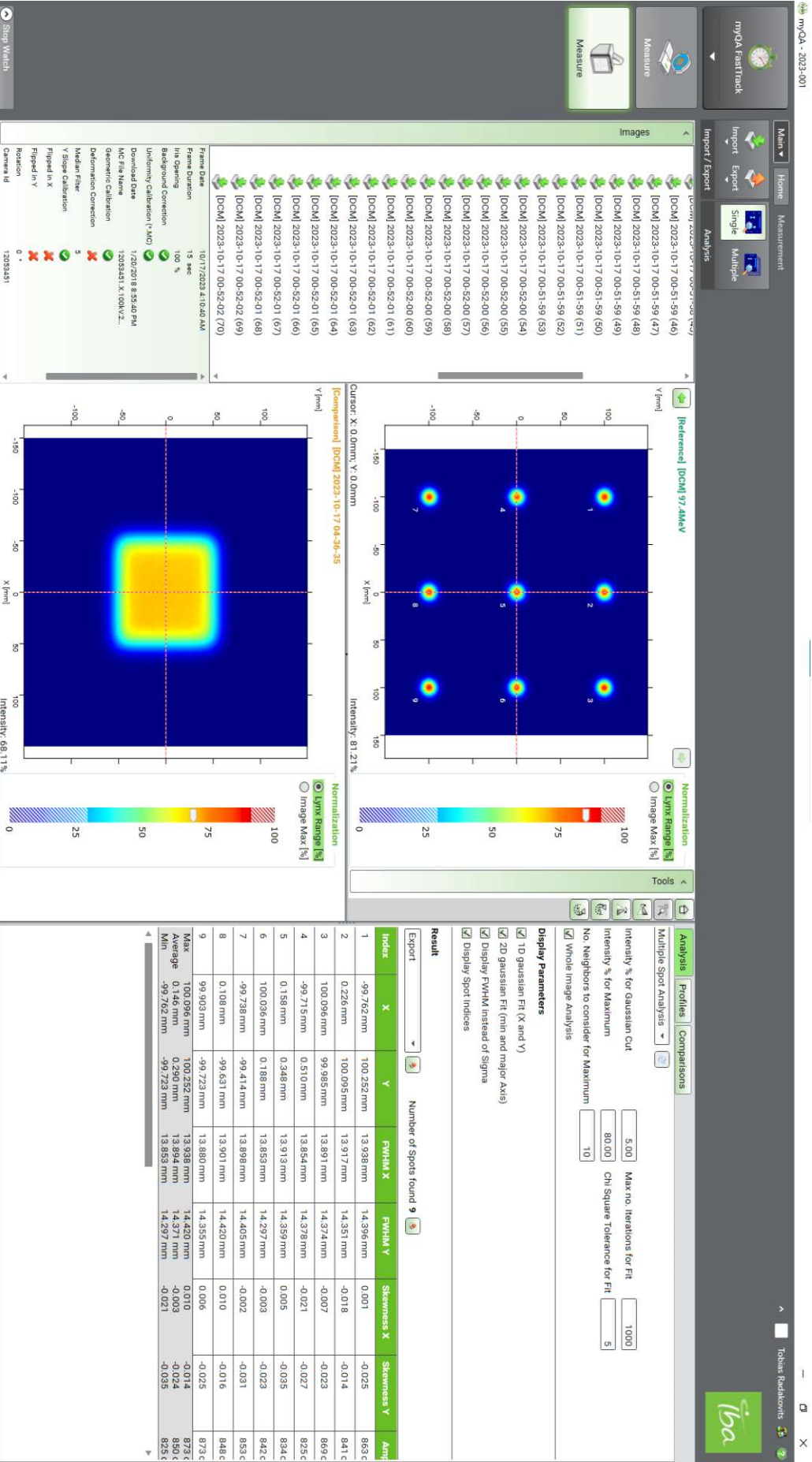
Figure 45: Home tab of myQA FT. On the left the recorded images are temporary saved. To utilize the comparison function, in this case another spot map must be employed. In this instance, a 2D field was utilized for display purposes. On the right the analysis and their default settings for the selected spot map are shown.
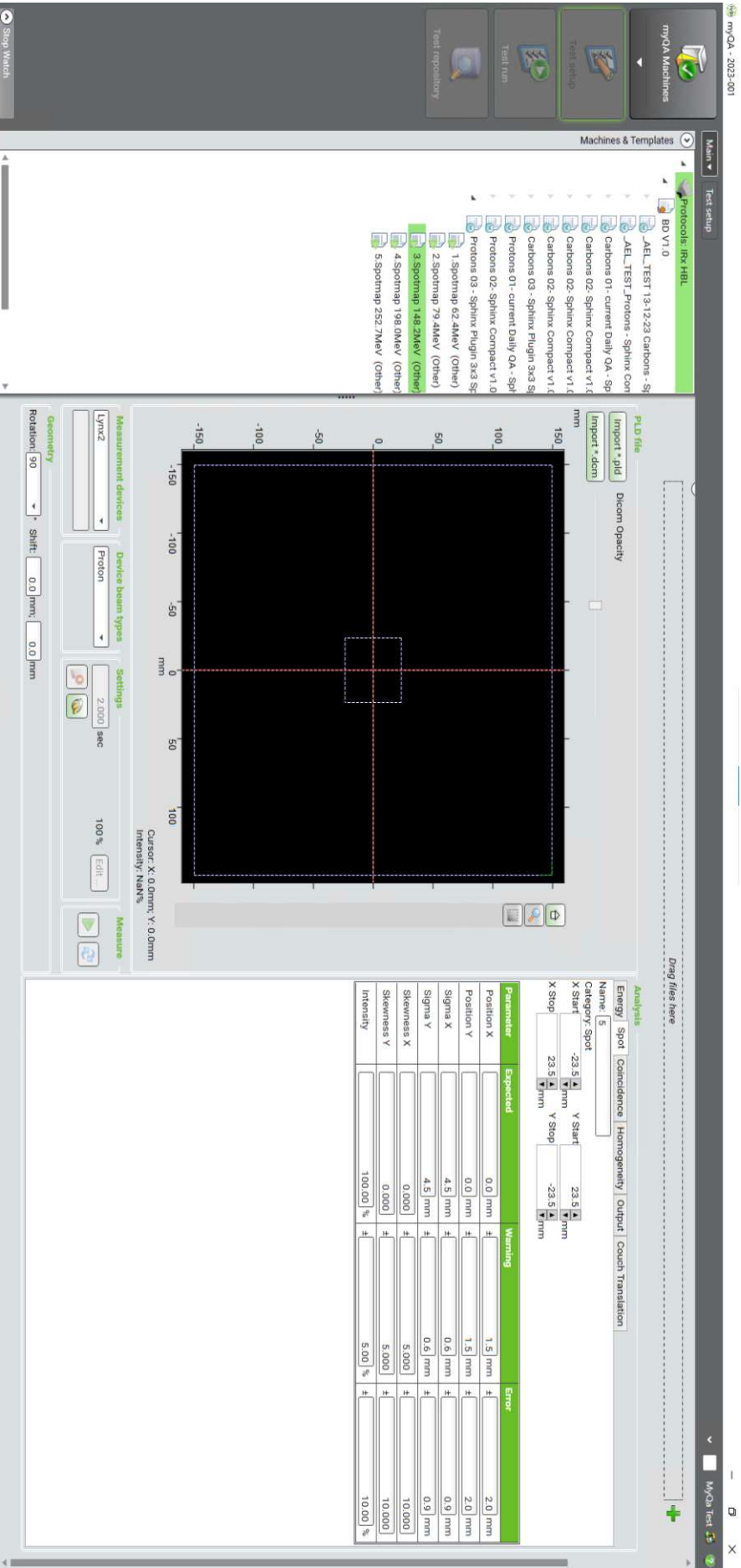
Figure 46: Test creation of a spot map analysis for a proton beam with 148.2 MeV for SP. On the right the area and the thresholds are defined. On the bottom the measurement device and particle type is chosen. A rotation of 90° is selected to show the image in beam view.
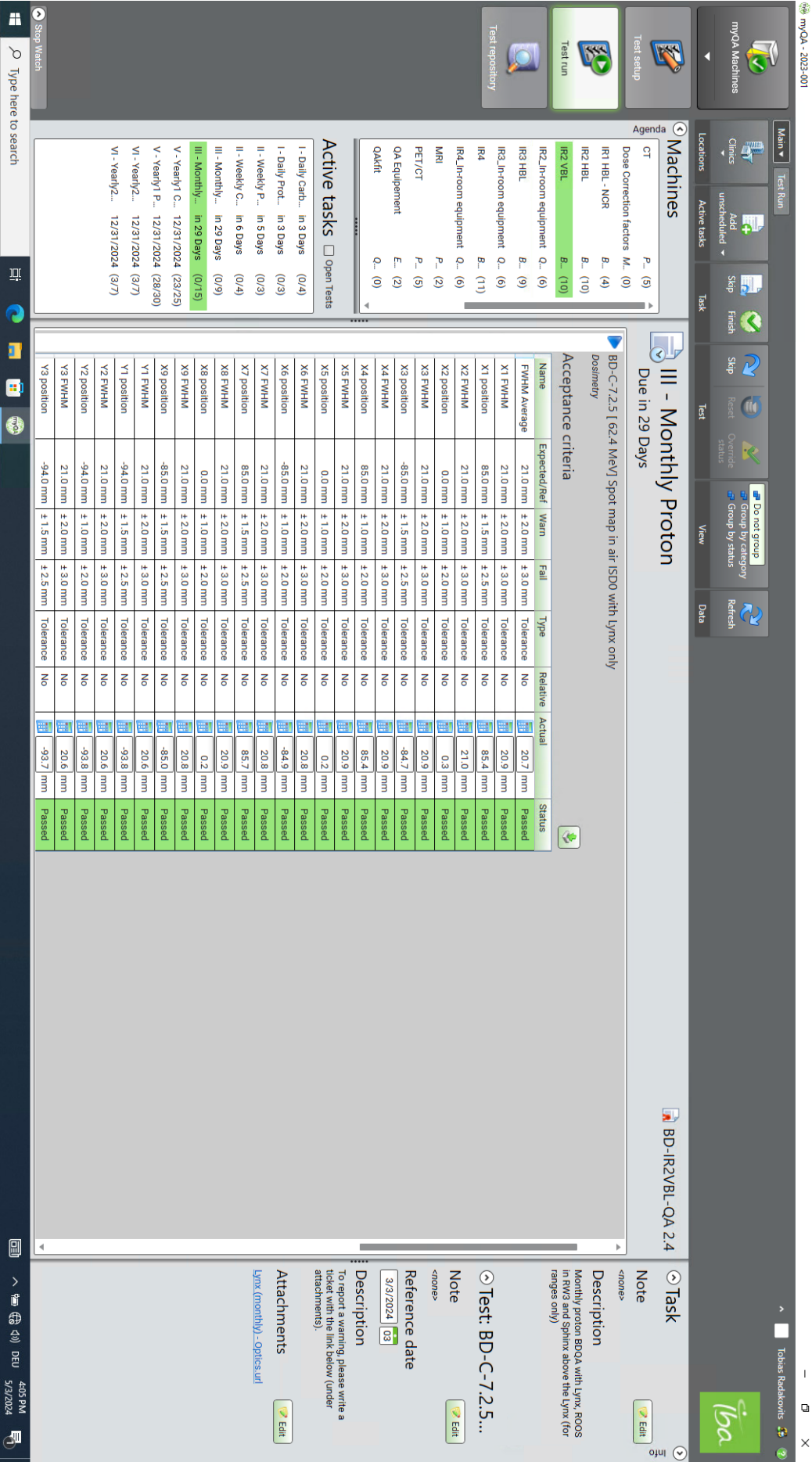
Figure 47: Spot map parameter analysis in myQA Machines measured with Lynx. When the data is within threshold the status turns green and the data is saved in the database.